



**UNIVERSITY OF NAIROBI**

**THREE-DIMENSIONAL PRINTING AND CHARACTERIZATION OF  
BOTTLING PRODUCTS FABRICATED USING POLYLACTIC ACID  
AND ACRYLONITRILE BUTADIENE STYRENE**

**BY**

**BELETA DIBLI OTIENO**

**I56/33747/2019**

**A Research Thesis Submitted in Partial Fulfillment of the Requirements  
for the Award of the Degree of Master of Science in Industrial Chemistry  
of the University of Nairobi**

**2022**

## DECLARATION

I declare that this thesis is my original work and has not been submitted elsewhere for research. Where other people's work has been used, that has been properly acknowledged and referenced in accordance with the University of Nairobi's requirements.

BELETA DIBLI OTIENO

I56/33747/2019


Department of Chemistry

University of Nairobi

Signature:  Date: 7/03/2023.

This dissertation is submitted for research with our approval as research supervisors:

Dr. Geoffrey Bosire  
Department of Chemistry  
University of Nairobi  
[gboseire@uonbi.ac.ke](mailto:gboseire@uonbi.ac.ke)

Signature 

Date: 08/03/2023

Prof. John Mmari Onyari  
Department of Chemistry  
University of Nairobi  
[jonnyari@uonbi.ac.ke](mailto:jonnyari@uonbi.ac.ke)

Signature 

Date: 08/03/2023

Prof. Julius M. Mwabora  
Department of Physics  
University of Nairobi  
[mwabora@uonbi.ac.ke](mailto:mwabora@uonbi.ac.ke)

Signature 

Date: 08/03/2023

## **DECLARATION**

To Almighty God for the ability, wisdom, and resources, and my family for constant prayer, encouragement, moral, and material support.

## **ACKNOWLEDGEMENT**

Special gratitude is accorded to Dr. Geoffrey Bosire, Prof John Onyari, and Prof Julius Mwabora for their constructive critique, patience, resources, guidance, and mentorship which have directly contributed to the successful completion of this thesis. Sincere gratitude also goes to the personnel and institution of Worcester Polytechnic Institute (WPI) for allowing me to access key instruments and materials core for this research. Providing and allowing me to use the 3-D printer and printing filaments was instrumental in the successful completion of this study. Thank you.

For their technical and intellectual support, my appreciation goes to Kelvin Karanja, Lab in-charge Bata shoe Kenya for assistance in the determination of the polymer samples' mechanical properties, Mr. Bett of the University of Nairobi, Department of Physics, for assisting during the 3-D printing process, Prof Philiswa Nomgongo of the University of Johannesburg, Department of Chemical Sciences for her assistance in recording Size exclusion microscopy (SEM) images.

Solomon Chogo of the International Centre of Insect Physiology and Ecology (icipe) who assisted in carrying out antimicrobial tests, Ephraim Muriithi who offered MS training and Dr. Elizabeth Ndunda of Machakos University, Department of Chemistry, who assisted with Material Studio Software (V.2021).

## ABSTRACT

Polymeric materials have outpaced all other materials used in housing, packaging, building, as well as other applications. Most countries have sought aggressive mitigation measures to address the threat of global warming and the disappearance of numerous species caused by carbon emissions from the use of fossil fuels and the plastic upsurge. One of the areas currently exploited to generate products with predetermined eco-friendly products is additive manufacturing (AM) or 3-D printing. Guided by computer-aided designs (CAD), the rapid prototyping technique generates complicated yet perfectly aligned structural geometries, increasing the probability of stronger polymeric structures. The strategic focus has been on recent advancements in 3-D printing, in the context of emerging fabrication designs and mechanisms, polymeric materials, and applications.

In this study, the structural, electrical, and optical features of printed bottling products were characterized using ab initio structural simulations as well as experimental methods. The density functional theory (DFT) analysis of zinc oxide nanoparticles, copper oxide nanocrystals, polylactic acid (PLA), and acrylonitrile butadiene styrene (ABS), was accomplished using the material studio (MS) software modules including Cambridge Serial Total Package (CASTEP), blends and adsorption. This study combined computational chemistry perspectives and nanotechnological improvements to PLA and ABS and consequently, 3-D printing of dispenser pumps and bottle caps. Further, the study investigated their mechanical and antimicrobial properties. The bottle caps and dispenser pumps were designed using Autodesk fusion 360 software and imported into the slicing software (Ultimaker Cura). Fused filament fabrication technique was employed to produce PLA dispenser pumps in a 3-D printer. Computer simulations of the polymers and nanomaterials were done using material studio software V.2021. Characterization of the designed dispenser pumps was done by employing various spectroscopic techniques including; SEM, NMR, FTIR, Raman spectroscopy, and XRF.

PLA and ABS have band gap energies of 1.899 and 2.539 eV, respectively. This meant that PLA and ABS were both semiconductors. This was also supported by the existence of diverse orbitals from conduction and valence bands, which contributed to these materials' improved optical properties. The PLA-ZnO, PLA-CuO, ABS-ZnO, and ABS-CuO blends were determined to be immiscible. This was revealed by the positive values of the chi parameter, mixing, and free energies. PLA-ZnO, PLA-CuO, ABS-ZnO, and ABS-CuO blends also exhibited an adsorption

energy of -92.4846, -654.8616, -35.43790, and -5.9236 kcal/mol respectively hence an exothermic reaction. The SEM observations showed good compatibility between the printed layers while the FTIR and NMR revealed that both PLA and ABS backbones remained intact and there was no addition of any impurity. The elemental composition test indicated both polymers had dominant silicon and titanium ranging at 550.0, 416.0 ppm, and 1020, 9.490 ppm respectively. They both had almost similar concentrations of potassium metal reported to be 98.7 ppm and 92.2 ppm. Mechanical parameters like elongation at break and tensile strength were demonstrated using grey PLA and orange ABS grades with an infill percentage of 80. The co-precipitation approach was utilized to synthesize zinc oxide and copper oxide nanocrystals with enhanced antimicrobial properties against *Escherichia coli* and minimal effect on *Bacillus thuringiensis*. This is supported by the observed inhibition zones of 376.91mm and 110.34mm respectively.

Considering that PLA is biodegradable and hence greener, the findings will serve as a springboard for further study on PLA modification, resulting in polymer composites and blends with properties similar to those used in the packaging industry. Computer simulations provided scientific data on mechanical properties such as the Poisson's ratio of 0.339 that supplemented experimental investigations of 0.331 published elsewhere in the literature. From the findings of this study, the bottling products were fabricated using 3-D printing technology. In addition, the synthesized zinc oxide and copper oxide nanoparticles exhibited antimicrobial properties against *Escherichia coli* and *Bacillus thuringiensis*.

## TABLE OF CONTENTS

DECLARATION .....	ii
DECLARATION .....	iii
ACKNOWLEDGEMENT .....	iv
ABSTRACT .....	v
TABLE OF CONTENTS .....	vii
LIST OF TABLES .....	xii
LIST OF FIGURES .....	xiii
LIST OF SCHEMES .....	xv
ABBREVIATION AND SYMBOLS .....	xvi
CHAPTER 1: INTRODUCTION .....	1
1.1: Background .....	1
1.2: Statement of the problem .....	3
1.3: Objectives.....	3
1.3.1: General Objective .....	3
1.3.2: Specific objectives .....	4
1.4: Justification .....	4
1.5: Research hypothesis .....	5
1.6: Research questions .....	5
1.7: Scope of the study .....	5
CHAPTER 2: LITERATURE REVIEW .....	7
2.1: Lactic acid .....	7
2.2: Polymerization of polylactic acid .....	7
2.2.1: Direct condensation polymerization .....	7
2.2.2: Ring-opening polymerization.....	7
2.3: Applications of polylactic acid.....	8

2.4:	PLA structure, morphology and parameters .....	9
2.4.1:	Crystal structure .....	10
2.4.2:	Tensile structure .....	10
2.4.3:	Avrami parameters .....	10
2.5:	PLA plastics in solid wastes and degradation process.....	11
2.5.1:	Quantification of PLA polymers in wastes .....	11
2.5.2:	Current trends in reuse and recycling .....	11
2.5.2.1:	Recuperation of the scrap polylactic acid product .....	11
2.5.2.2:	Restabilization.....	12
2.5.2.3:	Modification of the PLA structure .....	12
2.5.2.4:	Recycling of PLA.....	12
2.6:	PLA and nanotechnology in the industry.....	12
2.7:	PLA blends and composites .....	13
2.8:	Acrylonitrile-butadiene-styrene.....	13
2.9:	Plastic wastes management strategies .....	14
2.9.1:	Landfills .....	14
2.9.2:	Plastic incinerations .....	14
2.9.3:	Recycling .....	15
2.10:	Antimicrobial effects of nanoparticles.....	15
2.11:	Additive manufacturing techniques for PLA and ABS polymers .....	16
2.11.1:	Extrusion-based methods .....	16
2.11.2:	Photopolymerization (light-induced) methods.....	17
2.11.3:	3-D powder binding technology.....	17
2.12:	Mass Balance models in 3-D printing .....	19
2.13:	Models of Multi-material 3-D printing of viscoelastic inks .....	19
2.13.1:	Models used in Fused Deposition Modelling.....	20
2.13.2:	Stereolithography models .....	21



2.13.3:Selective Laser Sintering models .....	21
2.14: Photo resins for additive manufacturing .....	22
2.14.1:Radical systems .....	22
2.14.2:Cationic Systems .....	26
2.14.3:Light Absorbers .....	26
2.15: Printing Materials and binders .....	27
2.16: 3-D dispensing processing techniques.....	28
2.16.1:Light absorbers .....	28
2.16.2:3-D fiber deposition.....	28
2.16.3:3-D bio plotting .....	28
2.17: 4-D printing.....	28
2.18: Applications of 3-D and 4-D printing.....	29
2.18.1:Biomedical Applications.....	29
2.18.2:Fashion Industry .....	29
2.18.3:Electronic industry and energy.....	30
2.18.4:Construction, architecture and automotive industry.....	30
2.19: Computational analysis of additive manufacturing polymers.....	30
<b>CHAPTER 3:MATERIALS AND METHODS .....</b>	<b>32</b>
3.1: Reagents and instruments .....	32
3.2: Characterization of PLA and ABS theoretically using Materials-Studio-based computational simulations .....	32
3.3: Fabricating bottle caps and dispenser pumps using 3-D printing guided by CAD ..	37
3.3.1: Bottle caps.....	37
3.3.2: Dispenser pumps .....	39
3.4: 3-D printing of bottle caps and dispenser pumps .....	40
3.5: Characterization of the 3-D printed ABS and PLA specimen .....	41
3.5.1: Scanning Electron Microscopy (SEM).....	41

3.5.2: Nuclear Magnetic Resonance.....	41
3.5.3: Fourier Transform Infrared Spectroscopy .....	41
3.5.4: Raman Spectroscopy .....	42
3.5.5: Energy dispersive X-ray fluorescence spectroscopy .....	42
3.6: Determination of mechanical and antimicrobial properties of the designed bottle caps and dispenser pumps.....	43
3.6.1: Preparation of tensile sample specimen.....	43
3.6.2: Synthesis of nanoparticles.....	46
CHAPTER 4: RESULTS AND DISCUSSIONS .....	48
4.1: Theoretical characterization of PLA and ABS using Material-Studio-based computational simulations. ....	48
4.1.1: Geometrically optimized structural models. ....	48
4.1.2: Electronic Properties of PLA and ABS .....	49
4.1.2.1. Band Structure.....	49
4.1.2.2. Density of States.....	50
4.1.2.3. Projected Density of States .....	51
4.1.2.4. Electron Density .....	52
4.2: Work function .....	53
4.3: Optical properties .....	54
4.3.1: Conductivity.....	54
4.3.2: PLA and ABS absorption coefficients.....	55
4.4: Adsorption of CuO and ZnO nanoparticles on PLA and ABS surfaces.....	55
4.4.1: Geometrically optimized structural models. ....	59
4.5: Miscibility of PLA-ZnO, PLA-CuO, ABS-ZnO and ABS-CuO nanoparticles .....	59
4.5.1: Phase diagrams .....	59
4.5.2: Flory-Huggin’s interaction parameters and mixing energies.....	60
4.5.3: Free energies .....	62
4.6: Fabricating bottle caps and dispenser pump .....	63

4.6.1: Bottle caps.....	63
4.6.2: Dispenser Pumps.....	64
4.7: Characterization of the 3-D printed dispenser.....	64
4.7.1: Scanning electron microscopy.....	64
4.7.2: Nuclear Magnetic Resonance (NMR).....	65
4.7.3: Fourier Transform Infrared (FTIR).....	67
4.7.4: X-ray Fluorescence.....	68
4.8: Determination of mechanical properties of the designed bottle caps and dispenser pumps.....	69
4.9: Characterization of Zinc Oxide and Copper Oxide.....	70
4.10: Antimicrobial activity of ZnO and CuO nanocrystals.....	71
CHAPTER 5: CONCLUSIONS AND RECOMMENDATIONS.....	74
5.1: Conclusions.....	74
5.2: Recommendations.....	74
REFERENCES.....	76
APPENDICES.....	96
I. Zinc Oxide crystal structure.....	96
II. Copper oxide crystal structure.....	96
III. Blending of PLA, ABS, Zinc Oxide and Copper Oxide nanoparticles.....	97

## LIST OF TABLES

Table 1:Summary of different 3-D printing processes and techniques.....	18
Table 2:The 3D printer parameters used for printing .....	41
Table 3:Specimen (V D 638-89 ASTM) dimensions.....	45
Table 4: Lattice parameters for PLA and ABS crystals .....	49
Table 5:PLA and ABS bond population and bond lengths .....	50
Table 6a: Adsorption energy of PLA-ZnO and PLA-CuO interactions.....	58
Table 6b: Adsorption energy of ABS-ZnO and ABS-CuO interactions.....	58
Table 8:Elemental composition of PLA and ABS obtained in ppm (parts per million) .....	69
Table 9:Mechanical properties of the 3D printed PLA and ABS samples.....	70
Table 10:Inhibition measurements of zinc oxide nanoparticles .....	73

## LIST OF FIGURES

Figure 1: Lactic acid enantiomers' structures .....	7
Figure 2: Reaction paths for production of poly (lactic)/polylactide acid .....	8
Figure 3: PLA structure (Otieno <i>et al.</i> , 2022).....	9
Figure 5: Selective laser sintering machine working based on the 3-D power binding technology principle (Nath & Nilufar, 2020). .....	18
Figure 6: Type1 radical photoinitiators.....	24
Figure 7: Structures for meth (acrylate) monomers for additive manufacturing. ....	26
Figure 8: A light absorber for AM photo resin.....	27
Figure 9: (a) PLA, (b) ABS, (c) 3D printer (WPI, USA), (d) PLA 3D-printed bottle caps, & (e) ABS caps) (Otieno <i>et al.</i> , 2022).....	32
Figure 10a: Illustration of computational analysis of PLA .....	35
Figure 10b: Illustration of computational analysis of ABS .....	36
Figure 11a: Virtual bottle cap designs .....	38
Figure 11b: Virtual Dispenser pump design.....	40
Figure 12: Fourier Transform Infrared spectrometer .....	42
Figure 13: Energy dispersive Xray fluorescence spectrometer .....	43
Figure 14a: Polymeric tensile test specimens.....	44
Figure 14b: Diagram of designed and printed specimen.....	44
Figure 15: Instron and Wallace hardness tester machine .....	45
Figure 16a: Reaction stages of zinc oxide nanoparticle synthesis.....	46
Figure 16b: Reaction stages of copper oxide nanoparticles .....	47
Figure 17: Upper view of optimized a) PLA and b) ABS structure. The white color denotes the hydrogen atom, grey shows carbon atom, the red color represents oxygen atom whereas blue represents the nitrogen atom. ....	48
Figure 18: Band gap structures a) PLA b) ABS .....	49
Figure 19: Density of states a) PLA b) ABS .....	51
Figure 20: Partial density crystal of states for PLA (left image) and ABS (right image) .....	52
Figure 21: Electron density a) PLA b) ABS respectively .....	53
Figure 22: computed work function ( $\phi$ ) values of PLA and ABS. The blue solid line represents the fermi level whereas the red line indicates the vacuum level. ....	54
Figure 23: PLA and ABS Conductivity .....	54

Figure 24: Absorption coefficients of PLA and ABS .....	55
Figure 25a: Adsorption of ZnO and CuO nanoparticles respectively on the polylactic acid surface. ....	56
Figure 25b: Adsorption of ZnO and CuO nanoparticles respectively on acrylonitrile butadiene styrene surface .....	57
Figure 26a: Phase diagrams of PLA-ZnO and PLA-CuO blends. The blue solid line denotes the Binodal curve, the black dot represents the critical point and the green line indicates the spinodal curve. ....	60
Figure 26b: Phase diagrams of ABS-ZnO and ABS-CuO blends .....	60
Figure 27a: Mixing energies for PLA-ZnO and PLA-CuO blends against temperature .....	61
Figure 27b: Mixing energies for ABS-ZnO and ABS-CuO blends against temperature.....	61
Figure 28a: Free energies of PLA-ZnO and PLA-CuO blend against mole fractions .....	62
Figure 28b: Free energies of ABS-ZnO and ABS-CuO blend against mole fractions .....	63
Figure 29a: Virtual (a) and printed models (b and c) of bottle caps .....	63
Figure 29b: Virtual and printed model dispenser pump.....	64
Figure 30a: SEM images for PLA .....	65
Figure 30b: SEM images for ABS .....	65
Figure 31: PLA (a) and ABS (b) <sup>1</sup> H-NMR spectra.....	66
Figure 32a: FTIR spectra of PLA and ABS .....	68
Figure 32b: Raman spectrum of PLA .....	68
Figure 33: FTIR spectra of ZnO and CuO nanoparticles. ....	71
Figure 34: Antimicrobial activity of ZnO and CuO Nanocrystals.....	72
Figure 35: Zinc oxide 3D structure .....	96
Figure 36: Copper oxide 3D structure.....	97
Figure 37a: PLAZnO and PLACuO blends respectively .....	98
Figure 37b: ABSZnO and ABSCuO blends respectively .....	<b>Error! Bookmark not defined.</b>

## LIST OF SCHEMES

Scheme 1: Nature of the study.....	6
Scheme 2: Synthesis of acrylonitrile butadiene styrene (Ebewele, 2000). The x, y, and z represent the number of repeating units in ABS.....	14
Scheme 3: Photocleavage mechanism for a darocur 1173 .....	23
Scheme 4: Radical generation from benzophenone (Type 2 photoinitiator).....	24
Scheme 5: Generation of thiol radical.....	25
Scheme 6: Structures of a) PLA b) ABS .....	66

## ABBREVIATION AND SYMBOLS

3-D	Three Dimensional
4-D	Four Dimensional
ABS	Acrylonitrile Butadiene Styrene
AM	Additive Manufacturing
ANOVA	Analysis of Variance
ASTM	American Society for Testing and Materials
BAPO	(2,4,6-trimethylbenzoyl)-phosphine oxide
BFGS	Broyden-Fletcher-Goldfarb-Shannon
BMSB	1,4-bis(2-dimethylstyryl) benzene.
CAD	Computer Aided Design
CASTEP	Cambridge Serial Total Package
CMC	Carboxymethyl Chitosan
COMPASS	Condensed Phase Optimized Molecular Potentials for Atomic Simulation Studies
CuO	Copper Oxide nanoparticles
DFT	Density Functional Theory
DGEBA	D(M)A -bisphenol A diglycidyl ether
DLP	Digital light Processing
DOS	Density of States
DPGA	Dipropylene glycol diacrylate
F	Force
FTIR	Fourier Transform Infra-Red
GDP	Gross Domestic Product
GGA	Generalized Gradient Approximation
H	Laser radiation
K	Consistency index
M	Molar
MS	Material Studio
$N_B$	Pressure gradient reduced factor
NaOH	Sodium hydroxide
NMR	Nuclear Magnetic Resonance
NPS	Nanoparticles



$^{\circ}\text{C}$	Degree Centigrade
PBE	Perdev-Burke -Ernzehorf
PBT	Poly (butylene terephthalate)
PCL	Polycaprolactone
PDOS	Projected Density of states
PEG	Polyethylene glycol
PEGT	Poly (ethylene glycol)-terephthalate
PET	Polyethylene Terephthalate
PGA	Polyglycolic Acid
PHG	Polymer hydrogel
PLA	Polylactic acid
PLGA	Poly lactide-co-glycolic acid
PP	Polypropylene
PVA	Polyvinyl Alcohol
Q	Heat transfer
Re	Reynolds number
$S_f$	Filament's cross-sectional area
SEM	Size Exclusion Microscopy
SLS	Selective laser sintering
STL	Stereolithography (file format)
T	Temperature
$T_g$	Glass transition temperature
$T_m$	Melting temperature
$\text{TiO}_2$	Titanium dioxide
TPO	Diphenyl (2,4,6-trimethyl benzoyl) phosphine oxide
UV	Ultra violet
$W_e$	Weber number
XRF	X-ray Fluorescence
ZnO	Zinc Oxide
Å	Armstrong.
$\alpha$	Alpha
$\beta$	Beta
$\gamma$	Shear rate

$\tau$	Shear stress
$\eta$	Viscosity
$\rho$	Density
$\mu\text{l}$	Microliter
$n$	Flow index
$Q$	Volumetric flow rate
$V$	Speed
$\Omega$	Domain of interest
$\Phi$	Work function
$C_e$	Unabsorbed adsorbate
$K_L$	Langmuir constant
$q_m$	Maximum adsorption capacity
$q_e$	Adsorbed adsorbate

## CHAPTER 1: INTRODUCTION

### 1.1: Background

Polymeric materials are becoming increasingly popular due to their versatility and uses in a variety of industries. According to reports by (Borrelle *et al.*, 2020), the petrochemical sector invested more than \$204 billion in the shale gas rapid growth in sales, resulting in a predicted rise in virgin plastics production to the environment (Otieno *et al.*, 2022). Plastics have outperformed all other materials used in housing, building, packaging, and other uses. With the prospect of extinction of numerous species and the global warming crisis caused by carbon emissions from plastic pollution and application of fossil fuels, most countries have pursued aggressive climate change mitigation measures (Borrelle *et al.*, 2020; Lebreton & Andrady, 2019). In addition, the increased distribution of plastic waste due to high human population has resulted to reduced water percolation and aeration in most of our agricultural lands and blockage of the sewage lines hence acting as breeding grounds for most disease-causing vectors (Alda-Vidal *et al.*, 2020; Silva *et al.*, 2021). Numerous plastic additives have been identified to be endocrine disruptors and carcinogens. These harmful chemicals through inhalation, ingestions and skin contact harm humans (Aalto-Korte & Suuronen, 2019; Adeniran & Shakantu, 2022; Fucic *et al.*, 2018). Microplastics, often consumed by variety of freshwater and marine lives form complexes in the food chain that can pose health risks upon consumption (De-la-Torre, 2020; Smith *et al.*, 2018; Wright & Kelly, 2017). Recently, research has increasingly focused on the role of polymers across the world, with a focus on the biodegradability of polymeric products (Mangaraj *et al.*, 2019; Ryzd *et al.*, 2018).

Novel polymeric composites are already developed to improve biodegradability by incorporating natural resource reinforcements such as biofibres and organic nanofillers as an alternative to synthetic fibers (Amza *et al.*, 2021; Sathishkumar *et al.*, 2013). According to emerging technologies, adding nanoparticles to polymers creates new and co-efficient capabilities that include barrier packaging in the material industries, medical area, and nano-scaled coatings (Kamel, 2007; Otieno *et al.*, 2022; Saba *et al.*, 2014). Numerous characteristics of PLA, including degradability, could be enhanced by co-polymerization between several additional monomers such as glycolic acid to create polymers (Hu *et al.*, 2016; Jem & Tan, 2020; Murcia Valderrama *et al.*, 2020). PLA breakdown kinetics can also be accelerated under more acidic circumstances. According to (Lai *et al.*, 2012), the pre-treatment of ABS resin effluent with a micro-electrolysis device increased the decomposition of hazardous aromatic compounds and organic nitriles.

PLA has a wide range of excellent characteristics such as low shrinkage, which reduces the possibility of product deformation, good tensile strength and young's modulus, excellent optical, complete biodegradability, and high biocompatibility (Jamshidian *et al.*, 2010; Luckachan & Pillai, 2011). PLA's fundamental building blocks are optically active D (-) or L (+) enantiomers. However, the ratio of enantiomers permits for the fabrication of a diverse range of PLA grades with varying physical, optical, and mechanical characteristics (Carrasco *et al.*, 2010). Using condensation polymerization of lactic acid monomer, a high molecular weight PLA can be manufactured in the industrial setting. It can also be achieved through lactide (l, D, and D, L) polymerization under ring opening approach (Otieno *et al.*, 2022; Singhvi *et al.*, 2019) whereas ABS polymer is produced via emulsion polymerization (Zhang & Dubé, 2017). The latter happens in a heterogeneous system under an aqueous medium. A surface-active surfactant is used in stabilizing the system. During the manufacturing process, a combination of styrene, acrylonitrile monomer, surfactant, and polybutadiene latex is introduced into a continuous reactor. This is done with under pressure, temperature and time constraints (Ebewele, 2000; Otieno *et al.*, 2022). Polymerization of a mixture of these monomers under the specified conditions yields ABS with increased toughness, stiffness, chemical resistance, non-biodegradability, and excellent thermal stability (Olivera *et al.*, 2016). PLA, on the other hand, offers distinct qualities such as high processability, excellent barrier properties, and low toxicity (Dugan, 2001).

Besides its remarkable excellent properties, PLA lacks reactive side chain groups and exhibits poor toughness. This is evidenced by its characteristics of poor low heat deflection, poor heat stability, low impact strength, and charpy impact fracture of approximately  $2.5\text{kJ/m}^2$  (Domb & Kumar, 2011; Oksiuta *et al.*, 2020). To overcome these drawbacks, several modification approaches, among them annealing, chemical and physical treatments, are necessary in creating cross-linkages into the PLA polymer. The inclusion of nucleating agents, fibers, and nanoparticles, as well as blending with other polymers, could result in improved performance in terms magnetic, conduction, degradation, and antibacterial characteristics (Cifuentes *et al.*, 2017; Tan *et al.*, 2020). However, these various techniques are solely concerned with developing polymers with desired performance and blends, and they typically disregard greener solutions that reduce pollution to the environment.

This work investigates semi-empirical methods for producing and characterizing PLA and ABS caps and dispenser pumps. This was accomplished by using theoretical computations, 3-D printing, and empirical analysis of printed products. Rapid prototyping technology provides

complicated yet perfectly matched structural geometries, it is likely that harder polymeric structures will be developed, among other benefits. Computational simulations in the blends, CASTEP, and forcite modules of the Materials Studio software were used to supplement experimental data in this study. As such, the following were studied: the electronic, surface chemistry, optical and structural properties of ABS, PLA, zinc oxide and copper oxide were studied. Work function values, band gaps and density of states are examples of properties that aid in determining the stability of certain polymer structures when under temperature and pressure variations (Otieno *et al.*, 2022). In many respects, ABS and PLA properties do not differ considerably, and as such indicating that printed PLA is potentially a greener alternative to non-biodegradable polymers (such as acrylonitrile butadiene styrene, polyethylene terephthalate and polypropylene) in packaging.

## **1.2: Statement of the problem**

The production of plastics, whose applications continue to grow exponentially globally, contributes to increasing waste and waste disposal problems in the environment (Abukasim *et al.*, 2020; Andreeßen & Steinbüchel, 2019). In developing countries such as Kenya, plastic waste is ubiquitous in the environment. In recent decades, there has been enormous research and industrial effort on plastic recycling, with numerous applications of recycled plastic waste discussed in literature (Gopi & Srinivas, 2020; Imad *et al.*, 2017). Literature elsewhere revealed that the recycling process of non-biodegradable polymers such as ABS among other rigid plastics resulted in additional problems including cross-contamination and the addition of higher concentrations of adhesive materials (Niaounakis, 2013; Rujnić-Sokele, 2005). It is noteworthy, therefore, that the use of biodegradable polymeric materials as an alternative, is carving its niche in the 21st century which could grow into sustainable end-user cutting-edge technologies. Even though numerous approaches have been practiced to reduce plastic pollution, this catastrophe still exists. The utilization of biopolymers to generate new materials is a beneficial step in plastic waste reduction from the environment (van Velzen *et al.*, 2017). Regrettably, little study has been done on improvements and 3-D printing of PLA and ABS to produce materials with enhanced properties. This study combined 3-D printing, computational chemistry perspectives, and nanotechnological improvements to PLA and ABS polymers. In addition, the study empirically investigated the properties of 3-D printed products.

## **1.3: Objectives**

### **1.3.1: General Objective**

To use a semi-empirical approach in the production of bottling products through 3-D printing.

### **1.3.2: Specific objectives**

1. To theoretically characterize PLA and ABS polymers.
2. To fabricate bottling products using 3-D printing guided by CAD.
3. To characterize the properties of PLA and ABS 3-D printed bottling products.

### **1.4: Justification**

Polylactic acid has become economically attractive due to its remarkable properties such as ease of degradability, lower cost, and versatility. This biopolymer continues to gain popularity in various fields including medical, agricultural, aerospace, and textile (Abd Alsaheb *et al.*, 2015; Ebnesajjad, 2012; Sin *et al.*, 2012). Numerous publications and patents have been reported in the literature concerning various conventional manufacturing techniques for producing PLA products. It is envisaged that the use of rapid prototyping techniques commonly known as 3-D printing would help meet this rising global demand due to its flexibility and lower production cost (Shahrubudin *et al.*, 2019; Yan *et al.*, 2018; Zhou *et al.*, 2020). Besides, there are justifiable concerns over the risks involved in the release of petroleum-based polymers to different environmental systems. Therefore, using biopolymers such as PLA as an alternative option would aid in reducing environmental pollution, greenhouse gas emissions, and drainage blockages. This thesis reports the use of 3-D printing of PLA and ABS to boost the creativity of most product designers enabling them to be able to design complex structures while minimizing errors or reducing scraps that are likely to occur when using conventional molding or casting methods. This enhanced design security has limited the need for costly corrections to be carried out at later stages (Lu & Li, 2013). This disruptive technology was foreseen to eliminate the need for large production warehouses and low-level assembly workers since one could print a product upon demand hence a decrease in supply chain cost. It has been used to serve the needs of the high-end markets at lower costs in various industries including automotive, healthcare, defense, and aerospace. The creation of vastly different products in a single machine is also a disruptive element of 3-D printing, unlike conventional methods which require customized and tailored production lines. Introduction of copper oxide and zinc oxide nanocrystals are foreseen to enhance the antimicrobial properties of the designed bottle caps and dispenser pumps due to their photocatalytic sterilizing property. Theoretical analysis of the polymers using material studio-based simulations hastened the production process due to operation under optimized conditions and minimization of the construction material.

### **1.5: Research hypothesis**

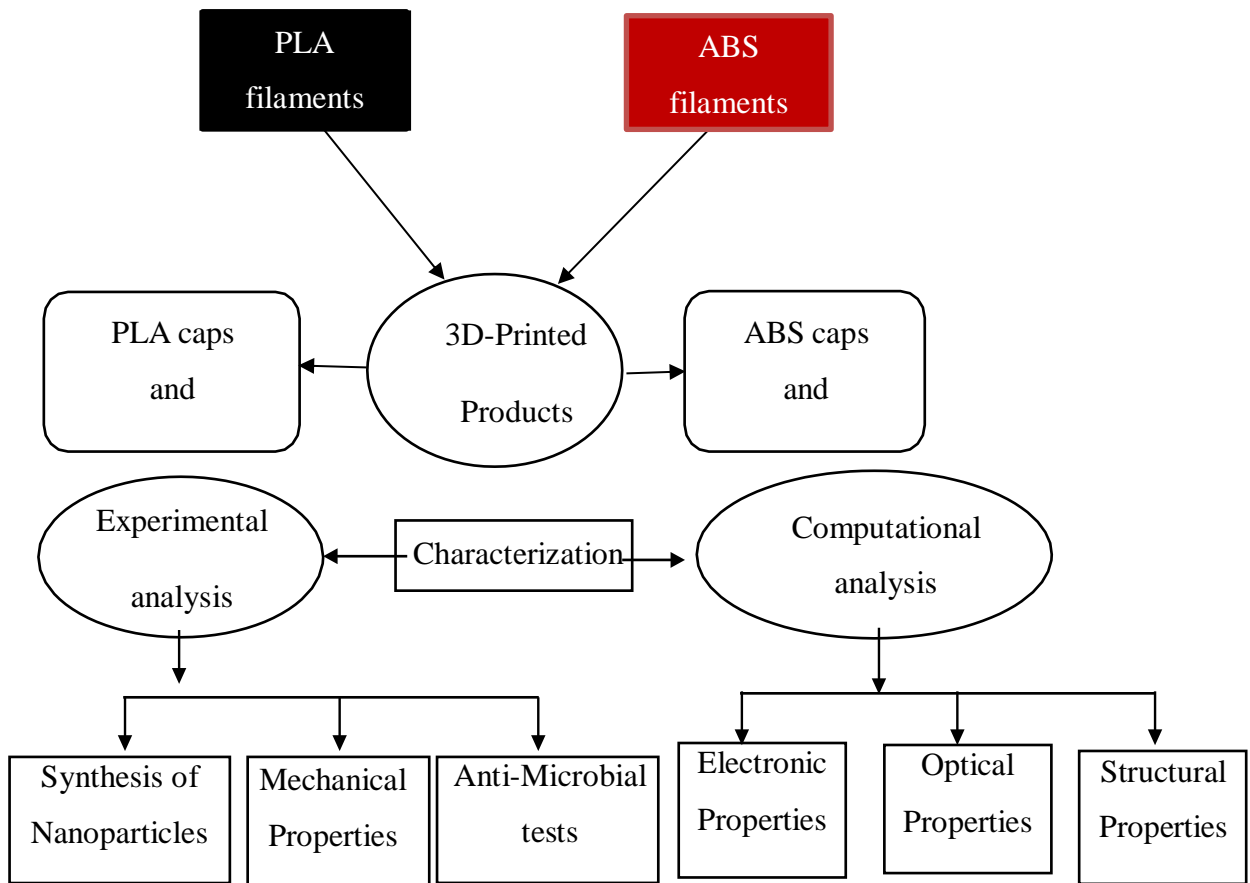
1. Autodesk fusion 360 and material studio are used to design and do molecular simulations respectively.
2. Fused filament fabrication approach is utilized to fabricate caps and dispenser pumps.
3. The designed bottle caps and dispenser pumps exhibit numerous properties including mechanical and antimicrobial.

### **1.6: Research questions**

1. How are computational simulations of PLA and ABS caps and dispenser pumps carried out?
2. Which additive manufacturing technique is used to fabricate the caps and dispenser pumps?
3. What mechanical and antimicrobial properties are exhibited by 3-D printed bottle caps and dispenser pumps?

### **1.7: Scope of the study**

The diagram in scheme 1 represents the scope of this research work where PLA and ABS printing filaments were fed into a 3-D printer to produce PLA and ABS caps and dispenser pumps from virtual models. The printed products were experimentally and theoretically characterized using material studio-based simulations.



**Scheme 1:** Nature of the study



## CHAPTER 2: LITERATURE REVIEW

### 2.1: Lactic acid

Poly(lactic acid)'s primary building block is precursory lactic acid ( $C_3H_6O_3$ ), equally referred to as 2-hydroxy propionic acid. It is generated by bacterial fermentation of renewable starch substrates such as corn and sugarcane (Ebnesajjad, 2012). As illustrated in Figure 1, it possesses two enantiomers: L (+) and D (-) lactic acid.

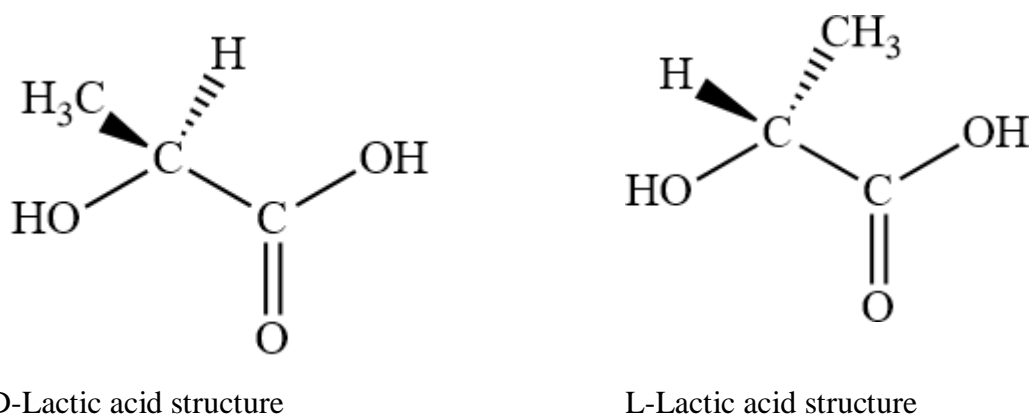


**Figure 1:** Lactic acid enantiomers' structures

Lactic acid serves as an additive during the color dyeing of fabrics, for leather tanning, in personal hygiene products as a moisturizer, and to provide the sour taste in the food industry (Auras, 2002; Henton *et al.*, 2005).

### 2.2: Polymerization of polylactic acid

#### 2.2.1: Direct condensation polymerization

PLA can be prepared through the direct condensation polymerization method (Huang & Onyari, 1996). This involves the elimination of the water molecule from polyhydroxy carboxylic acids using a solvent under higher vacuum and temperature conditions resulting in low molecular weight polylactide (Sin, 2012). This method leads to the production of oligomers with average molecular weights. The addition of coupling agents such as isocyanates and epoxides increase the molecular weights of the PLA.

#### 2.2.2: Ring-opening polymerization

This process entails the removal of water molecules without a solvent from the lactic acid monomer resulting in an intermediate dimer (lactide). Ring-opening polymerization can be

carried out by coordination insertion, cationic or anionic mechanisms. Ring-opening polymerization occurs in bulk, melt, or solution. Inclusion of stannous octoate as a catalyst is necessary to stimulate the reaction (Henton *et al.*, 2005; Huang & Onyari, 1996; Mehta *et al.*, 2005; Rujnić-Sokele, 2005; Sin, 2012).

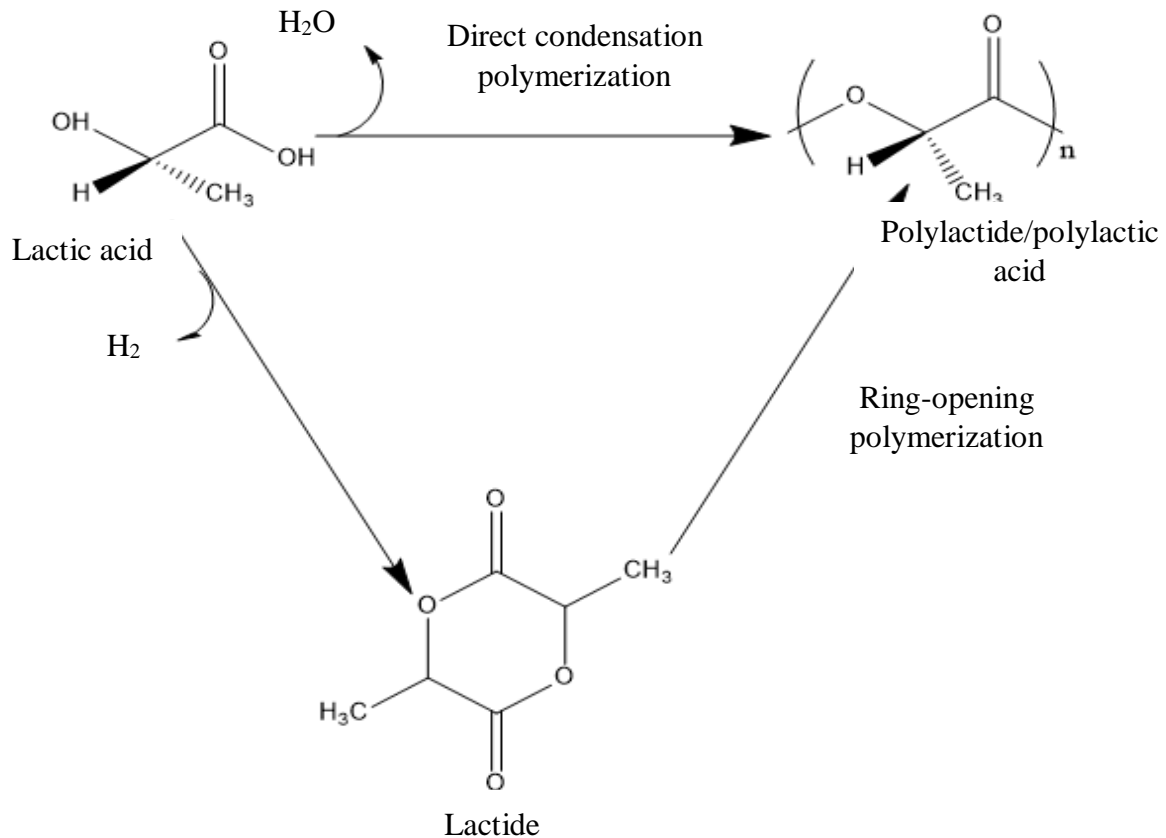


**Figure 2:** Reaction paths for production of poly (lactic)/polylactide acid

### 2.3: Applications of polylactic acid

Polylactic acid fiber is used to make garments that have low moisture and odor retention ability. It can also be used to manufacture plastic bottles which tend to deform when subjected to temperatures exceeding the glass transition temperature (60<sup>0</sup>C). These bottles exhibit desirable properties such as transparency, clarity, and good flexibility hence can easily be adaptable to the plastic processing techniques including blow and injection molding (Ebnesajjad, 2012). PLA can be used to make casings for electronic devices, fabrics, and stationery. Since it can easily be printed, it is used to make lightweight food packaging containers. According to nature works, the substitution of such products instead of several metric tons of petrochemical-derived polymers can help in the reduction of greenhouse gas emissions. It can also be used to make

disposable transaction cards since it can withstand magnetic trips and security features (Sin, 2012). Due to the biocompatibility with the living mammalian tissues, polylactic acid and its copolymer PLA/PGA (polylactide-co-glycolic acid) has been used to make screws, pins, bioresorbable sutures and scaffolds (Jadoun, 2019). It has also been used to fabricate artificial joints and bones during orthopedic surgery (Tappa & Jammalamadaka, 2018). It can also be used as a drug carrier component since it has high crystallinity and can take time to break down while releasing the active drug ingredient (Fattahi *et al.*, 2019; Vlachopoulos *et al.*, 2022). Polylactic acid can be used to make building materials such as laminated flooring materials, carpets, and wall mats which can last if well maintained. Moreover, they can easily degrade upon disposal which is contrary to the commonly used polyvinyl chloride. PLA is used as a fused filament in the fabrication of 3-D printing (Matos *et al.*, 2018; Prabhakar *et al.*, 2021). It can also be used to make socket casings and plug applications since it equally possesses good electrical properties. The polylactic acid mulch film can aid in fertilizer retention, managing the growth of weeds, and soil protection. It can later decompose providing the soil with nutrients (Sin *et al.*, 2012). It can also be used to make flowerpots which can be buried to degrade once the plant has grown enough to be planted in the ground.

#### 2.4: PLA structure, morphology and parameters

The physical characteristics of PLA are much dependent on its glass transition temperature which is about 60°C. This may affect various parameters such as density, mechanical properties, and heat capacity. It is noteworthy that glass transition as well as melting temperatures (T<sub>m</sub> and T<sub>g</sub>) are deciding factors in various applications. These transition temperatures are controlled by polymer molecular weight, thermal history, and basic structure. The structure of polylactic acid is shown in figure 3. Various properties of PLA polymer can also be determined from its Avrami parameters, tensile and crystal structure as discussed.

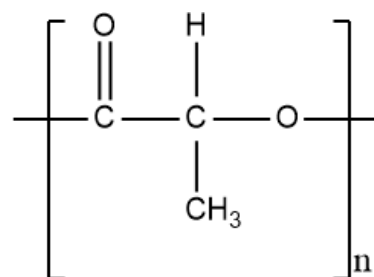


**Figure 3:** PLA structure (Otieno *et al.*, 2022)

### 2.4.1: Crystal structure

Poly(lactic acid) can crystallize into four types of crystal structure namely;  $\beta$ ,  $\alpha$ ,  $\gamma$ , and  $\eta$  (Tábi, 2019). The alpha form ( $\alpha$ ) known for its orthorhombic unit cell is the most common and stable polymorph. It is formed by crystallization of poly(lactic acid) from the melt to solid state. When alpha form ( $\alpha$ ) is subjected to higher temperatures, it results to  $\beta$  form which has a trigonal unit cell. The melt blend generated between D-lactic acid and L-lactic acid leads to the formation of the stereo-complex structure. The  $\gamma$  form is developed from crystallization of PLA on a hexamethylbenzene substrate. It also forms an orthorhombic unit cell (Tábi, 2019). It's worth mentioning that melt blending optically pure PLLA and PDLA results in the stereo complex crystal structure ( $\eta$  form) (Bouapao & Tsuji, 2009).

### 2.4.2: Tensile structure

Mechanical parameters including young's modulus, yield stress, and tensile strength have an impact on the morphological qualities of PLA polymer. The tensile response depends on polymer structure, temperature, crystallinity, and molecular weight distribution. The tensile test of poly(lactic acid) polymer can be determined using a universal test machine according to the ASTM D-638 standards (Gamez-Perez, 2010). Besides being rigid and brittle, PLA also has a specific yield point and experiences failure by neck instability (Gámez-Pérez *et al.*, 2011; Palai *et al.*, 2019).

### 2.4.3: Avrami parameters

Polymer crystallization entails polymer growth of crystals and nucleation. Kinetics of polymer crystallization from melt or dilute solutions of poly(lactic acid) will be obtained by using the Avrami model (Hortos Llobera *et al.*, 2019). It is noteworthy to mention that poly(lactic acid) crystallization is not only affected by polymer mobility but also higher temperatures which in turn influences the polymer's precipitation rate. The general Avrami law equation (Lorenzo *et al.*, 2007) is expressed by equation 1;

$$X_C = 1 - e^{-K(t-t_{induction})^n} \quad (1)$$

Where:  $X_C$  denotes the relative degree of crystallinity,  $n$  refers to the Avrami constant dependent on nucleation and crystal growth,  $t$  indicates time, and  $k$  denotes the crystallization rate constant,

The linear expression of the Avrami law is as follows;

$$\log k + n \log(t - t_{induction}) = \log(-\ln(1 - IP)) \quad (2)$$

The slope and intercepts of the above equation are used to determine the Avrami parameters  $n$  and  $K$  (Hortos Llobera *et al.*, 2019).

## **2.5: PLA plastics in solid wastes and degradation process**

The key elements influencing PLA biopolymer breakdown include molecular weight, temperature, the presence of a solvent, oxygen supply, moisture availability, and crystallinity. Amorphous polymer components are reported to be less resistant to deterioration than crystalline polymer parts. High molecular weight polymers are envisaged to decompose at a slower rate due to their entanglements caused by inhibition of hydrolysis for chain cleavage. In the presence of oxygen, polylactic acid can degrade aerobically and anaerobically. According to Kale *et al* (2007), PLA plastic bottles could take lesser years to fully decompose.

### **2.5.1: Quantification of PLA polymers in wastes**

Biopolymers have gained tremendous attention in the midst of climate change and plastic pollution. This high demand to replace general-purpose plastics in the market has curved a niche in most of our packaging industries. It is therefore important to ascertain the degradability of most biopolymers including PLA before their release to the environment. However, reports reveal that the disintegration of PLA is quite slow in the natural environment (Hottle *et al.*, 2016; Sintim *et al.*, 2020). This implies that PLA particles remain in the soil for a longer duration of time if not modified.

### **2.5.2: Current trends in reuse and recycling**

Recycling and reuse are described to be ways of managing PLA solid wastes. Reusing the PLA plastic waste is highly preferred since it requires less energy and is cost-effective. Reusing involves several steps including; recuperation of the scrap plastic during the molding process, mixing with additives to enhance the properties of the new products, polymer structure modification, and blending with other polymers to form polymer blend weight (Niaounakis, 2013). These methods have been elaborately described below:

#### **2.5.2.1: Recuperation of the scrap polylactic acid product**

This method is applicable to industrial residues obtained during processing. They are mixed with virgin materials and fed back to the processing system. Off grades of PLA formed during the polymerization reaction, runners, used PLA, defective parts during blow and injection molding and sprues are sources of polylactic acid waste. These plastic residues must first undergo heat pretreatment to obtain highly compacted and abrasion-resistant granules. The amount of heat needed for agglomeration should be considered to protect the biopolymers from

being thermally damaged. However, the concept of reprocessing polylactic acid biopolymers is a difficult task since they are bound to thermal deterioration and a decrease in molecular weight (Niaounakis, 2013).

#### **2.5.2.2: Restabilization**

Restabilization protects the polylactic acid polymer from further degradation which may be activated by the presence of some moieties in its structure or by environmental factors such as moisture and temperature. Catalyst deactivators such as benzoyl peroxide, 2-hydroxy-2,4,6-cycloheptatrienone, and 1,4-diaminoanthroquinone have been reported to stabilize polylactic acid biopolymer (Endres & Siebert-Raths, 2011; Rujnić-Sokele, 2005). Compatibilizing agents are also added to PLA biopolymer to enhance its performance

#### **2.5.2.3: Modification of the PLA structure**

Chemical modification of the polylactic acid structure is done to enhance the mechanical qualities of the PLA polymer. This can be done by the addition of chain extenders or radical generators whose properties induce crosslinking and increase molecular weight and branching (Niaounakis, 2013). The classification of the chain extenders is based on the polyester functional group with which they react. Carbodiimides, diepoxides, diisocyanates, and dianhydrides are examples of chain extenders used to improve biopolymer properties.

#### **2.5.2.4: Recycling of PLA**

Recycling biopolymers such as polylactic might prove to be beneficial to the manufacturing industry. This is because it saves on renewable energy that could be used to process a PLA monomer. It also reduces the amount of plastic waste disposed to the ecosystem since most commercial polylactic acid does not degrade under normal environmental conditions in presence of microorganisms. However, recycling PLA plastics alongside other plastics such as polyethylene terephthalate using the conventional recycling method has raised major concerns due to the anticipated contamination of the recycling stream (Niaounakis, 2013). Recycling of rigid biopolymers can be categorized into chemical and physical recycling. Physical recycling involves size reduction and separation of different polymers from a waste stream without altering the polymer(s) molecular structure while chemical recycling involves depolymerization of the polymer to recover the monomer.

### **2.6: PLA and nanotechnology in the industry**

Nanotechnology is the implementation of nanoscience that results in the use of nanostructured materials and nano-size constituents in practical products whereas the manipulation, and

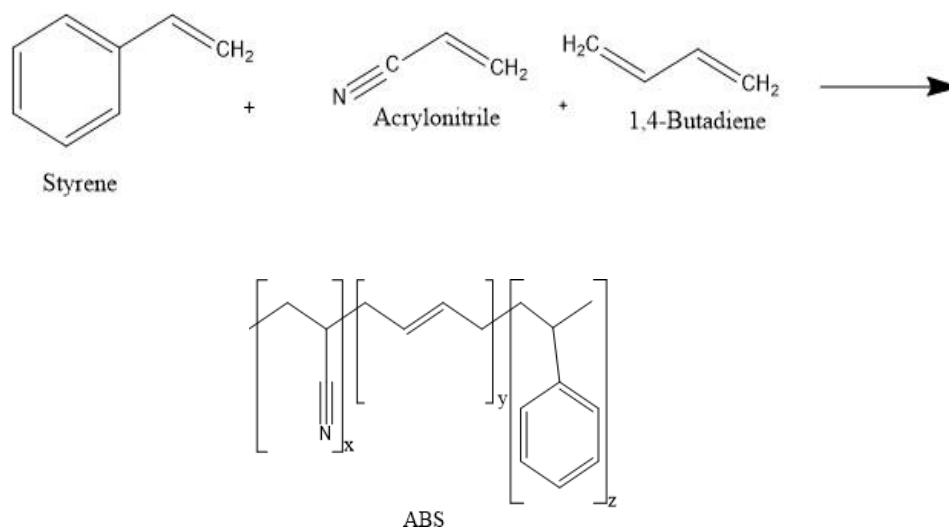
engineering of matter particles and structures at the nanometer scale is known as nanoscience. (Al-Bayati & Al-Zubaidi, 2018; Lee *et al.*, 2010). In the food industry, nanoparticles have been used to ensure bioavailability of various nutraceuticals and dietary supplements to improve stability, flavor, and act as protective barriers. The application of nanoparticles in food packaging materials made of PLA has immensely progressed given their antimicrobial properties hence they are able to extend the products' shelf life making them safe for human consumption (Heinlaan *et al.*, 2008). In addition, the incorporation of nanoparticles into packaging materials such as polylactic acid sheets would result in products with enhanced barrier and mechanical properties (Berekaa, 2015; Chaudhry *et al.*, 2010; Mihindikulasuriya & Lim, 2014). Suri *et al* (2007) reported on the use of polylactic acid copolymers (PLA-PGA) as a medication delivery strategy for poorly soluble drugs to the illness site.

### **2.7: PLA blends and composites**

Polymers are often blended to obtain desirable properties of each component. The polymers to be blended should be miscible and biodegradable. Polylactic acid can blend with poly(caprolactone), poly (ethylene oxide), poly (vinyl acetate), and poly [(R)-3-hydroxybutyrate] (Ying-Chen *et al.*, 2010). The stereoisomer polymer blends have been characterized to have better hydrolysis resistance, good thermal stability, and improved tensile properties than the individual polymers. PLA can form composites with various polymers such as PGA. These composites exhibit excellent properties among them biocompatibility and bio absorption with the tissues having the implants (Abd Alsaheb *et al.*, 2015; Ebnesajjad, 2012).

### **2.8: Acrylonitrile-butadiene-styrene**

This is a thermoplastic polymer whose copolymer composition comprises butadiene, styrene, and acrylonitrile monomers (Ebewele, 2000). It exhibits excellent electrical insulating properties, poor resistance to weak acids, and strong bases among other characteristics making it applicable in various fields to satisfy customer demands (Ziemian *et al.*, 2015). This polymer is commercially available in pellets and filament forms. Transparent, flame retardant, heat resistant, structural foam, and low gloss are examples of commercially available ABS grades (Ebewele, 2000). The emulsion polymerization process is frequently used in the industrial manufacturing of ABS polymer (Rodríguez *et al.*, 2003; Zhang & Dubé, 2018). This occurs in an aqueous medium in a heterogeneous system with a surface-active surfactant as a stabilizing agent (Ebewele, 2000; Otieno *et al.*, 2022). Free radical initiators and little amount of heat are also introduced to accelerate the conversion of the monomer droplets to the required ABS polymer (Ebewele, 2000).



**Scheme 2:** Synthesis of acrylonitrile butadiene styrene (Ebewele, 2000). The x, y, and z represent the number of repeating units in ABS.

## 2.9: Plastic wastes management strategies

### 2.9.1: Landfills

Landfills are large sites created for disposing off plastic wastes that can no longer be utilized (Huang *et al.*, 2022). They are normally used as the last option for plastic waste management. It should be noted that different plastics take varied time to degrade due to their biochemical composition, environmental conditions, and climate change. Despite the issue of degradability of the plastic waste which is perceived to take longer duration, soil, and water contamination, landfills are a source of energy as a result of the methane and carbon (IV) oxide gas produced (Huang *et al.*, 2022; Kedzierski *et al.*, 2020).

### 2.9.2: Plastic incinerations

This is the burning of plastic wastes in presence of oxygen. However, not all plastics are good candidates for combustion since some are explosives and can also be resistant to oxygen heating (Huang *et al.*, 2022; IETC, 2021). This method is attributed to several benefits such as the production of renewable energy production from wastes and huge contributions to minimizing the amount of plastic waste, reducing pollution, and preventing the production of methane gas (De Weerd *et al.*, 2020).



### **2.9.3: Recycling**

Recycling is the conversion of waste plastics into raw materials used to generate valuable products (Alabi *et al.*, 2019). This process is procedural and entails various steps including collection and sorting of plastic wastes, shredding and resizing, segregation by color and polymer, and extrusion of the various polymers in pellet form (Huang *et al.*, 2022). These pellets are later sold to the manufacturers. However, the quality of the recycled plastics depends on the type of recycling method used (Chow *et al.*, 2017; Vlachopoulos *et al.*, 2022). According to Prata *et al.* (2019), high-quality plastics are produced via primary recycling from uncontaminated materials while the secondary recycling method is applied in the production of lower-quality plastics. Even though it is not economical for most plastic manufacturers since they require a constant supply of raw materials, it possesses advantages such as saving energy and resources, reducing the need for the creation of more landfills and pollutant emissions (Zheng *et al.*, 2005).

### **2.10: Antimicrobial effects of nanoparticles**

Surface contamination by microbes poses a great health risk to human health (Klink *et al.*, 2022). However, antibiotic resistance due to continual misuse and non-compliance of antimicrobial agents has led to a rapid increase of pathogenic microbes (Padmavathy & Vijayaraghavan, 2008). Thus, effective alternative strategies are needed to control the growth of the bacteria population. The application of nanotechnology has received great attention in the eradication of microbes from surfaces (Padiyara *et al.*, 2018). Zinc oxide and copper oxide nanoparticles, for example, have been adversely known for their functional antibacterial activity. This is due to their high surface-to-volume ratio resulting in interactions between the microbial membrane and the nanoparticles (Vassallo *et al.*, 2020). According to a study reported by (Padmavathy & Vijayaraghavan, 2008), zinc oxide nanoparticles were determined to exhibit great stability under harsh conditions, biocompatibility properties, and non-toxicity to human cells. Due to its strong UV absorption properties, it has been used in various personal care products including sunscreens and deodorants (Jiang *et al.*, 2018). It is worth mentioning that zinc oxide is regarded as a safe additive by USFDA (21CFR182.8991) (Saravanan *et al.*, 2018) hence its wide application in most biosensors, antimicrobial coatings and scaffolds (Agarwal *et al.*, 2017; Klink *et al.*, 2022). Zinc oxide and copper oxide nanoparticles have been in food packaging and other coatings due to their antifungal and antibacterial properties (Duffy *et al.*, 2018). They have also been identified to exhibit antimicrobial effects against a wide

range of gram-negative and positive bacterial strains such as *Pseudomonas aeruginosa*, *Bacillus subtilis*, *Escherichia coli* 0157:H7, *Bacillus thuringiensis*, *Staphylococcus aureus*, *Campylobacter jejuni*, and *salmonella Listeria monocytogenes* (Duffy *et al.*, 2018; Jones *et al.*, 2008; Liu *et al.*, 2009).

### 2.11: Additive manufacturing techniques for PLA and ABS polymers

These techniques have been classified into three categories according to ISO/ASTM standards 52900: 2015. These categories include material extrusion, 3-D power binding technologies, and photopolymerization methods.

#### 2.11.1: Extrusion-based methods

Extrusion methods are AM processes in which thermoplastic materials are spread layer by layer in thinner threads through the nozzle to obtain a 3-D model, and are categorized into fused deposition modeling techniques, bio plotting, and direct ink writing. As illustrated in Figure 4, thermoplastic filaments are heated above their melting point and extruded in layers on the print bed in fused deposition modeling (FDM) method (Nath & Nilufar, 2020; Zhou *et al.*, 2017). According to literature, materials utilized for component manufacturing should have a relatively low shrinkage rate and glass transition temperature (Wang *et al.*, 2007). The heat energy of the extruded material determines the bond formation of the different polymeric filaments. It is also worth mentioning that the temperature history of the interfaces influences the bond quality and mechanical qualities of the final product (Sun *et al.*, 2008).

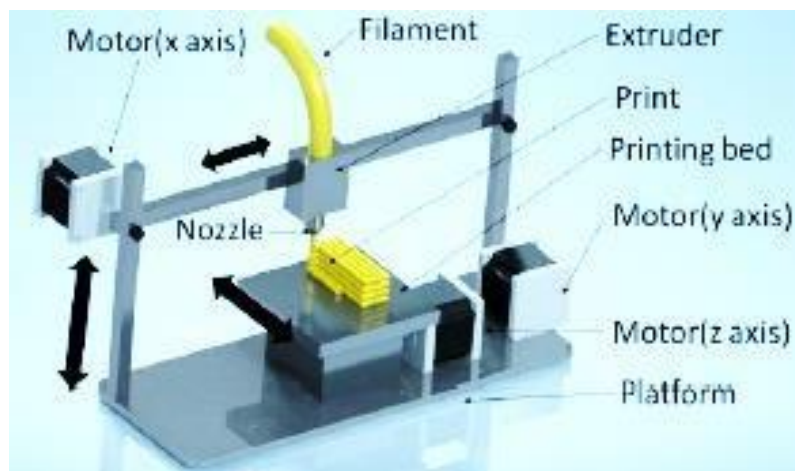


**Figure 4:** Fused deposition modeling printer working based on the material extrusion principle (Nath & Nilufar, 2020).

On the other hand, direct ink writing involves the extrusion of the printing material through a micronozzle under pneumatic pressure while utilizing a computer-guided robot to guide the dispenser printed ink (Wan *et al.*, 2020). The prototype is also generated through a layer-by-layer procedure. The bioprinting strategy involves the deposition of biomaterials onto the substrate by using a laser as the source of energy radiation. In this case, the laser irradiates the ribbon containing the biomaterials which are later deposited onto the metal film. The cell culture medium present in the receiving substrate should sustain the growth of cells and the preservation of cellular adhesion (Papaioannou *et al.*, 2019).

### **2.11.2: Photopolymerization (light-induced) methods**

Light-induced AM processes such as stereolithography, digital light processing, and electron beam melting have their liquid monomers cured by light irradiation. Of central focus is stereolithography, which involves the application of a three-dimensional computer image sliced into many cross-sectional layers approximately 150  $\mu\text{m}$  thick. It is reported that each of these slices is placed on the surface of the photosensitive material (liquid monomer) and sequentially scanned using a laser beam hence photocuring into a polymer (Park *et al.*, 2007). Distinctively, digital light processing (DLP) approach involves radiation of light on a single layer of the digital virtual model, therefore, creating layer solidification. The object is further built by continuous repetition of the same procedure along the z-axis (Gillono *et al.*, 2019). Further literature indicates that polymeric materials such as acrylic and methacrylic resins can be used since they are easily cured by photopolymerization (Frascella *et al.*, 2018). On the other hand, electronic beam melting (EBM) is a metal-free form fabrication technique that utilizes electron beams as a radiation source to melt the metallic powder (Harrysson & Cormier, 2006; Harrysson *et al.*, 2008; Zäh & Lutzmann, 2010). This process takes place under vacuum conditions and is more suitable for metals and alloys with higher affinity for nitrogen and oxygen (Harrysson *et al.*, 2008).

### **2.11.3: 3-D powder binding technology**

Selective laser sintering (SLS) (Figure 5), one of the widely applied 3-D printing technologies, involves powder materials and granules in the fabrication of a solid layer via three steps; powder deposition, solidification, and lowering the built plate by one-layer thickness (Stotko, 2009). This method is continued until the final layer is sintered. Upon exposure to laser radiation, the powder particles soften, melt and solidify at higher temperatures and pressure (Ligon *et al.*, 2017).



**Figure 5:** Selective laser sintering machine working based on the 3-D powder binding technology principle (Nath & Nilufar, 2020).

**Table 1:** Summary of different 3-D printing processes and techniques

Processes	Techniques	Materials	Advantages	Disadvantages	References
<b>Photopolymerization techniques</b>	Digital light processing	Photopolymers	Higher resolution, Numerous printable materials	Limited printing Materials	(Ligon <i>et al.</i> , 2017)
	Stereolithography	Photopolymers	High resolution	Single printing materials	(Melchels <i>et al.</i> , 2010)
	Inkjet printing	Photopolymers	Simple, multi-materials		(Guo <i>et al.</i> , 2017; Palmara <i>et al.</i> , 2021)
	Electron beam melting	Metallic photo resins	Higher resolution		(Körner, 2016)
<b>Extrusion based methods</b>	Fused deposition modeling	PLA, ABS, etc.	Versatile, simple cheaper materials and multi-materials	Lower resolution rough surfaces, high temperatures	Benwood <i>et al.</i> , 2018; Ligon <i>et al.</i> , 2017; Vidakis <i>et al.</i> , 2016)
	Bioprinting	Hydrogen composites, photo resins and thermoplastics	Broad range of printing materials	Lower resolution, lower viscosity ink required	(Ligon <i>et al.</i> , 2017; Zhang <i>et al.</i> , 2018, 2019)
	Direct ink writing	Hydrogel's thermoplastics	Numerous printing materials	Limited resolution	(Palmara <i>et al.</i> , 2021; Wan <i>et al.</i> , 2020)
<b>3-D Powder Binding Technology</b>	Selective Laser Sintering	Polyamide 12 poly(ether) ketone	Higher mechanical properties, less anisotropy	Limited range of printing materials and resolution	(Ligon <i>et al.</i> , 2017; Stotko, 2009)

## 2.12: Mass Balance models in 3-D printing

### 2.13: Models of Multi-material 3-D printing of viscoelastic inks

To illustrate the integration of function and form in 3-D-printed physical items, printing using microfluidic printheads is specifically designed for patterning viscoelastic inks. (Hardin *et al.*, 2015). As a result, the Herschel-Bulkley model, presented in equation 4, describes the rheological behavior of ink used in printing. In this equation,  $\tau$  represents shear stress,  $\eta$  indicates yield stress,  $\dot{\gamma}$  the shear rate,  $K$  is the consistency index, and  $n$  denotes the flow index associated with the ink used for 3-D printing (Hardin *et al.*, 2015; Larson, 2004).

$$\tau = \eta(\dot{\gamma})\dot{\gamma} = \tau_{\dot{\gamma}} + K\dot{\gamma}^n \quad (3)$$

Viscosity is a critical characteristic of ink and a single model equation that combines both the total pressure and flow rates is necessary. Experimental results have been corrected using the following expression, the Bagley correction (Equation 4), which shows how the actual pressure drop across the capillary ( $\Delta P_{capillary}$ ) can be determined (Jiang *et al.*, 2020).

$$\Delta P_{total} = \Delta P_{entrance} + \Delta P_{capillary} \quad (4)$$

The Weissenberg-Rabinowitsch correction is used elsewhere in literature to account for shear-thinning and to calculate the true shear rate (Hardin *et al.*, 2015) (Equation 5):

$$\dot{\gamma}_t = \frac{\dot{\gamma}_a}{3} \left[ 2 + \frac{d \ln \dot{\gamma}_a}{d \ln \tau_w} \right] \quad (5)$$

Where  $\tau_w = \frac{R}{2L} \Delta P_{capillary}$  is the shear stress and  $\dot{\gamma}_a = \frac{4Q}{R^3}$  is the shear rate of a Newtonian fluid which corresponds to the volumetric flow rate  $Q$ .

In addition, the Ohnesorge number ( $Oh$ ) (equation 6) can be used to determine the range of printability in the event that the viscosity is independent of the shear rate while having limited elasticity (Guo *et al.*, 2017). According to a discussion by Derby (2011), if  $Oh > 1$ , then the printing fluid is therefore considered viscous, requiring minimal energy to form a jet while if it is less than 0.1 then surface tension would aid in drop formation.

$$Oh = \frac{We^{1/2}}{Re} \quad (6)$$

Here,  $We$  is the Weber number and  $Re$  is the Reynolds number.

Indeed, the subjection of polymeric microfluid particles to Brownian motion may lead to the exhibition of elasticity and a laminar flow pattern through the nozzle if the  $Re < 10^{-5}$  (Hardin *et al.*, 2015). This type of model of fluid flow can be achieved using the Reynold number which is computed using the following expression (Equation 7).

$$Re = \frac{\rho v d^2}{\eta} \quad (7)$$

where  $v$  represents velocity of the smaller section of the nozzle print head,  $d$  is the nozzle diameter,  $\eta$  is the viscosity,  $\rho$  refers to density of the polymeric printing fluid. The mass balance equations for the printing material through the nozzle heads can be described using equations 8 and 9.

$$Q_{p,a}(t) - Q(t) = V_a \beta \frac{dP_a}{dt} \quad (8)$$

$$Q_{p,b}(t) - Q(t) = V_b \beta \frac{dP_b}{dt} \quad (9)$$

where  $Q_{p,a}$  and  $Q_{p,b}$  are the net volumetric flow rates exiting the nozzles. (Hardin *et al.*, 2015) reported an assumption of similar volumetric flow rates since a negligible amount of the ink was printed compared to the nozzle volume, therefore, resulting in  $v_a = v_b = v$ .

### 2.13.1: Models used in Fused Deposition Modelling

Employing the Taguchi approach and the ANOVA (analysis of variance) approach to examine the impact of various processing factors, it was determined that decreasing the layer thickness and air gap values improves the surface roughness of the printed components parts (Horvath *et al.*, 2007). The development of a factorial design led to the conclusion of using higher temperatures to obtain smooth printed parts (Horvath *et al.*, 2007). The building period of a particular design using the FDM method was predicted by a mathematical model whose results were found to agree with most published literature (Thrimurthulu *et al.*, 2004). An evaluation of various process parameters whose optimization would influence stress distribution and part distortion using the fine element models is reported in literature (Zhang & Chou, 2008). The mass balance equation obtained during the deposition of the layers in the building chamber is illustrated and discussed in literature, as shown in equation 10 (Han *et al.*, 2003).

$$V_r S_f \rho_{input} = V_h S_r \rho_{output} \quad (10)$$

Here,  $\rho_{input}$  is the density of the extruded filament,  $\rho_{output}$  represents the density of the semi-molten solid  $S_f$  refers to filament's cross-sectional area,  $S_r$  denotes road's cross-sectional

area,  $Vh$  is the table speed and  $Vr$  is the roller speed. (Stewart *et al.*, 2015) conducted a study to determine how various factors such as process control, part quality, and efficiency would affect polylactic acid melt flow pattern during the extrusion process, their conclusive data gave more insights into a range of PLA materials and extruder designs to be adopted. The melt flow properties of any Newtonian fluid in extrusion processes follows the expression of power law (Equation 11) (Bellini *et al.*, 2004).

$$\mu = K\gamma^{n-1} \quad (11)$$

where  $K$  signifies the consistency index,  $\mu$  denotes the viscosity and the power law index is represented by  $n$ . The viscoelastic behavior as well as the time variance of the melt can be reflected by the application of the tanner nonlinear constitutive equation which is expressed as shown in Equation 12 below (Liu *et al.*, 2005).

$$K \frac{dv^n}{dt} = \eta (\dot{\gamma}) \gamma = \tau + \lambda \frac{d\tau}{dt} \quad (12)$$

Since the upper part of the polymer does not fully melt, the Bagley correction method is therefore used to correct the pressure gradient which is then given by Equation 13:

$$\frac{dp}{dz} = \Delta P/L + RN_B \quad (13)$$

where  $R$  is the radius of the upper part of the extruder and  $N_B$  is the pressure gradient revised factor (Jiang *et al.*, 2020).

### 2.13.2: Stereolithography models

According to Tang and coworkers, the polymer radicals, and monomers mass balance equations 13 and 14 obtained during the stereolithography technique expounds on the various mass transfer processes such as diffusion (Tang *et al.*, 2004).

$$\frac{d[M]}{dt} = D_M \left\{ \frac{d^2[M]}{dx^2} + \frac{d^2[M]}{dy^2} + \frac{d^2[M]}{dz^2} \right\} + (-R_p) \quad (14)$$

$$\frac{d[P.]}{dt} = D_{P.} \left\{ \frac{d^2[P.]}{dx^2} + \frac{d^2[P.]}{dy^2} + \frac{d^2[P.]}{dz^2} \right\} + (-R_t) \quad (15)$$

$[M]$  and  $[P.]$  are represented by  $Q$ , which is often assumed to be equal within a given temperature and monomer concentration.

### 2.13.3: Selective Laser Sintering models

Papadakis and team (2014) suggested factors including oxygen content in the atmosphere, type of powder material and powder thickness to be considered during the SLS technique besides

laser power and laser scanning speed. The laser energy density in Equation 16 is important in ensuring adequate melting of the powder particles while minimizing scenarios that would lead to uneven surface finishes and increased porosity (Hussein *et al.*, 2013).

$$\text{Laser energy density} = \frac{\text{Laser Power}}{\text{Scanning speed} * \text{spot size}} \quad (16)$$

The Gaussian Beam model is reported as the most common laser model used to locate maximum intensity and distribute it from the beam axis using its irradiance profile (Hussein *et al.*, 2013). Considering the molten pool stability as an important phenomenon in the determination of the built quality and balling, predictions on the size of the molten tool and the resultant porosity using Rosethanl's equation are discussed in literature Tang *et al.*, 2015). Deposition of particles by allowing them to settle into different layers by gravity enables the determination of the equation of motion of the nth particle by application of Newton's second law of motion.

$$m_i x_i = F_i^{total} = F_i^{con} + F_i^{env} + F_i^{fric} + F_i^{grav} \quad (17)$$

In Equation 17, m represents the mass, F represents force, x represents position, Frictional force  $F_i^{fric}$ , contact force  $F_i^{con}$ , environmental force  $F_i^{env}$ , and force due to gravity  $F_i^{grav}$ .

In the event of particle thermal effect, the integrated equation for a particle with a uniform temperature field is given by Equation 18:

$$\int_{\partial\Omega} Q \cdot ndA + \int_{\Omega} HdV = \int_{\Omega} \rho c \dot{T} \quad (18)$$

where Q is the heat transfer, H accounts for laser radiation input,  $\rho$  is the density, T is temperature,  $\Omega$  domain of interest and c represents the constant pressure specific heat capacity of the printing material.

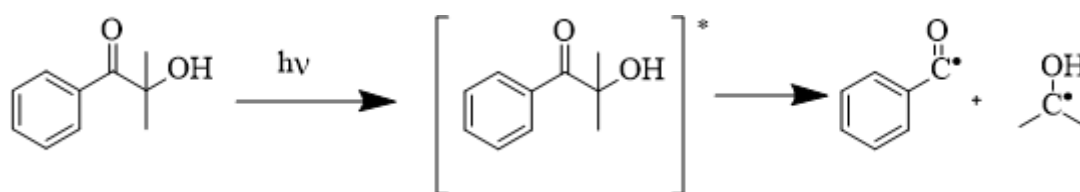
## 2.14: Photo resins for additive manufacturing

### 2.14.1: Radical systems

Radical photoinitiators absorb light, therefore, converting photocatalytic energy to reactive species which can induce polymerization. Radical photoinitiators are classified into two categories; Norrish type 1 and 2. Type 1 initiators cleave to the radical fragments upon exposure to light at a given wavelength. According to (Ficko *et al.*, 2005), benzil ketals are the most common examples of type 1 initiators with lower energy transitions. The photocleavage

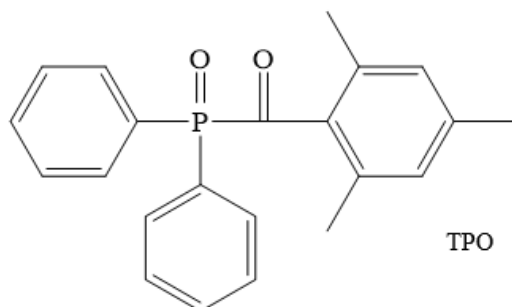
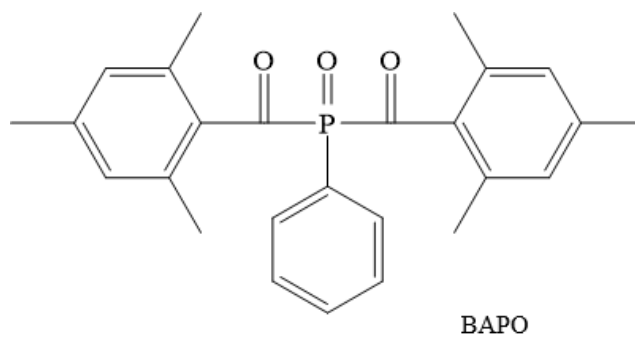


mechanism for type 1 initiators such as Darocur 1173 (scheme 3) results to direct cleavage of the excited singlet state.



**Scheme 3:** Photocleavage mechanism for a darocur 1173

Besides Darocur 1173, other type 1 benzil ketal initiators include Irgacure 369, Irgacure 651, and acyl phosphines oxides (BAPO and TPO) (Green, 2010). Type 1 photoinitiators are suitable for application in digital light processing technique.



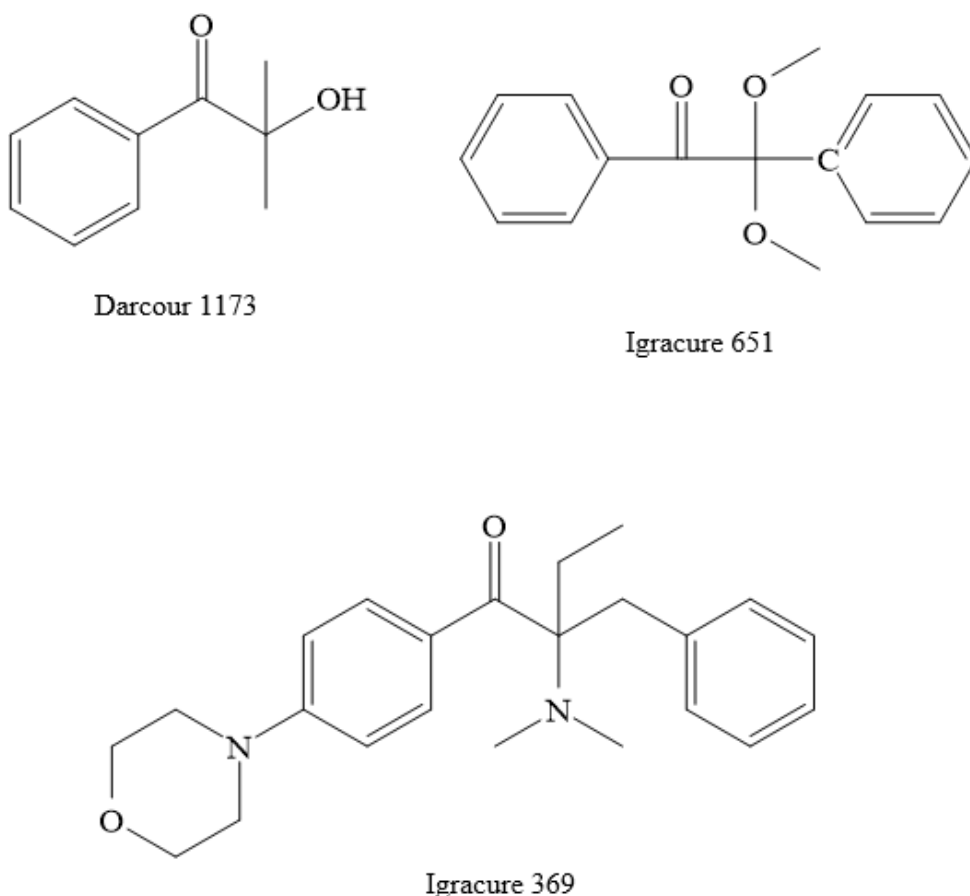
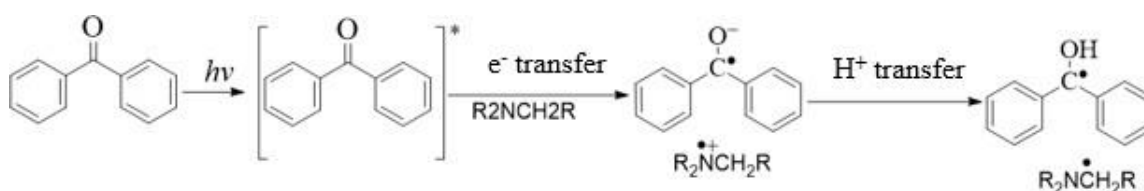


**Figure 6:** Type 1 radical photoinitiators

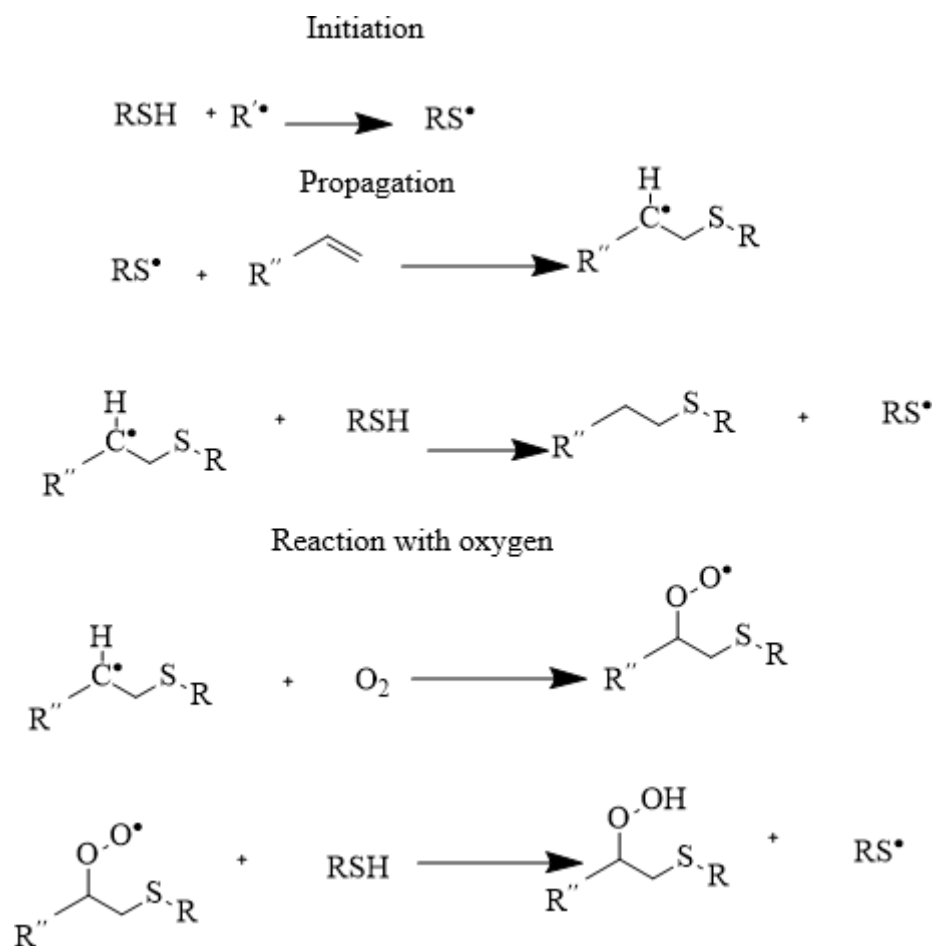
A light absorption molecule and a co-initiator are used in type 2 initiator systems. Upon radiation, the co-initiator donates a hydrogen atom to the stimulated absorbing molecule. Benzophenone and isopropylthioxanone are examples of type 2 co-initiators. The light-absorbing molecule can directly abstract hydrogen molecules from the monomer or solvent hence resulting in radical polymerization (Scheme 4).



**Scheme 4:** Radical generation from benzophenone (Type 2 photoinitiator)

Thiol-Yne and Thiol-Ene systems; these photo resins are used as an alternative to replacing the acrylates which are bound to shrinkage during polymerization. By donating hydrogen to a

peroxyl radical, thiols eliminate oxygen inhibition, which leads to the production of a thiol radical (Hoyle & Bowman, 2010) (Scheme 5).



**Scheme 5:** Generation of thiol radical.

(Meth)acrylate monomers; involve the application of bisphenol A diglycidyl ether (DGEBA) and acrylate-based resins such as urethane acrylates and methyl methacrylate resins. Good mechanical strength is attributed to their functional groups. Aliphatic or aromatic urethane acrylates are commercially available and their structural monomers are characterized to be too viscous to be used during additive manufacturing hence various reactive diluents possessing lower viscosity are added to improve their thinning ability (Joshi *et al.*, 1999; Ligon *et al.*, 2017). As shown in figure 7, reactive diluents, including dipropylene glycol diacrylate (DPGDA), accelerate resin cross-linking during polymerization.

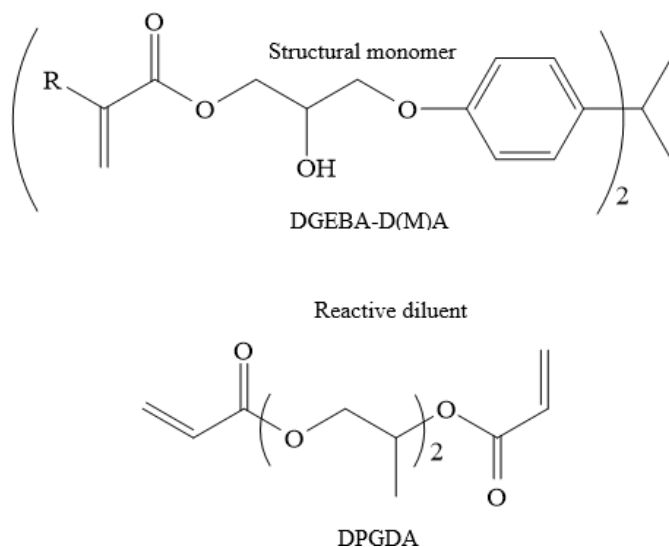


**Figure 7:** Structures for meth (acrylate) monomers for additive manufacturing.

### 2.14.2: Cationic Systems

Cationic photopolymerization was developed due to shortcomings experienced with radical polymerization. Cationic systems have been categorized into photoacid generators, epoxides, oxetanes, and vinyl ethers. According to Ligon *et al* (2017), cationic initiators such as aryl iodonium salts are attributed to thermal stability even though they decompose when subjected to UV radiation to form an intermediate consisting of cation, radical intermediate, and radicals. When the intermediate reacts to either a monomer or solvent, it leads to the formation of an initiator for acid polymerization. Epoxides monomers including DGEBA and trimethyloyl propane are commonly used for stereolithography due to their good mechanical and less shrinkage property of the resultant polymer during photopolymerization (Ligon *et al.*, 2017; Takahashi *et al.*, 2003, 2004).

### 2.14.3: Light Absorbers

Additive manufacturing resins contain various compounds besides the initiators and monomers. Radical inhibitors such as butylated hydroxy toluene is added to prevent premature gelation of acrylates. Ligon *et al* (2017) reported that 9-anthanoic acid esters have been used as stabilizers of silicone vinyl monomers. Several publications have been done on the use of pyrenes and anthracene derivatives as light absorbers for stereolithography technique (Ligon *et al.*, 2017). other light absorbers include 1,4-bis(2-dimethylstyryl) benzene (BMSB) in figure 8.

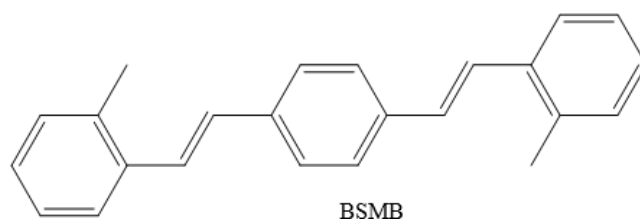


**Figure 8:** A light absorber for AM photo resin

### 2.15: Printing Materials and binders

There are two techniques commonly used to carry out printing of 2-dimensional or 3-dimensional objects namely; aerosol jet and inkjet printing. Building and support materials are required to attain lower viscosity for inkjet printing (Napadensky, 2003; Napadensky *et al.*, 2007). These materials must also have high thermal stability and cure rapidly upon exposure to light radiation. Support materials used during inkjet additive manufacturing are water soluble monomers that undergo photocuring to form weaker soluble polymers which can easily dissolve in water. Support materials may comprise polyethylene glycol (PEG), stabilizers, and silicon additives (Schmidt *et al.*, 2008). Three-dimensional systems use urethane wax which can be melted by mild heating. In scenarios where there is the addition of a supplementary component (lipase solution) is added before or after printing. Polycaprolactone-polyethylene glycol-polycaprolactone (PCL-PEG-PCL) is used as a base material (Dikovskiy & Napadensky, 2013). The Aerosol jet printing technique employs pneumatic atomization or ultra-sonification process in an aerosol chamber which involves atomizing the building materials. The materials used for pneumatic atomization should have lower viscosity approximately 2500 MPa and smaller diameters for dispersed particles (Ligon *et al.*, 2017). Ink based on single or multi-walled carbon nanotubes can be used to print conductive and semiconductive structures. Teflon and UV adhesives (polyimide) are used to develop dielectric materials and 3-D structures on a nonplanar surface. Some biomaterials commonly used for tissue engineering are printed from PLGA/TiO<sub>2</sub> nanocomposites (Liu & Webster, 2023). Binders initiate particle fusion by swelling the polymeric powder, therefore, causing entanglement. Binders might be polymer dispersion solutions or film-forming polymers. Hydrophobic polymers that include polylactic acid (PLA), polycaprolactone (PCL), and polylactide-co-glycolide (PLGA) are confined together using Inkjet printing of organic solvents. While hydrophilic powders including cement and starch need aqueous binders (Ligon *et al.*, 2017).

## **2.16: 3-D dispensing processing techniques**

### **2.16.1: Light absorbers**

This process involves thermoplastic granules which are melted and fed to the extrusion head. The melted polymer is then 3-D dispensed in micrometer-sized micro droplets which are formed under high pressure and a high-frequency piezoelectric nozzle. The polymer was then subjected to solidification ensuring layer-by-layer printing as per the computer-aided design. This process applies to polymers that do not require filaments (Gloria *et al.*, 2009; Ligon *et al.*, 2017).

### **2.16.2: 3-D fiber deposition**

Fiber deposition is a rapid prototyping technique that fabricates scaffolds possessing different properties and geometric structures. It is a modified form of the 3-D bio-plotting technique normally used for the extrusion of viscous polymers. (Gloria *et al.*, 2009) described this 3-D dispensing technique to involve extrusion and deposition of molten polymer via a syringe driven by pressure-generating scaffolds possessing defined shape, structure, size, and architecture. Using a 3-D deposition process, Woodfield *et al* (2004) developed a 3-D poly (ethylene glycol)-terephthalate- poly (butylene terephthalate) (PEGT/PBT) block copolymer for articular cartilage tissue engineering.

### **2.16.3: 3-D bio plotting**

This is a dispensing technique that employs a layer-by-layer approach in the fabrication of desired objects. This is accomplished by the application of a pressure-controlled dispenser to extrude built material that is then allowed to solidify. The dispenser nozzle is freely adjustable in all directions (Carvalho *et al.*, 2005). Bio plotting is a technique used in tissue engineering to create 3D hydrogel scaffolds without the need for conventional molds and support materials.

## **2.17: 4-D printing**

Invented at MIT's self-assembly laboratory by Skylar Tibbits, 4D printing is a technology in which printed objects can respond to external stimuli that include current, heat, light, and water (Choi *et al.*, 2015). This mode of printing regards time as its fourth dimension. With unprecedented interest in this field, 4D printing could enhance drastic reforms to product assembly, manufacturing, automobile, and biomedical sectors by discovering self-assembly and programmable material technologies for the objects to be printed. Various stimuli-sensitive materials that can be utilized in 4D printing include piezoelectric, chromo active, magnetorheological, photoactive, and shape memory materials.

## **2.18: Applications of 3-D and 4-D printing**

### **2.18.1: Biomedical Applications**

3-D printing has been widely utilized in the biomedical field for a variety of applications that include tissue engineering and medicine. According to a study done by (Khanesar, 2019), this technology has been used to make an ear model, breast reconstruction, kidney fabrication, and designing 3-D printed mandibles as anatomical structures used in facial surgical operations. 3-D printing has aided in simulating surgical and interventional procedures applied during operations of delicate human internal organs such as the brain and heart. As reported by Mondal *et al.*, (2016) poly ( $\epsilon$ -caprolactone) (PCL) based materials are gaining ground in drug delivery and medical applications. Their review revealed that PCL is easy to process and manipulate, especially in tissue engineering applications (Mondal *et al.*, 2016). Interestingly, 3-D bioprinting of this kind has gained immensely in the 21st century, as evidenced by cutting-edge applications in tissue engineering, including prosthetic materials and bio fabricated cell carrying scaffolds such as cryogenic scaffolds (Biçen Ünlüer *et al.*, 2022; Powell *et al.*, 2020). It also enables the prediction of the feasibility of the performed surgical procedures (Liacouras *et al.*, 2011; Singare *et al.*, 2008). 3-D printing application in the manufacture of various drugs has modified the dosage profile hence not only can different drugs be printed with multiple sustained PLA release layers but they can also be printed for each specified individual (Paul *et al.*, 2018). 3-D printing has also been used to mimic the replication of soft tissues as reviewed by Liacouras and team (Liacouras *et al.*, 2011). 4-D printing could be used in coming up with self-folding protein.

### **2.18.2: Fashion Industry**

Besides manufacturing pieces of jewelry, 3-D printing has opened new frontiers in the fashion sector. Some designers such as Iris Van Herpen have experimented this technology to make wearable garments (Sun & Valtasa, 2019). This technology allows for the incorporation of a variety of material properties in a single build. Schmid and Bitoni were reported to have designed the first fully articulated 3-D printed gown globally (Ligon *et al.*, 2017). Additive manufacturing technologies have also been used to fabricate face masks and face shields to be used during the COVID-19 pandemic crisis (Armijo *et al.*, 2021). The art of 4-D printing is also perceived to change the face of the fashion industry, for example; designing clothes or shoes that would change shape with respect to the environmental conditions and activity to facilitate comfort.

### **2.18.3: Electronic industry and energy**

Previous research has focused on creating 3-D printing to produce electrical and energy devices (Zhu *et al.*, 2016). Construction of 3-D and 2-D circuits utilizing polypropylene thermoplastic composite (Kwok *et al.*, 2017). Studies have shown that 3-D printing via continuous inkjet-printing using polyimide films, generates capacitor-insulating layers (Zhang *et al.*, 2016). This technology can enable the printing of sensors exhibiting great consistency, high accuracy, and various usability (Bali *et al.*, 2016; Chang *et al.*, 2015). Piezoelectric ceramic elements for ultrasonic sensing were printed using the stereolithography technique (Chen *et al.*, 2016; Sajid *et al.*, 2018). Fabrication of sound-absorbing mats using polycarbonate was achieved through additive manufacturing (Ligon *et al.*, 2017).

### **2.18.4: Construction, architecture and automotive industry**

With the frequent use of CAD models, architects have easily adopted additive manufacturing technology by enhancing visualization for their clients while reducing the potential risk of structural failure and delay in construction (Ligon *et al.*, 2017). Diverse polymeric composites and polymers have been adopted in the automobile industry to design windbreakers, exterior or interior trimmings, and car bumpers utilizing the selective laser sintering technique (Nath & Nilufar, 2020). 4-D printing would be used to develop piping systems that would repair themselves upon exposure to different stimuli. The restriction of 3-D printing based on the printer size has paved way for 4-D printing which is foreseen to create flat boards that could self-assemble into furniture when exposed to light or water.

### **2.19: Computational analysis of additive manufacturing polymers**

This is a computational approach that uses various models and theories to introduce better designs, optimize and predict the structure and material properties of various polymers (Gooneie *et al.*, 2017). Multiscale simulation is given much preference since it can predict the macroscale properties of various polymeric materials from molecular processes. The models and theories are categorized into quantum, mesoscale, atomistic, and macroscale putting into consideration time scale and characteristic length (Gooneie *et al.*, 2017). Computational simulation techniques are grouped into field and particle-based methods. In the particle-based approach, the polymer building units include monomers, polymer chains, atoms, and molecules which are represented by particles that undergo bonded interactions using a range of forces hence resulting in forcefields (Müller-Plathe, 2002). Müller-Plathe (2002) described a field-based approach to evaluate the degree of freedom of a variety of models. It entails methods such as density functional theory, phase field techniques, and polymer reference interaction



site model (PRISM) (Alkorta & Elguero, 2003; Ganesan & Jayaraman, 2014). In a study conducted on molecular simulations of polylactic acid and polyethylene glycol blends, it was concluded that time factor influenced the stability of PLA blends since crystallization resulted in phase separation from homogeneous blends (Takhulee *et al.*, 2017). (Wei *et al.*, 2019) employed the molecular dynamics method to explore the performance and microstructure of PLA/CMC composites and to determine the total and binding energies that resulted from the molecular interactions of the two polymers. In addition, it can also aid in the prediction of the glass transition temperatures of polylactic acid and polylactic acid copolymer.

## CHAPTER 3: MATERIALS AND METHODS

### 3.1: Reagents and instruments

Analytical grade chemicals: ethanol ( $\text{CH}_2\text{COOH}$ ); zinc acetate dihydrate ( $\text{Zn}(\text{CH}_3\text{COO})_2 \cdot 2\text{H}_2\text{O}$ ); copper sulfate pentahydrate ( $\text{CuSO}_4 \cdot 5\text{H}_2\text{O}$ ), sodium hydroxide ( $\text{NaOH}$ ) of 99% purity were used without purification. The stock solution was made by dissolving salt in distilled water. The Worcester Polytechnic Institute (WPI) in the United States provided the PLA and ABS polymer filaments (figures 9a and 9b). The 3-D printer came with several PLA grades (black, green, translucent, blue, and grey) and orange ABS filaments (Ultimaker<sup>2</sup>, USA). In this study, 3-D printing was done with grey, translucent polylactic acid, and orange ABS grades. The 3-D printer (Ultimaker<sup>2</sup> shown in Figure 9c) was used to fabricate packaging materials that include 3-D printed bottle caps (Figures 9d and 9e), which were then crushed into small particle sizes for characterization.

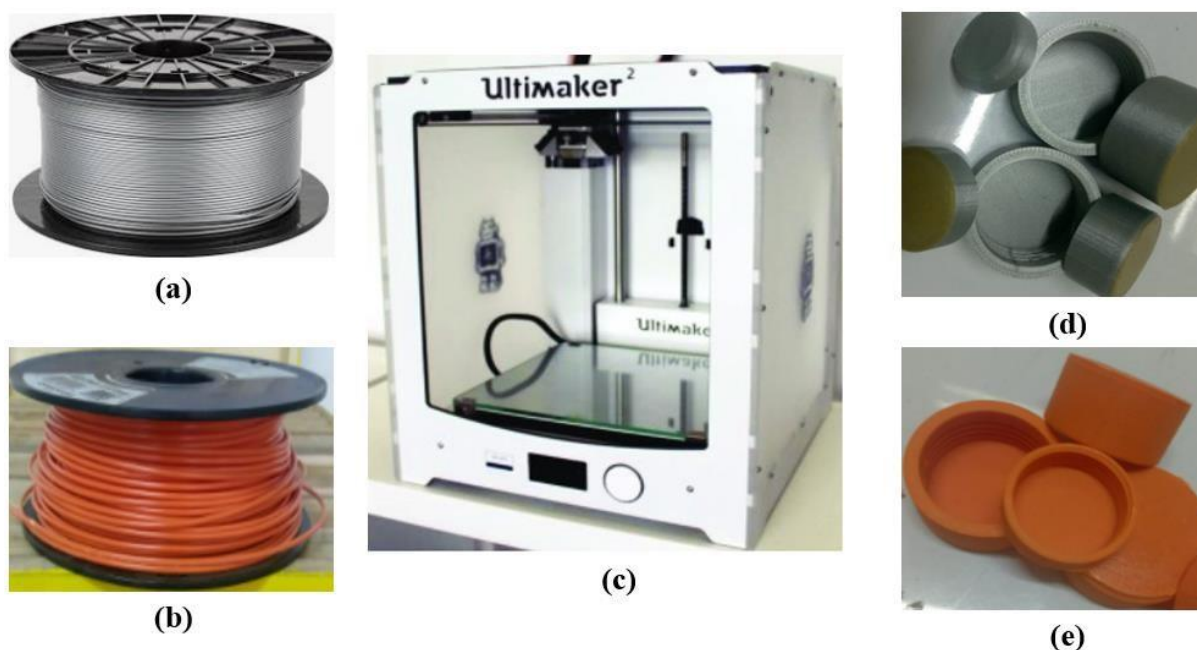


**Figure 9:** (a) PLA, (b) ABS, (c) 3-D printer (WPI, USA), (d) PLA 3-D-printed bottle caps, & (e) ABS caps) (Otieno *et al.*, 2022).

### 3.2: Characterization of PLA and ABS theoretically using Materials-Studio-based computational simulations

In calculating the first principle of quantum mechanics and density functional theory (DFT), Materials Studio software (V.2021) was used utilizing Cambridge Serial Total Energy Package

(CASTEP) module. Pristine ABS and PLA electronic, optical, and structural properties were generated using the CASTEP code. To calculate the surface and crystal characteristics of PLA and ABS, as well as the exchange-correlation and core valence electrons, the Generalized Gradient Approximation (GGA) using the Perdew-Burke-Ernzerhof (PBE) function in combination with norm-conserving pseudopotentials was employed. Brillouin zone sampling of electronic states was performed using a Monkhorst-Pack k-point of 2 x 2 x 1, a maximum permissible displacement of  $3.15 \text{ \AA}^0$ , an atomic force of 0.03 eV, the maximum stress of 0.05 Gpa, and a plane wave basis cut off the energy of 260 eV. The crystal structures of PLA and ABS were geometrically optimized using the BFGS method. To guarantee that structural changes and energy conversion were kept to a minimum, only 100 iteration steps were utilized in the evaluation of computation correctness. The requirement for further iterations might also be accounted for using the high energy configurations attributed to direct simulations of drawn polymers, which result in erroneous findings. As a result of this procedure, resemblance to genuine molecular structures was ensured. Above the 10eV maximum fermi level energy, several electronic parameters including the partial density of states, density of states, band structures, and potential profiles were determined.

Molecular dynamic simulations, using the forcite module, were used to predict mechanical properties. Analysis of interatomic interactions was done using condensed phase optimized molecular potentials for atomic simulation studies (COMPASS) forcefield. Each strain has four stages, with the greatest strain amplitude utilized being 0.003 m. It should be noted that both kinetic energy and potential energy were conserved. The projected density of states (PDOS) was simulated in this study while taking into account the contribution of each element to the interface (Otieno *et al.*, 2022). The density of states (Equation 19) expression describes the number of states present and the nature of the material at fermi level, hence determining energy and concentration distribution (Milman *et al.*, 2000):

$$N_n(E) = \int_{4\pi^3}^{dk} \delta(E - E_n(K)) \quad (19)$$

where:

$E_n(K)$  indicates electrons dispersion in a given band while  $N_n(E)$  denotes the total density of states attained by summation of n bands.

Born- Oppenheimer approximation and Schrodinger formalism can be used to determine electron density, which is frequently described as the chance of an electron being available at

a specific location. For instance, (Equation 20) gives the probability of one electron density (Bickelhaupt & Baerends, 2000).

$$\rho_1(r_1) = N \int \varphi_{el}^*(r_1, r_2, \dots, r_N; \{R\}) \cdot \varphi_{el}(r_1, r_2, \dots, r_N; \{R\}) dr_2 \dots dr_N \quad (20)$$

Where  $\varphi_{el}$  is the stationary wave function,  $\rho_1$  denotes the density of a given atom,  $r$  is electron position,  $N$  is electron number, and  $R$  is fixed nuclear coordinates.

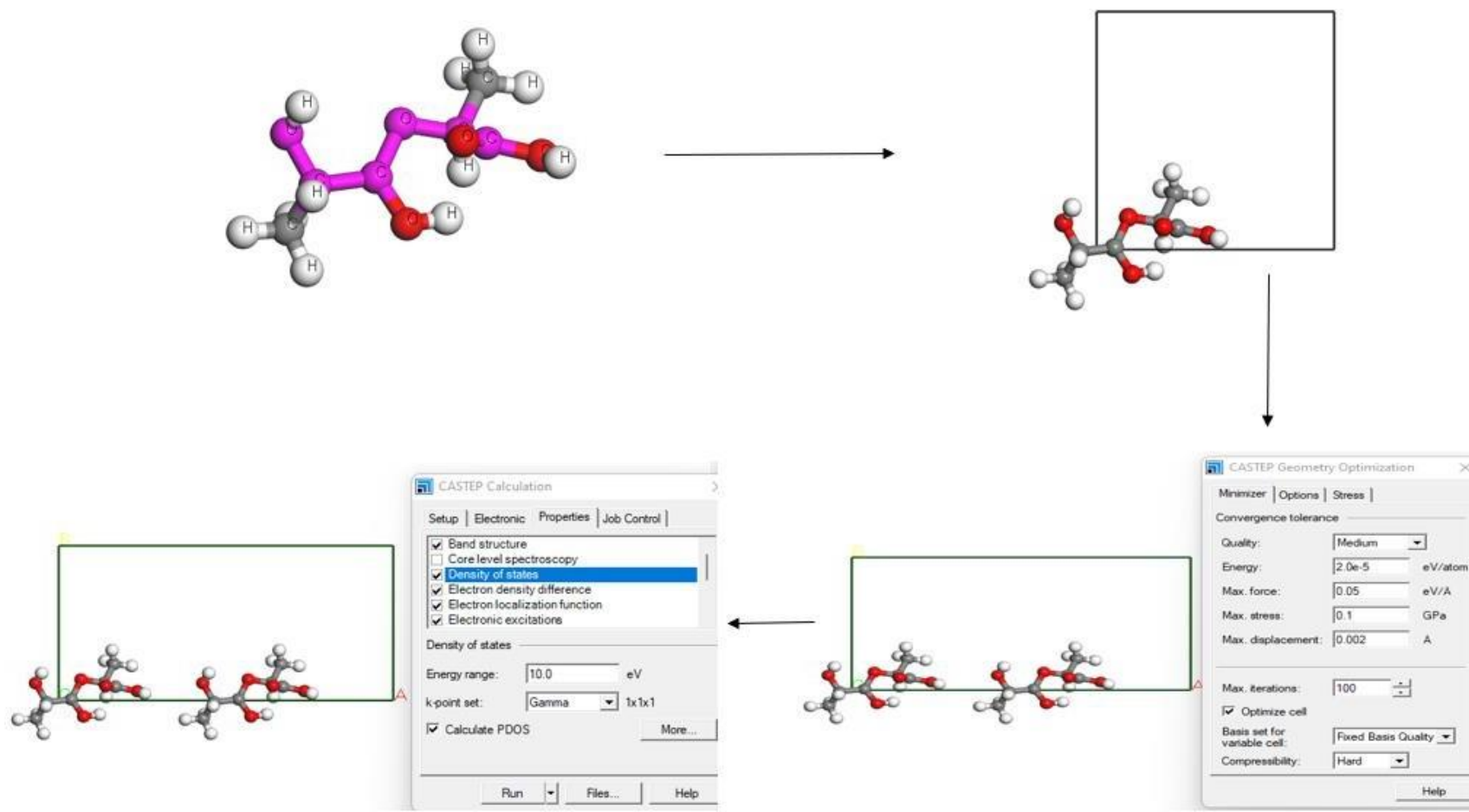


**Figure 10a:** Illustration of computational analysis of PLA

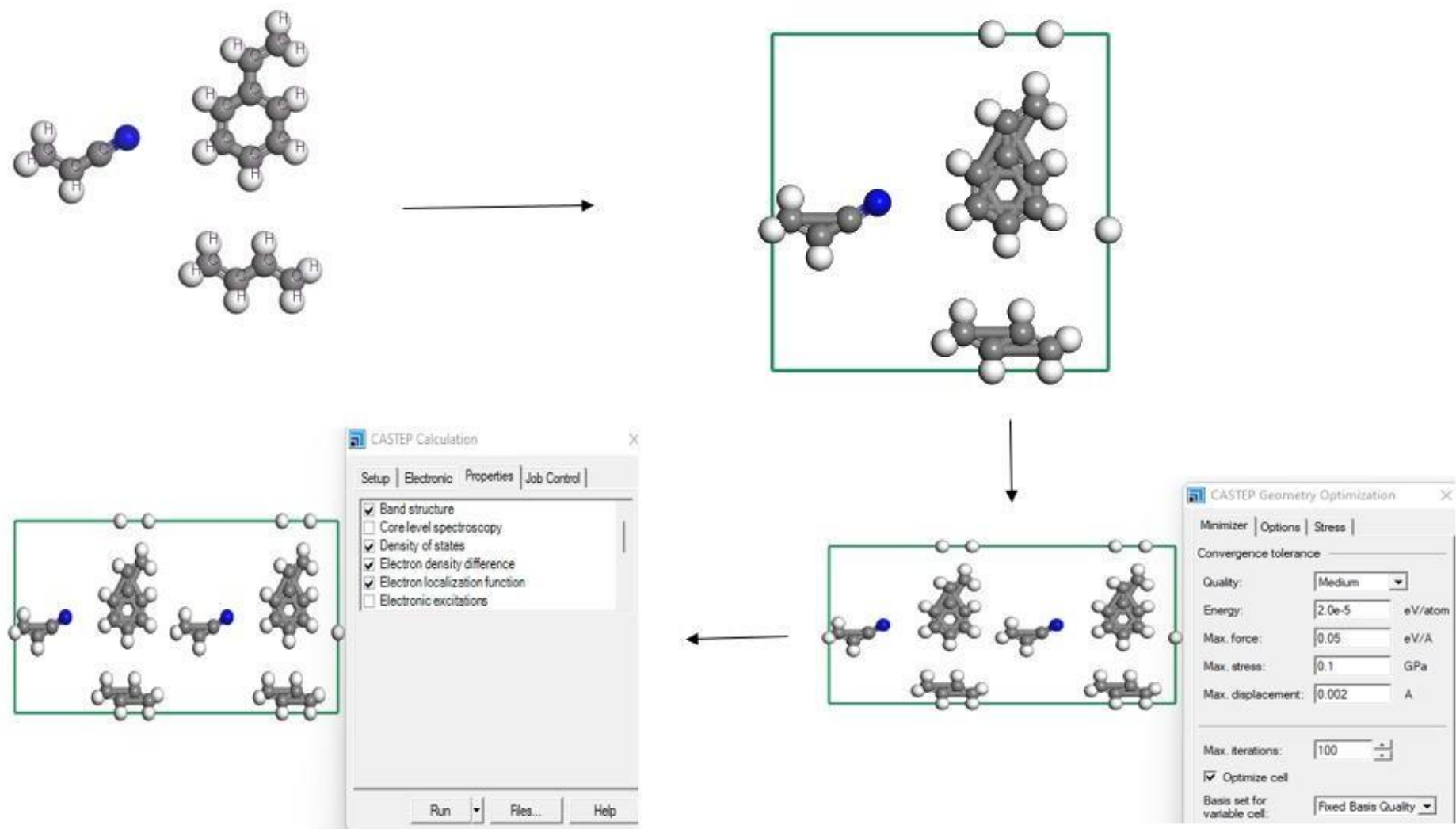


**Figure 10b:** Illustration of computational analysis of ABS

### **3.3: Fabricating bottle caps and dispenser pumps using 3-D printing guided by CAD**

#### **3.3.1: Bottle caps**

Fusion 360 software (V.2021) was used to create the computer-aided designs for the PLA bottle caps as shown in figure 11a. On the working interface, a 35 mm diameter circle was sketched. It was then extruded to 15 mm in height and shelled to 1 mm in thickness. The interior part of the cap was then threaded using ISO metric profile designation M35 x 1.5. Fillets were added to the edges of the bottle cap to obtain a smooth surface.

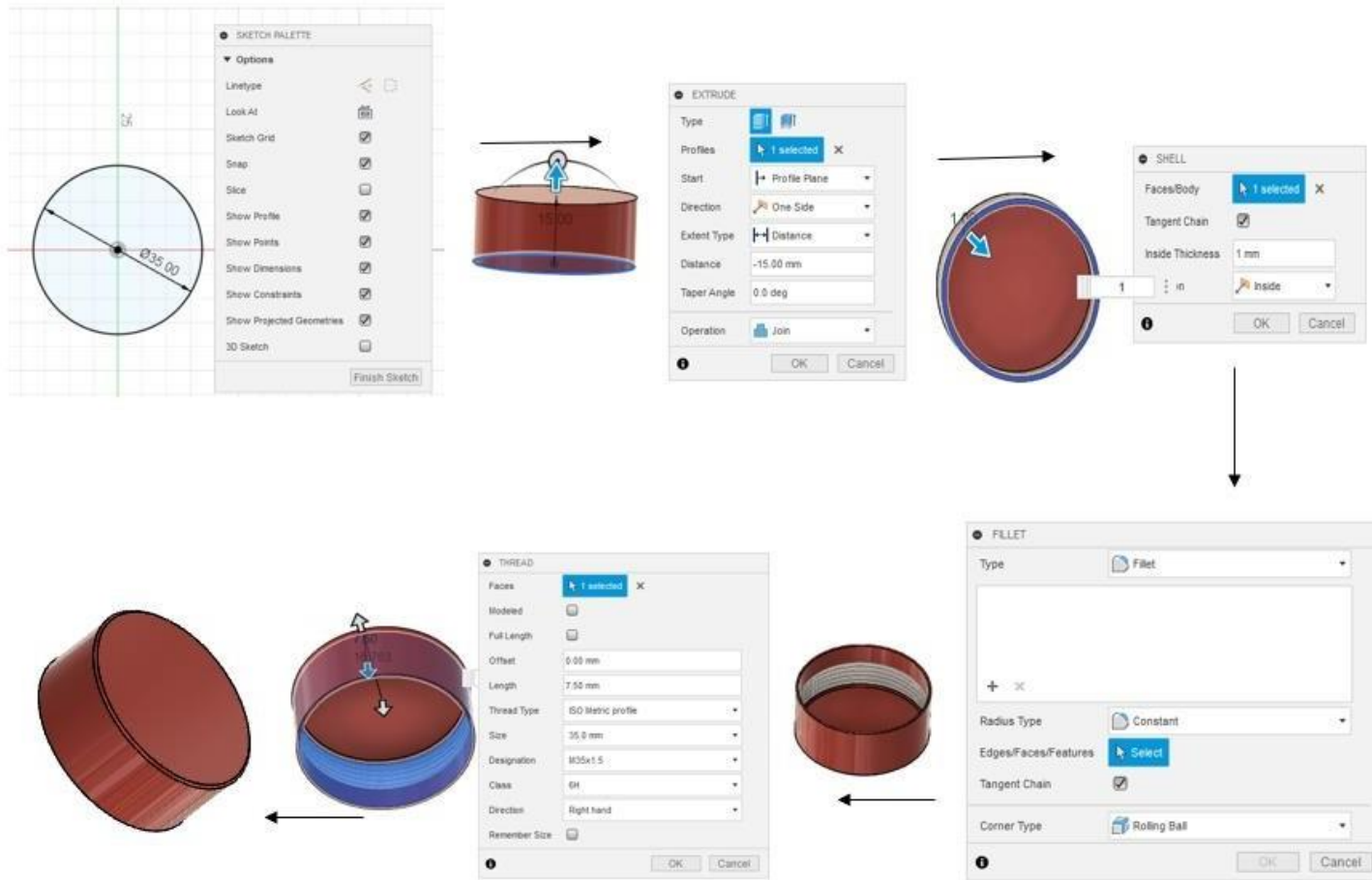
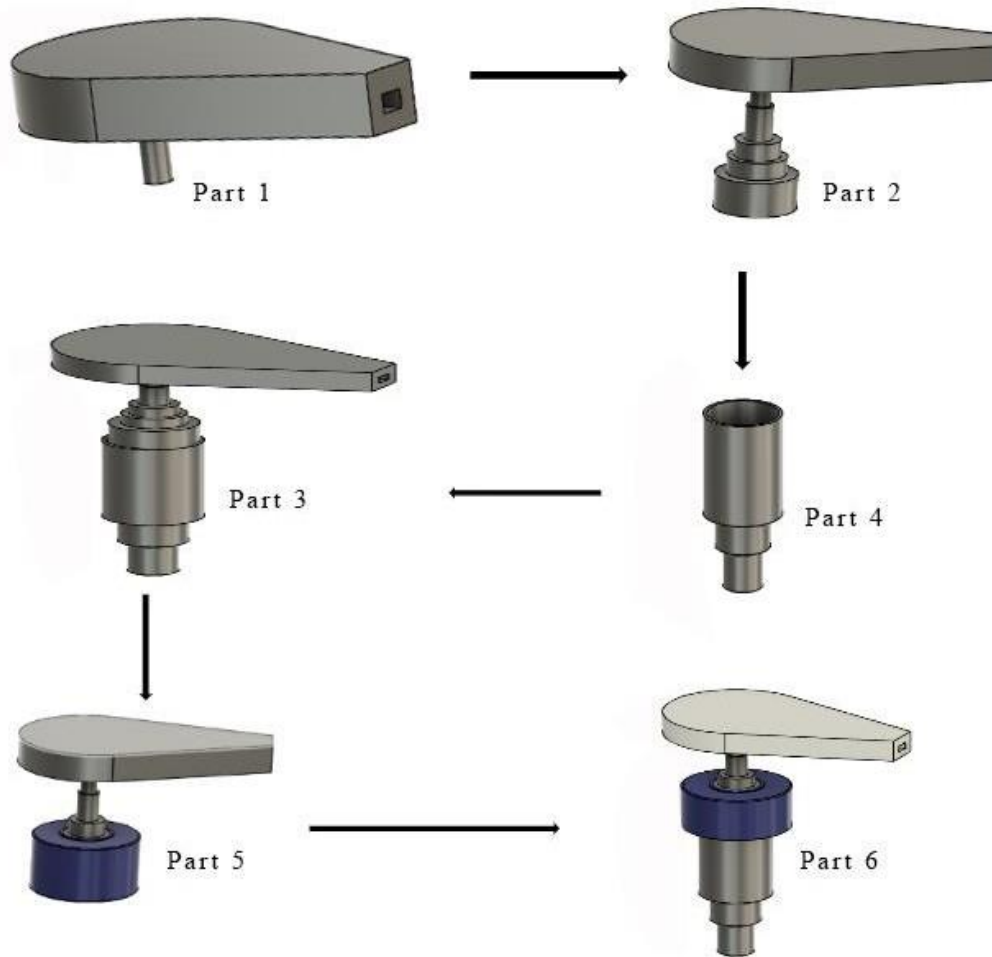


Figure 11a: Virtual bottle cap designs



### **3.3.2: Dispenser pumps**

On the working interface, a 23 mm diameter circle was drawn. It was then extruded to a height of 43 mm. Consecutive circles were extruded to a height of 13 mm and 16 mm, respectively and both joined as one body. Part two was made by sketching a 30 mm diameter and extruding to a height of 20 mm. A 15 mm hole was created at the top and a chamfer of 1 mm was added to the edges. Part three was designed from extruding cylinders of diameter 17.9 and 13 mm respectively. The outer movable bases were created by extruding, shelling, and creating a hole. The top part was created by drawing a sketch of a diameter of 35 mm which was later joined with lines of 48.82 mm at different angles. To it, a cylinder of diameter 10 mm and height 10 mm was extruded and joined to form one body. A hole of 8mm diameter was created at the bottom. A small rectangle was extruded 48 mm inwards to create an opening. The parts were then aligned to form one component as shown in figure 11b. Fillets were added to the edges of the dispenser pump to obtain a smooth surface.



**Figure 11b:** Virtual Dispenser pump design

### 3.4: 3-D printing of bottle caps and dispenser pumps

The virtual dispenser pump was created with Fusion 360 software. The model was first converted into a stereolithography extension format (STL) before being sent to the 3-D printer. Utilizing the Cura software, the models were then digitally sliced into many horizontal layers. That was followed by sending the developed virtual models to a 3-D printer-controlled computer. Using UV light, the filaments were melted before depositing them to the print bed via the extrusion route through the nozzle of the 3-D printer. The printer was controlled by a touchscreen interface that displayed status information. Table 2 summarizes the parameters utilized throughout the printing procedure.

**Table 2:**The 3-D printer parameters used for printing

Property	Parameters
Manufacturing technology	Fused deposition modeling
Diameter of the nozzle	0.4 mm
Thickness of printed layers	0.1 mm
Interior fill percentage	80%
Printing temperature	220 °C
PLA filament diameter	2.85 mm
Travel speed of the print head	60 m <sup>3</sup> /s

### **3.5: Characterization of the 3-D printed ABS and PLA specimen**

#### **3.5.1: Scanning Electron Microscopy (SEM)**

The examination of the material composition as well as the morphology of 3-D printed PLA and ABS polymers was done using a scanning electron microscope (SEM) equipped with Vega TC3 software. Scanned images were acquired by utilizing a 20kV acceleration voltage and a magnification lens. For PLA, a 2.19kx magnification was used while ABS used 969 x.

#### **3.5.2: Nuclear Magnetic Resonance**

A Spinsolve benchtop NMR spectrometer (Magritek, Germany) set at 60MHz at room temperature was used to acquire PLA and ABS 1H NMR spectra. Deuterated chloroform was used to dissolve the polymers for structural evaluation purposes. The spectra were obtained using a spectrometer at a frequency of 62.73 Hz.

#### **3.5.3: Fourier Transform Infrared Spectroscopy**

The polymer samples (PLA and ABS) were also evaluated in a Fourier Transform Infrared (FTIR) machine. The machine (SHIMADZU, USA) utilized the Attenuated Total Reflectance approach. The transmission spectra range of 600-4000 cm<sup>-1</sup> was obtained. In order to increase and maximize the surface area, the polymer samples were transformed into fine particles by crushing. An infrared monochromatic radiation was transmitted through polymer samples obtaining vibrations at different characteristic frequencies.



**Figure 12:** Fourier Transform Infrared spectrometer

#### **3.5.4: Raman Spectroscopy**

Raman microscope equipment was used in the analysis. The equipment had a 600 nm laser source. The printed samples were positioned and examined under the microscope until they were focused at the desired magnification (Otieno *et al.*, 2022). The instrument settings were later adjusted to get the required spectrum. Before analysis, the optical components and laser source were aligned. This study optimized the laser intensity, aperture, and duration of 1 second to achieve a satisfactory signal-to-noise ratio. To avoid damage to the PLA and ABS samples caused by excess heat, the laser power was kept below 50% throughout the operation

#### **3.5.5: Energy dispersive X-ray fluorescence spectroscopy**

Energy dispersive X-ray fluorescence (Rigaku, Japan) was utilized to assess the quantity the concentration of different metals in polylactic acid and acrylonitrile butadiene styrene. Additionally, secondary targets in Cartesian Geometry were used for indirect excitation to boost the sensitivity of trace element analysis by minimizing background intensity. Mo and Rx9 were chosen as supplementary targets in this investigation. About 0.5 g of finely crushed PLA and ABS samples were each placed in secondary xrf cups. They were then carefully placed on to instrument and covered using the compartment lid. They were later subjected to

radiation to detect the presence of various trace elements. Key elements of interest were calcium, tin, chromium, silicon, iron, potassium, and titanium.



**Figure 13:** Energy dispersive Xray fluorescence spectrometer

### **3.6: Determination of mechanical and antimicrobial properties of the designed bottle caps and dispenser pumps**

#### **3.6.1: Preparation of tensile sample specimen**

Thirty-three polymeric tensile test specimens were developed using fusion 360 design software. This ensured the testing met standards under type V D 638-89 ASTM standard (Otieno *et al.*, 2022). The specimens' dimensions are specified in figure 14a and table 3. The fused deposition modeling technique was then used in fabricating them.

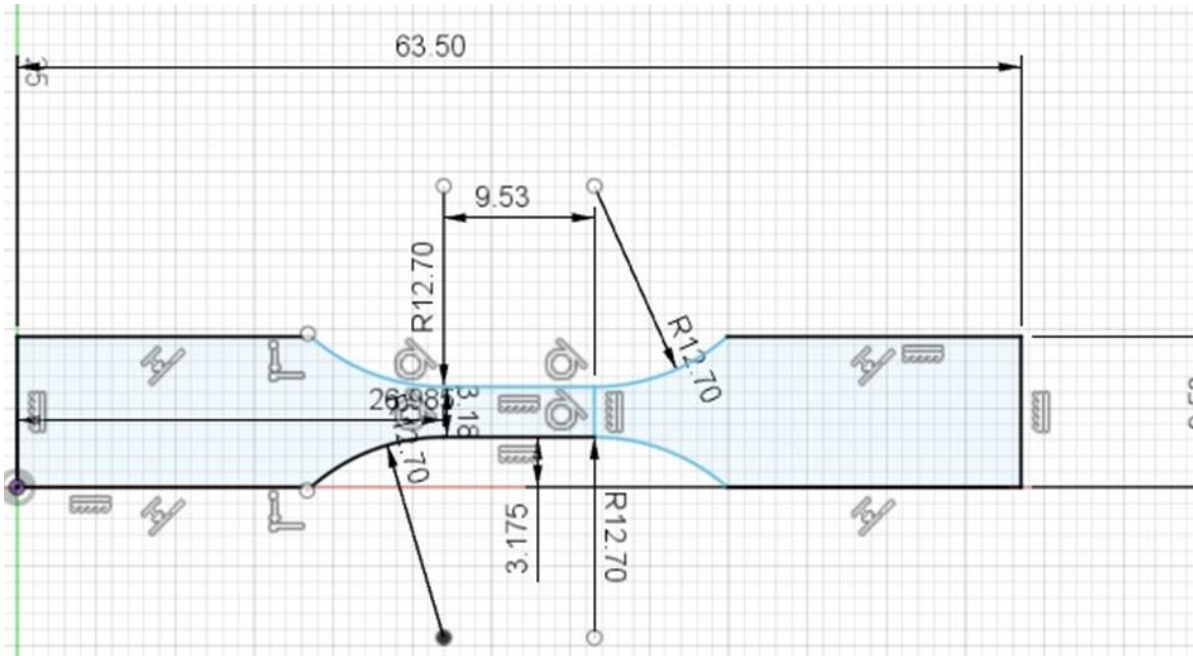


**Figure 14a:** Polymeric tensile test specimens



**Figure 14b:** Diagram of designed and printed specimen.

**Table 3:** Specimen (V D 638-89 ASTM) dimensions

Dimensions (mm)	Type V	Tolerances
Overall width	9.53	+ 0.125 (+ 3.18)
Length of the narrow section	9.53	$\pm 0.02 \pm 0.5$
Width of the narrow section	3.18	$\pm 0.02 \pm 0.5$
Gauge length	7.62	$\pm 0.010 (\pm 0.25)$
Radius of the fillet	12.7	$\pm 0.04 (\pm 1)$
Thickness	4	-
Overall length	63.5	No max

An ASTM standard test technique, D 638M was used to evaluate the tensile characteristics of plastics in the form of standard dumbbell-shaped test specimens examined under controlled conditions. Mechanical properties for ABS and PLA test specimens were evaluated using Instron testing equipment. Wallace hardness tester was used to measure hardness of the materials.



**Figure 15:** Instron and Wallace hardness tester machine

### 3.6.2: Synthesis of nanoparticles

#### 3.6.2.1: Zinc Oxide nanoparticles synthesis

The preparation of zinc oxide nanomaterials was achieved through a sol-gel technique (Klink *et al.*, 2022). A solution was made by dissolving about 8.8g of zinc acetate dihydrate ( $\text{Zn}(\text{CH}_3\text{COO})_2 \cdot 2\text{H}_2\text{O}$ ) in 100 ml distilled water. Then, 4.0g of sodium hydroxide pellets were dissolved in 100 ml of distilled water to prepare 0.1M NaOH. After mixing the two solutions, it was constantly stirred for three hours at  $60^\circ\text{C}$ . 100 ml of ethanol was then titrated dropwise to the solution containing both zinc acetate dihydrate and sodium hydroxide until the formation of a white precipitate was observed. It was left overnight to settle and later rinsed with distilled water removing residual impurities. It was then dried at  $100^\circ\text{C}$  for 4 hours. The sol was later dried to form a white powder as shown in figure 16a. The chemical reaction of the nanoparticle synthesis is expressed as shown in equation 21. It was then characterized using FTIR.

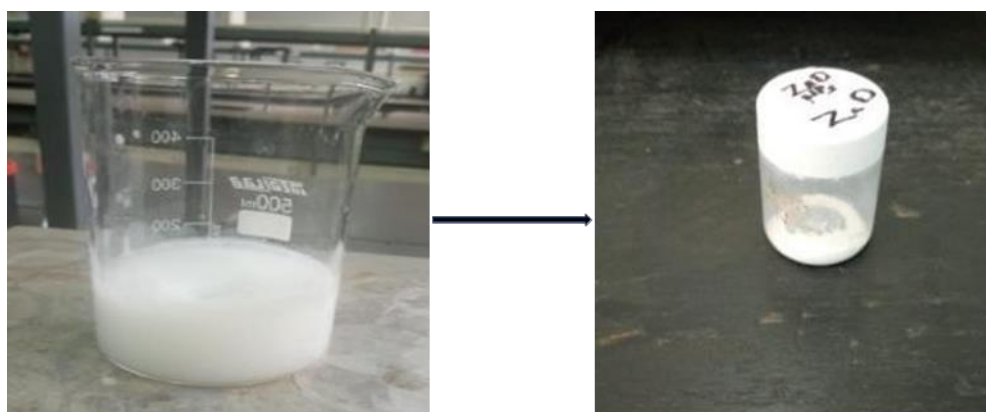
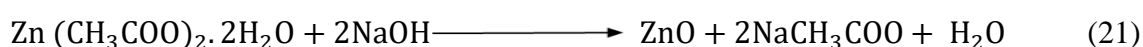


**Figure 16a:** Reaction stages of zinc oxide nanoparticle synthesis

#### 3.6.2.2: Copper oxide nanoparticles synthesis

The procedure reported by (Rangel *et al.*, 2020) was adopted; About 0.1 M copper oxide solution was obtained by dissolution of about 4 g copper sulfate in 100 ml distilled water and later stirred using a magnetic stirrer while being maintained at lower temperatures of about  $50^\circ\text{C}$ . The solution gradually changed color from blue to black. Using deionized water, the black precipitate was filtered and rinsed to eliminate the contaminants. The powder was vacuum dried for 6 hours at  $80^\circ\text{C}$ . The sample was then characterized using FTIR. The reaction stages have been expressed in figure 16b.



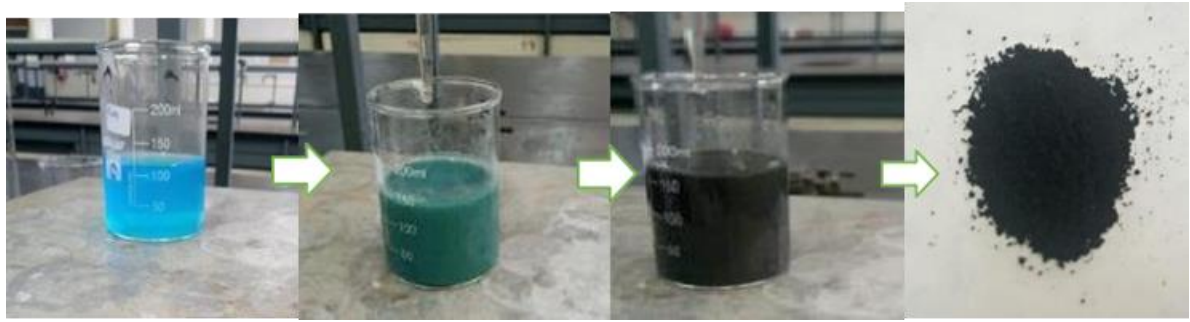


**Figure 16b:** Reaction stages of copper oxide nanoparticles

### **3.6.2.3: Antimicrobial activity of zinc oxide and copper oxide nanoparticles**

To determine the antimicrobial properties of the synthesized nanoparticles, *Bacillus thuringiensis* and *Escherichia coli* bacteria were tested using well diffusion method (Liu *et al.*, 2009). The two bacteria strains were cultured in a nutrient broth at 37<sup>0</sup>C. On solid muller hinton agar plates, 100  $\mu$ l culture broth containing 10<sup>6</sup> cfv/ml of bacteria strain was spread. The plates were left for an hour to allow for culture absorption. About 20ul of the synthesized nanoparticles solutions sample were then poured into the diffusion wells after incubation for 12 hours. The size of the zones of inhibition was later measured.

## CHAPTER 4: RESULTS AND DISCUSSIONS

### 4.1: Theoretical characterization of PLA and ABS using Material-Studio-based computational simulations.

#### 4.1.1: Geometrically optimized structural models.

The user interface of the material studio software 2021 was used to create the PLA and ABS crystal models (Figure 17). Using the symmetry calculations for both polymers, supercell units of  $4 \times 3 \times 3$  and  $3 \times 3 \times 3$  were produced for PLA and ABS, respectively. The BFGS algorithm was used to optimize the structures.

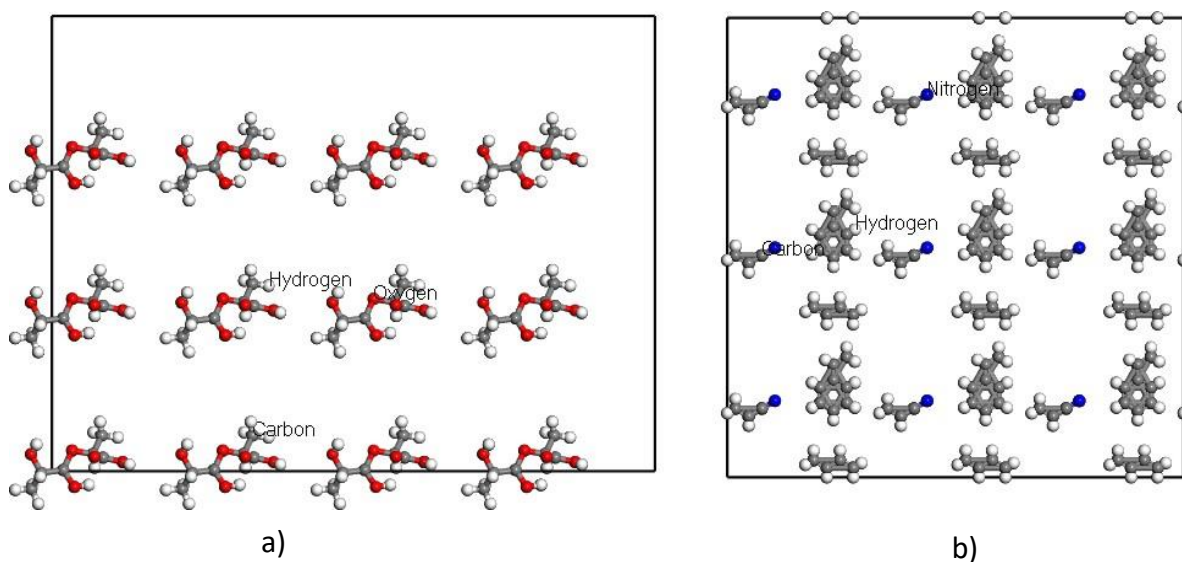


**Figure 17:** Upper view of optimized a) PLA and b) ABS structure. The white color denotes the hydrogen atom, grey shows carbon atom, the red color represents oxygen atom whereas blue represents the nitrogen atom.

**Table 4:** Lattice parameters for PLA and ABS crystals

Structure	Lattice parameters (Å)	Space group	Cell angle	Lattice type
ABS crystal	A = 10.00 B = 20.00 C = 10.00	P1	Gamma = 90.00 Beta = 90.00 Alpha = 90.00	3-D triclinic
PLA crystal	A = 20.00 B = 10.00 C = 10.00	P1	Gamma = 90.00 Beta = 90.00 Alpha = 90.00	3-D triclinic

## 4.1.2: Electronic Properties of PLA and ABS

### 4.1.2.1. Band Structure

Figure 18 shows the band gap energies for PLA and ABS calculated using the GGA-PBE functional and determined to be 1.899 and 2.539 eV, respectively. The large band gap indicated that both PLA and ABS were semiconductors.

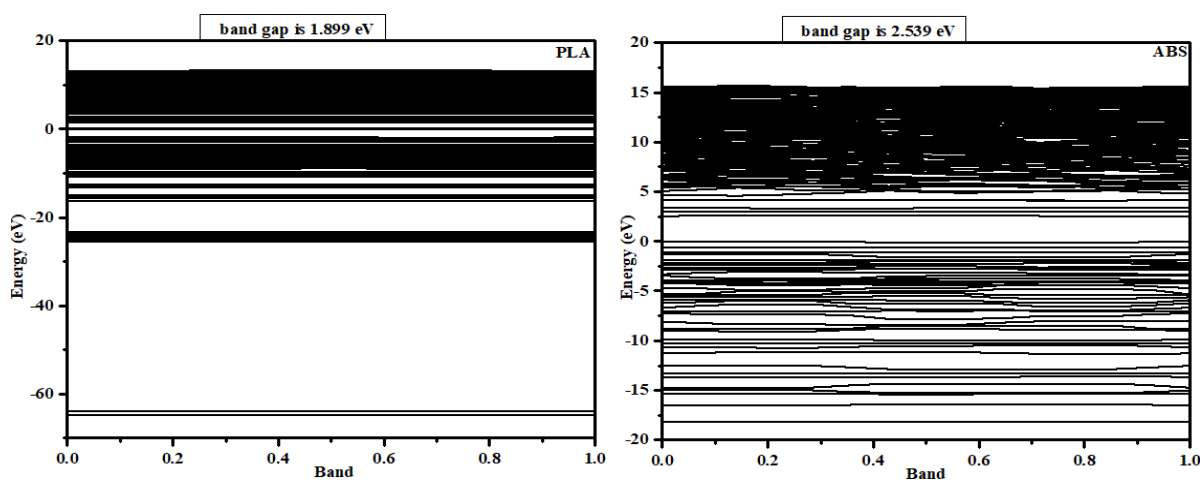


**Figure 18:** Band gap structures a) PLA b) ABS

The Mulliken population in Table 5 displays the matching findings, with smaller bond length values. This indicates stronger covalency between the corresponding PLA and ABS. A covalent bond is indicated by a high bond population value while an ionic bonding is indicated

by a low value (Otieno *et al.*, 2022). A zero population value points to an ionic connection whereas positive values show increasing covalency levels (Aouadi, 2006).

**Table 5:**PLA and ABS bond population and bond lengths

<b>Structure</b>	<b>Bond</b>	<b>population</b>	<b>Bond length</b>
<b>PLA</b>	H 18 --C11	0.85	1.21655
	C 3 -- O1	-0.15	2.62406
<b>ABS</b>	O 3 -- O5	-0.13	2.63470
	H8 – C8	1.11	1.06696
	C15--N1	1.77	1.18601

#### 4.1.2.2. Density of States

Equation 22 specifies the nature of the material and the number of accessible states at the fermi level, hence useful in determining concentration and energy distribution (Otieno *et al.*, 2022).

$$N_n(E) = \int \frac{dk}{4\pi^3} \delta(E - E_n(K)) \quad (22)$$

Whereby  $N_n(E)$  indicates the total density of states obtained by the summation of n bands while  $E_n(K)$  indicates the electron dispersion in a specific band. The general shape illustrated from the DOS histograms (figure 19) shows PLA and ABS to be semiconductors. This can equally be backed up by the broad band gap. In addition, the reduced peak numbers in the valence band as well as valleys in the conduction band signified fewer charge carriers within the materials.

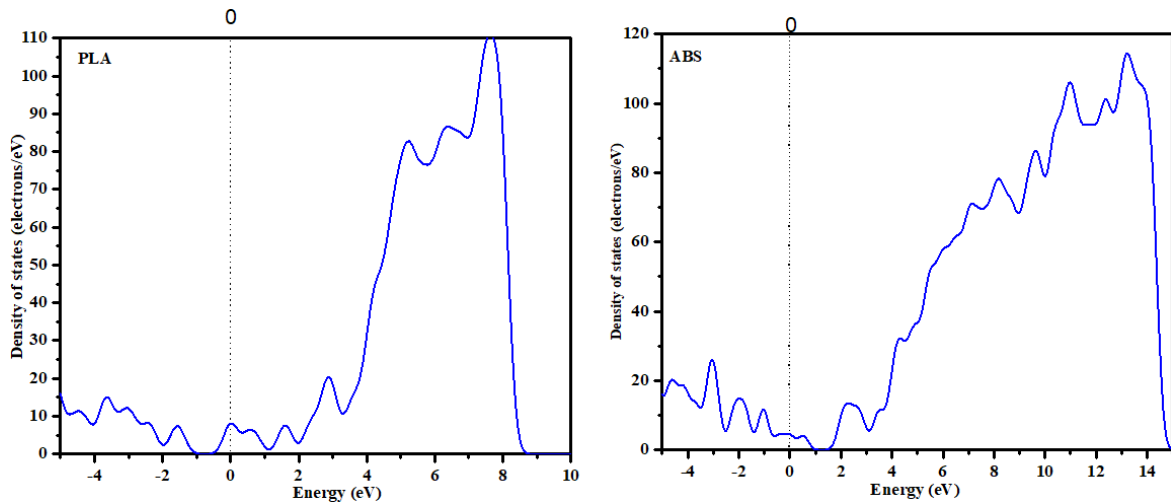


**Figure 19:** Density of states a) PLA b) ABS

#### 4.1.2.3. Projected Density of States

The nature of the orbitals forming the aforementioned structures was determined using Mulliken population analysis. PLA was composed of several atoms such as hydrogen, carbon, and oxygen. They respectively exhibited an electrical configuration of  $1S^1$ ,  $1S^2 2S^2 2P^2$ , and  $1S^2 2S^2 2P^4$ . As shown in figure 20, the valence and conduction bands were dominated by the 2P carbon orbital, whereas the 2P and 2S oxygen orbitals occupied the valence and conduction bands for PLA. Atoms such as nitrogen, carbon, and hydrogen constituted ABS with electronic configurations of  $1S^2 2S^2 2P^3$ ,  $1S^2 2S^2 2P^2$ , and  $1S^1$ , respectively (Otieno *et al.*, 2022). Both bands were dominated by nitrogen and carbon 2P orbitals. After losing an electron, the conduction band was dominated by the hydrogen 1S orbital, whereas the remaining filled  $2S^2$  orbital was observed in the valence band, resulting in  $SP^2$  hybridization.

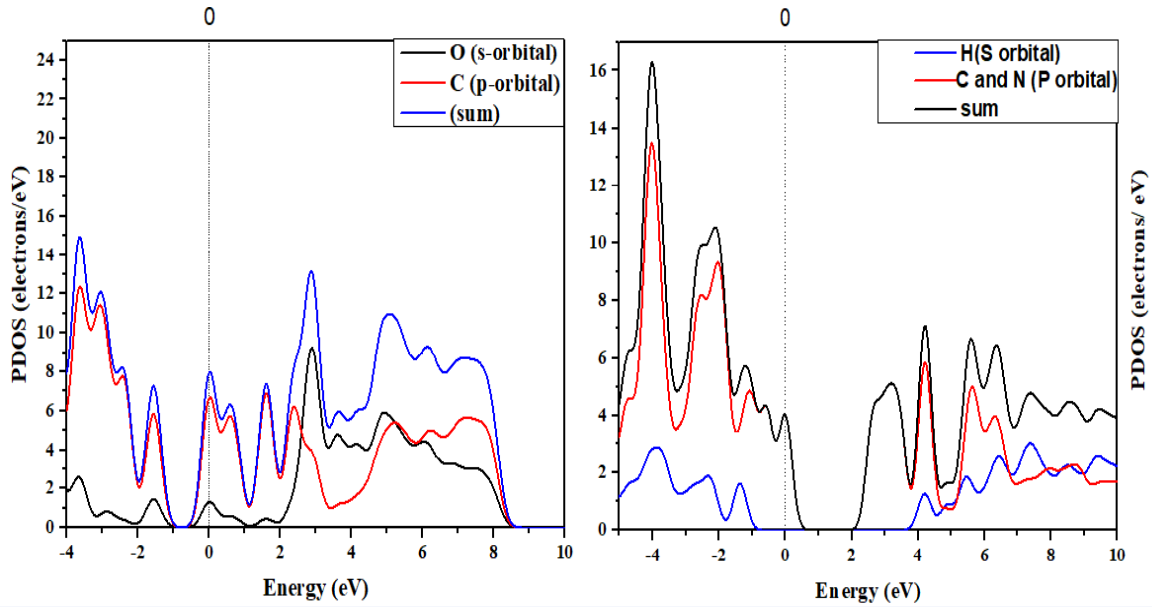


**Figure 20:** Partial density crystal of states for PLA (left image) and ABS (right image)

#### 4.1.2.4. Electron Density

The probability of an electron being at a particular point is defined as electron density. This can be determined from the Born-Oppenheimer approximation and Schrodinger formalism. For instance, the probability of one electron density can be obtained from (equation 23) (Ayers *et al.*, 2007).

$$\rho_1(r_1) = N \int \varphi_{el}^* (r_1, r_2, \dots, r_N; \{R\}) \cdot \varphi_{el} (r_1, r_2, \dots, r_N; \{R\}) dr_2 \dots dr_N \quad (23)$$

Where  $\rho_1$  indicates the density of a given atom, fixed nuclear coordinates are represented by  $R$ ,  $\varphi_{el}$  denotes the stationary wave function,  $r$  signifies electron position, whereas  $N$  denotes the number of electrons. When PLA constituents (carbon, oxygen, and hydrogen) interact, the electron cloud surrounding each atom combines to form a single entity (Chami Khazraji & Robert, 2013). Denoted by regions of electron enrichment and depletion near the bonds and atoms, polylactic acid polymer signified electron enrichment near the carbon, oxygen, and hydrogen atoms shown by blue shade while the depletion shown by the yellow color was not quite prominent. The electron interaction of ABS constituents showed electron enrichment signified by the presence of the blue shade near the carbon, hydrogen, and nitrogen atoms and bonds as observed in figure 21.

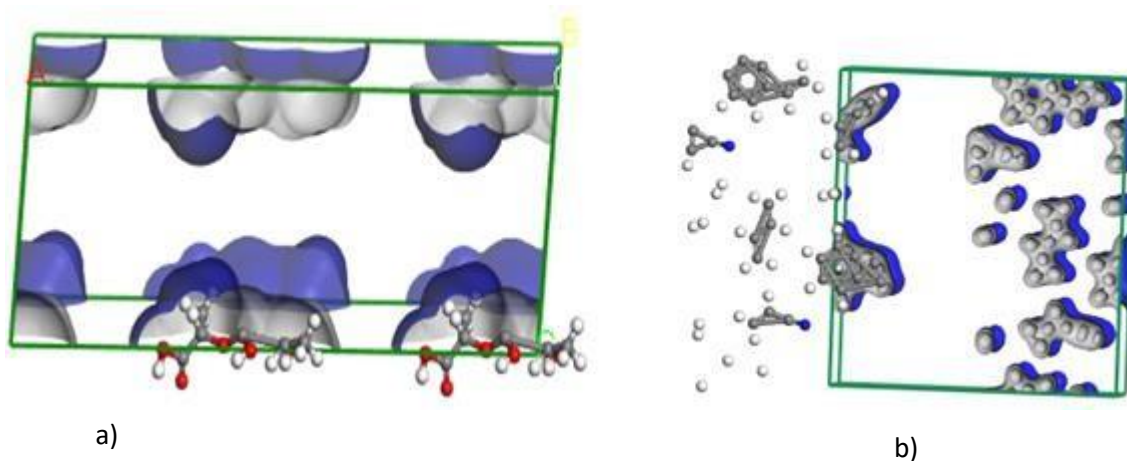


**Figure 21:** Electron density a) PLA b) ABS respectively

#### 4.2: Work function

As illustrated in figure 22, the work function values for PLA and ABS were calculated as 3.364 and 4.503 eV, respectively. Work function can therefore be defined as the minimum energy required to remove an electron from the solid to a point immediately outside the surface without any velocity. Alternatively, it can be defined as the energy required to remove an electron from the fermi level into a vacuum (Caglar *et al.*, 2018; Ghosh & Chakrabarty, 2011; Otieno *et al.*, 2022). According to Haynes (2014), the respective work function values for metals such as Al, Ag, Pd, Pt, and Au include 4.05, 4.43, 5.30, 5.70, and 5.21 eV. These values are within the 5% experimentally measured data (4.26, 4.74, 5.60, 5.94, and 5.31) eV implying that the DFT calculation method can be satisfactorily used to calculate work function values (Haynes, 2014). Lower work function values, as reported in the current study, demonstrated poor conductivity, therefore, making them suitable for use in packaging. PLA provides comparable better insulation due to its lower work function value. The work function ( $\phi$ ) of a given material can be reduced by either lowering the vacuum level or raising the Fermi level. These lower work function energy values can be attributed to fewer carrier electrons, implying poor thermal conductivity (Otieno *et al.*, 2022). This compliments Hartree-Fock's theory which accounts for electron-electron interaction leading to exchange energy or binding energy because of electron interaction (Sherrill, 2000).

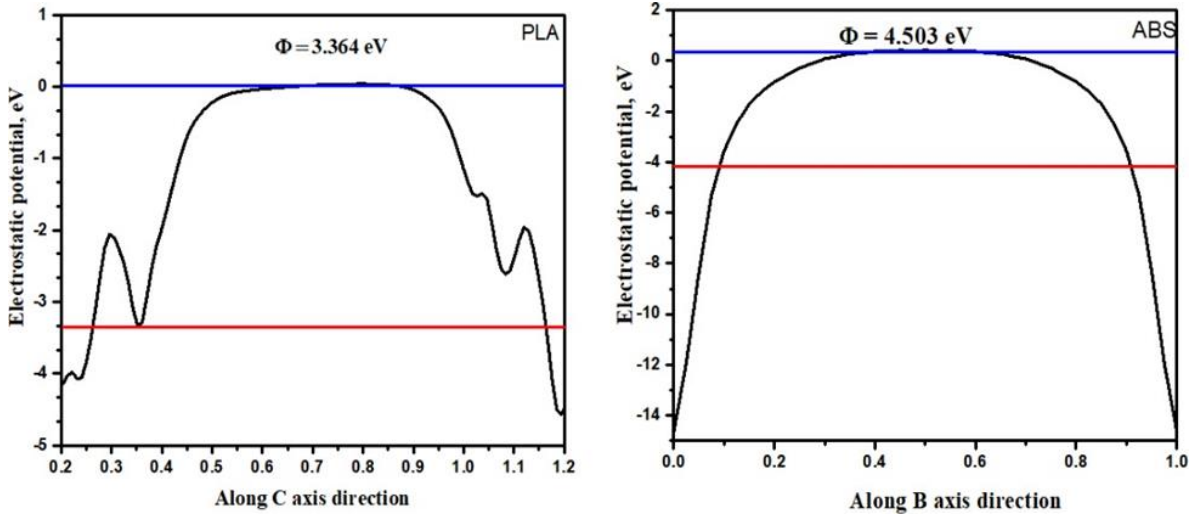


**Figure 22:** computed work function ( $\phi$ ) values of PLA and ABS. The blue solid line represents the fermi level whereas the red line indicates the vacuum level.

### 4.3: Optical properties

#### 4.3.1: Conductivity.

Figure 23 shows the optical conductivity of the PLA polymer. Within the photon energy range of 24 – 40 eV, the optical conductivity was found to be zero. For the PLA polymer, the maximum peak optical conductivity was identified at a frequency energy of 12 eV. This lower value is consistent with the lower work function values initially obtained thus accounting for the improved insulative properties. The maximum conductivity peak was observed at 0.648 at a frequency energy of 12.4 eV. Similarly, the minimum conductivity was recorded at 3.71 eV and 6.56 eV. These conductivity values point to ABS being a partial semiconductor.

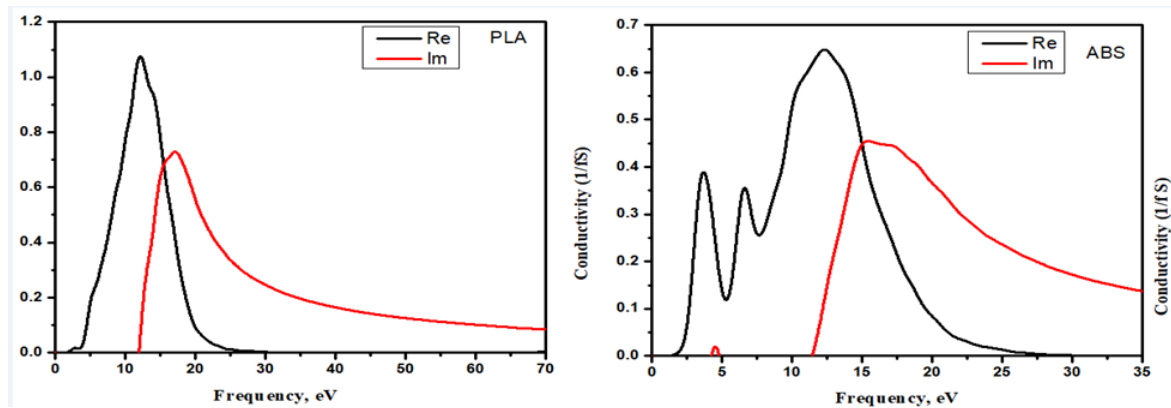


**Figure 23:** PLA and ABS Conductivity



### 4.3.2: PLA and ABS absorption coefficients

For the ABS polymer, a higher absorption coefficient was recorded at  $4.43 \times 10^4 \text{ cm}^{-1}$ . That was followed by a sudden drop observed at a frequency range of 12.9 - 26 eV. The significant rise in absorption coefficient recorded at the frequency range of 0 - 12 eV is consistent with the values of a conductive ABS filament. For the PLA polymer, the maximum absorption coefficient peak was recorded at  $7.0 \times 10^4 \text{ cm}^{-1}$  as depicted in figure 24. The absorption coefficient was later reduced to zero between frequency energy values in the range of 25 - 80 eV. These values affirm PLA polymer as being colorless and transparent hence suitable for use in the packaging industry. It's noteworthy to mention that within the UV visible region, the strongest absorption zone for the PLA polymer falls inside the frequency energy range of 4 - 22 eV. The higher absorbance could be a result of poor light scattering due to printing geometry and material composition.

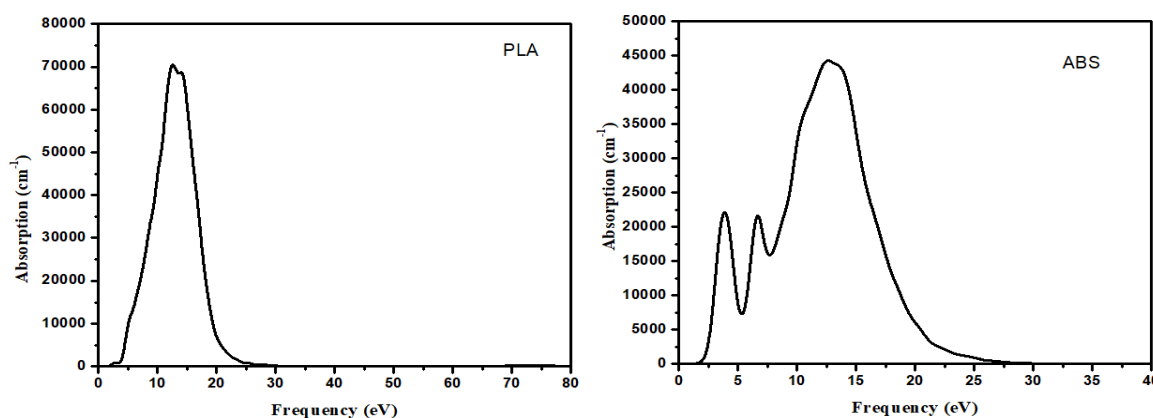


**Figure 24:** Absorption coefficients of PLA and ABS

### 4.4: Adsorption of CuO and ZnO nanoparticles on PLA and ABS surfaces

Modification of frequently touched PLA and ABS surfaces with copper oxide and zinc oxide nanomaterials makes them less susceptible to bacterial infections. This is because they can effectively kill microbe colonies and prevent bacterial colonization (Knetsch & Koole, 2011). Various factors such as chemical and topological characteristics influence the rate of microorganism adhesion on numerous polymer surfaces. For instance, a rougher PLA and ABS surface would provide more surface area for microbe adhesion than a smoother surface. In reference to chemical characteristics, hydrophobic surfaces are more prone to microorganisms than hydrophilic surfaces (Almaguer-Flores *et al.*, 2010; Busscher *et al.*, 1986; Katsikogianni *et al.*, 2006; Knetsch & Koole, 2011; Pavithra & Doble, 2008). Numerous researches have been

undertaken on the chemical process of antimicrobial activity of CuO and ZnO, which rely on their size and shape (Pal *et al.*, 2007; Panáček *et al.*, 2006; Sotiriou & Pratsinis, 2010). The nanoparticles are reported to cause an antimicrobial effect by binding and migrating into the cell of the bacteria hence disrupting the genetic material and also damaging the cytoplasmic membrane (AshaRani *et al.*, 2009; Glehr *et al.*, 2013; Knetsch & Koole, 2011). Adsorption of ZnO and CuO nanocrystals on PLA and ABS can be simulated as shown in figure 25. This would aid in the determination of the binding, adsorption energy, and prediction of the adsorption isotherm associated with this process. The cleaved surface generated vacant sites to which the ZnO and CuO nanoparticles would be later adsorbed.

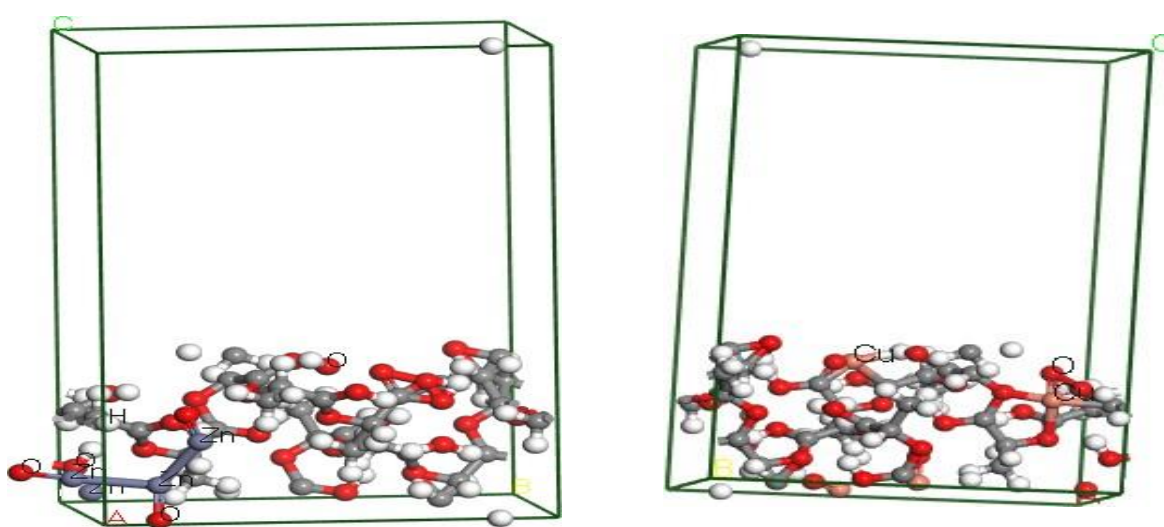


**Figure 25a:** Adsorption of ZnO and CuO nanoparticles respectively on the polylactic acid surface.

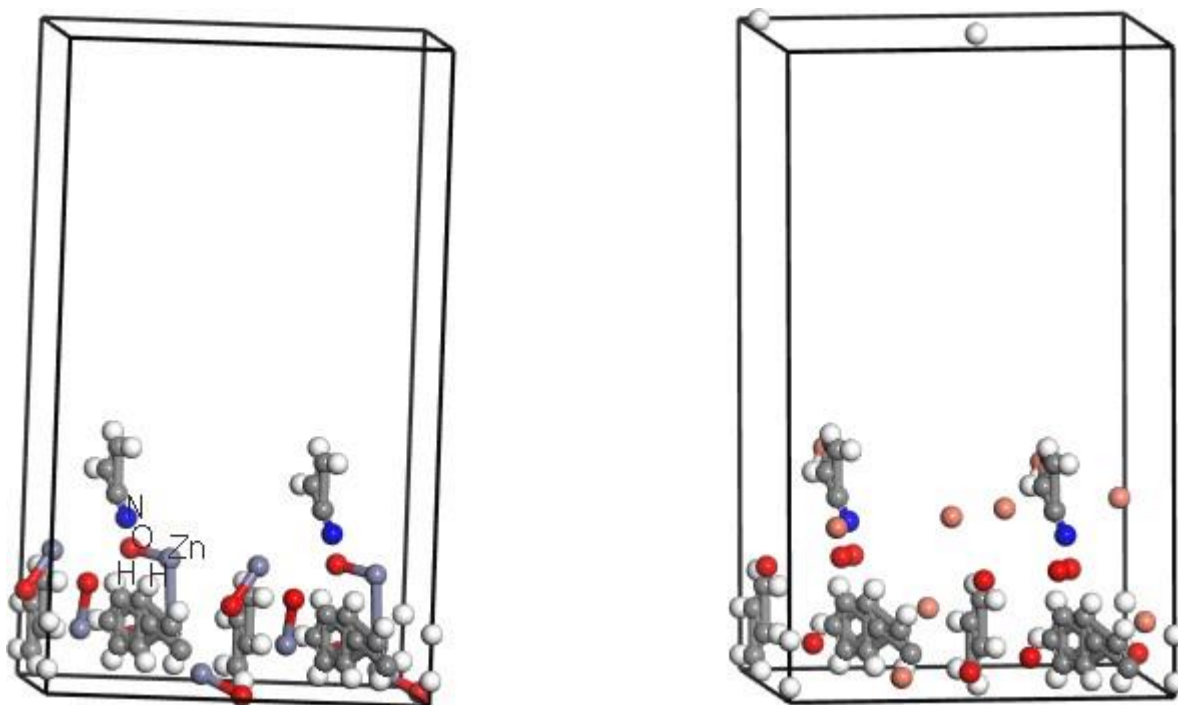


**Figure 25b:** Adsorption of ZnO and CuO nanoparticles respectively on acrylonitrile butadiene styrene surface

Incorporation of ZnO and CuO nanoparticles into the polylactic acid resulted in a final adsorption energy of -92.4486 and -654.8616 kcal/mol as expressed in table 6a while the adsorption energy of -35.4369 and -5.9236 kcal/mol was obtained for the interactions between ABS-ZnO and ABS- CuO as shown in table 6b. The antibonding and bonding state is created by the assumption of being tightly localized, the adsorbate-induced level is modelled as a single layer after the interaction of carbon and oxygen 2P orbital with the zinc and copper 3d state. The presence of an empty antibonding state which is caused by the shift of the 3d orbital above the fermi level results in a net force of attraction between the nanoparticles and polylactic acid. Having fulfilled various characteristics of chemisorption including defined as a monolayer process, an irreversible reaction due to the involvement of chemical bonding between the molecules. The adsorption energy was calculated by adding the deformation and rigid adsorption energies. It defines the energy released when unrelaxed base polymers and nanoparticle constituents are adsorbed on the PLA and ABS surfaces (1,1,0). Deformation energy, on the other hand, is the energy released when the adsorbed ZnO and CuO NPS are relaxed on the PLA and ABS surfaces (1,1,0) (Abdalla *et al.*, 2018). Both deformation and adsorption energies are in kcal/mol.

**Table 6a:** Adsorption energy of PLA-ZnO and PLA-CuO interactions.

No of configurations	Structure	Total Energy	Adsorption energy	Rigid adsorption energy	Deformation Energy	ZnO and CuO; dE <sub>ad</sub> /dNi
1	PLAZnO	-1.6285	-92.8022	-1.6285	-91.1737	-92.8022
2	PLAZnO	-1.6115	-92.7853	-1.6116	-91.1737	-92.7853
3	PLAZnO	-1.5571	-92.7309	-1.5571	-91.1737	-92.7309
4	PLAZnO	-1.3853	-92.5591	-1.3853	-91.1737	-92.5591
5	PLAZnO	-1.2748	-92.4486	-1.2748	-91.1737	-92.4486
6	PLACuO	-7.1914	-656.511	-7.1915	-649.3197	-130.231
7	PLACuO	-6.7210	-656.041	-6.7211	-649.3196	-130.675
8	PLACuO	-6.1698	655.4895	-6.1698	-649.3196	-130.511
9	PLACuO	-5.8213	-655.141	-5.8213	-649.3196	-130.708
10	PLACuO	-5.5419	-654.862	-5.5419	-649.3197	-130.608

**Table 6b:** Adsorption energy of ABS-ZnO and ABS-CuO interactions.

No of configurations	Structure	Total Energy	Adsorption energy	Rigid adsorption energy	Deformation Energy	ZnO and CuO; dE <sub>ad</sub> /dNi
1	ABS-ZnO	-11.2541	-36.0451	-11.2543	-24.7907	-7.2261
2	ABS-ZnO	-11.0079	-35.7990	-11.0082	-24.7907	-7.1146
3	ABS-ZnO	-10.8496	-35.6406	-10.8496	-24.7910	-6.7226
4	ABS-ZnO	-10.7735	-35.5646	-10.7738	-24.7907	-6.9567
5	ABS-ZnO	-10.6460	-35.4369	-10.6463	-24.7906	-6.7879
6	ABS-CuO	-6.1296	-6.0459	-6.0652	0.0192	-1.1742
7	ABS-CuO	-6.1167	-6.0330	-6.0736	0.0406	-1.1658
8	ABS-CuO	-6.0393	-5.9557	-5.9893	0.0336	-1.1652
9	ABS-CuO	-6.0282	-5.9446	-5.9759	0.0313	-1.1850
10	ABS-CuO	-6.0072	-5.9236	-6.0028	0.0793	-1.0593

#### 4.4.1: Geometrically optimized structural models.

The theoretical results showed that the adsorption of copper oxide and zinc oxide nanocrystals on both PLA and ABS polymer surfaces cleaved at 1,1,0 followed the Langmuir equation for adsorption (equation 24) since it describes monolayer adsorption. In addition, it also gives clarity on surface homogeneity, distribution of binding sites, and the energies required to facilitate the bonding of the adsorbate on the adsorbent surface (Ayawei *et al.*, 2015, 2017).

$$\frac{C_e}{q_e} = \frac{1}{KLq_m} + C_e/q_m \quad (24)$$

Where  $C_e$  and  $q_e$  are the amount of unadsorbed adsorbate concentration and adsorbed adsorbate in solution at equilibrium respectively,  $KL$  is the Langmuir constant and  $q_m$  is the maximum adsorption capacity (Piccin *et al.*, 2011).

### 4.5: Miscibility of PLA-ZnO, PLA-CuO, ABS-ZnO and ABS-CuO nanoparticles

#### 4.5.1: Phase diagrams

Phase diagrams aid in determining the stability and compatibility of various binary mixtures.

It is obtained from the derivatives of free energy  $\Delta G_{mix}$  (equation 25) (Fan *et al.*, 1992).

$$\frac{\Delta G_{mix}}{RT} = \frac{\phi_a}{n_a} \ln \phi_a + \frac{\phi_b}{n_b} \ln \phi_b + x\phi_a\phi_b \quad (25)$$

The spinodal and binodal curves are simulated from the second and first-order derivatives of the free energy (Simmons, 2022). A critical point is the intersection point of the two curves. Not all mixtures have critical points according to the Flory-Huggins model, this could result in the miscibility of the components at any given temperature (Campos *et al.*, 1996). The region outside the binodal curve is stable hence a miscible binary mixture while the region between the spinodal (green line) and binodal (blue line) curve is known to be metastable implying that the concentration variation of any phase may result in separation within the blend (Abdalla *et al.*, 2018). The instability of the region within the spinodal curve causes spontaneous phase separation of the binary mixtures. In addition, increasing the polymerization degree decreases the rate of miscibility. The critical temperatures for PLA-ZnO and PLA-CuO blends are 495 and 3250 K, respectively as observed in figure 26a. The region within the spinodal curve for the PLA-ZnO and PLA-CuO blends equally supports immiscibility.

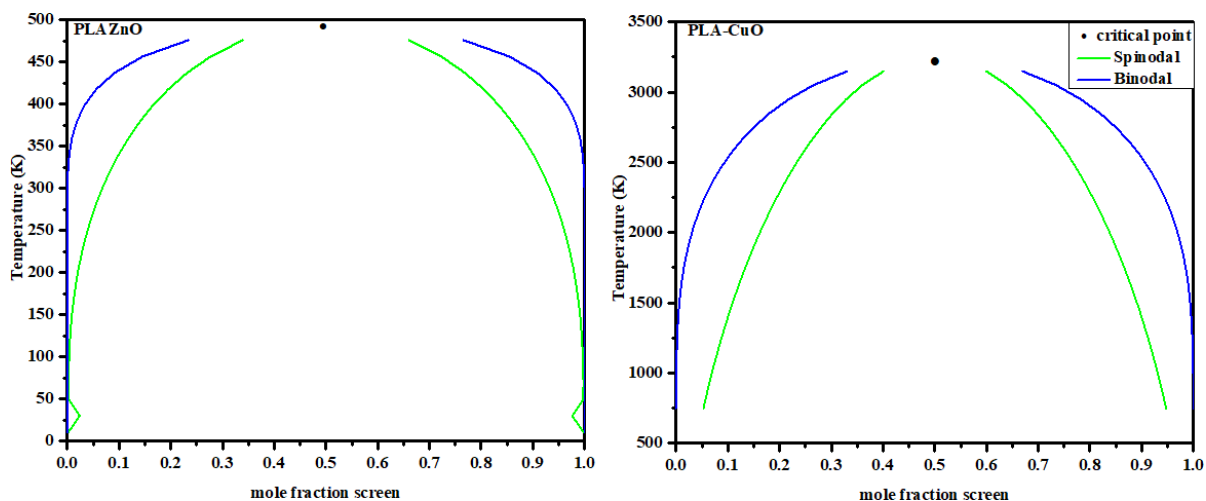


**Figure 26a:** Phase diagrams of PLA-ZnO and PLA-CuO blends. The blue solid line denotes the Binodal curve, the black dot represents the critical point and the green line indicates the spinodal curve.

The critical temperatures for ABS-ZnO and ABS-CuO blends are 2080 and 3890 K respectively as displayed in figure 26b. The spinodal curve region for the ABS-ZnO and ABS-CuO blends equally supports immiscibility.

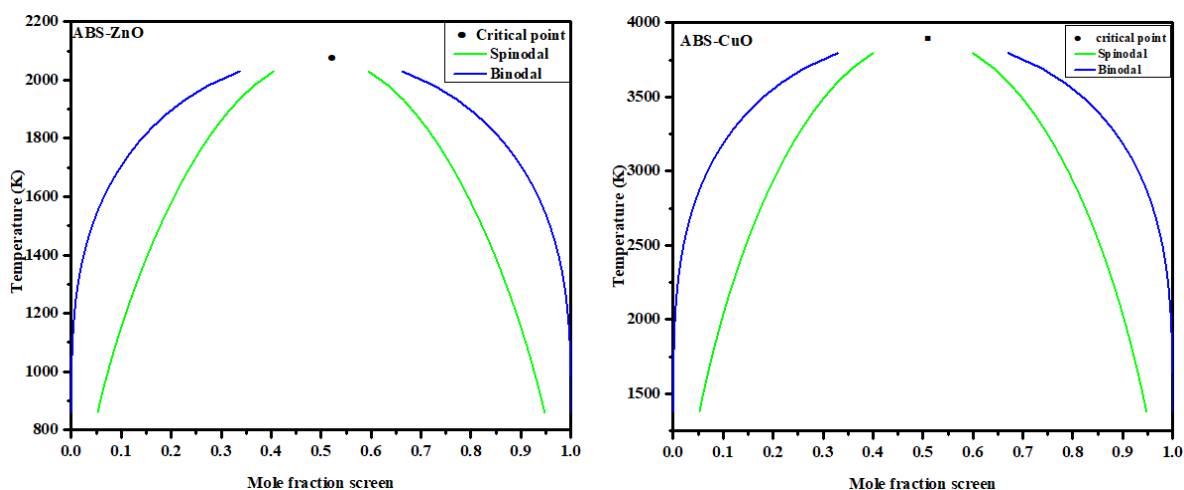


**Figure 26b:** Phase diagrams of ABS-ZnO and ABS-CuO blends

#### 4.5.2: Flory-Huggin's interaction parameters and mixing energies

The interaction chi parameter as well as mixing energies are important factors in determining the compatibility of a binary system. The two components would prefer to mix if the chi parameter is negative. In contrast, a positive value indicates the two components are

immiscible. Similarly, positive mixing energies would be attributed to immiscibility while negative mixing energy would be ascribed to the two components tending to mix under an exothermic process (Ryjkina *et al.*, 2002; Yang *et al.*, 2004). The immiscibility of PLA-ZnO and PLA-CuO was supported by the positive chi parameter (0.3238,20.632) and the Emix (0.1918,12.221) values respectively within a temperature range of 298 K. The immiscibility of ABS-ZnO and ABS-CuO was equally supported by the positive chi parameter (55.6398, 96.0693) and the Emix (32.9492, 56.8911) values, respectively within a temperature range of 298 K.

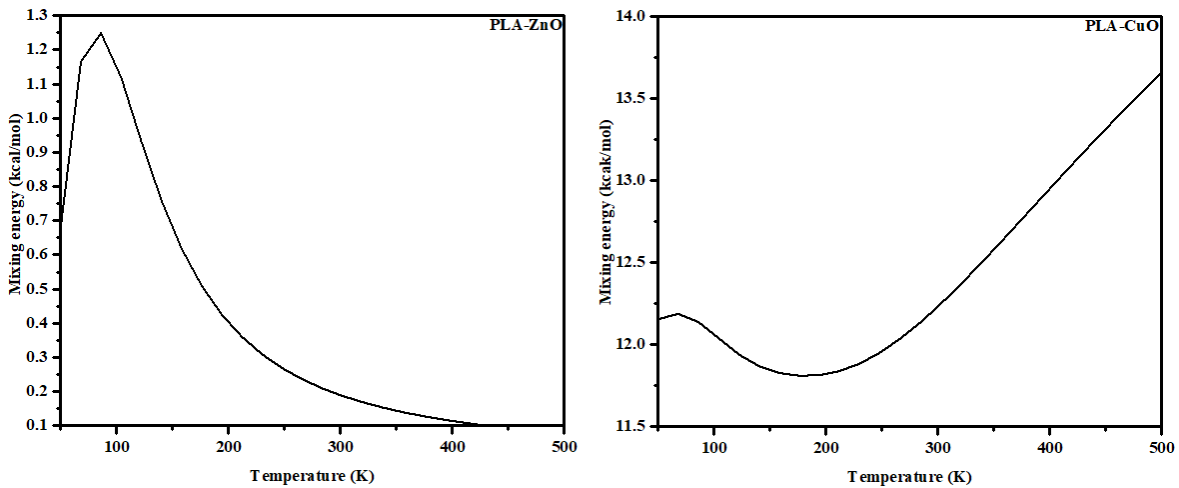


**Figure 27a:** Mixing energies for PLA-ZnO and PLA-CuO blends against temperature

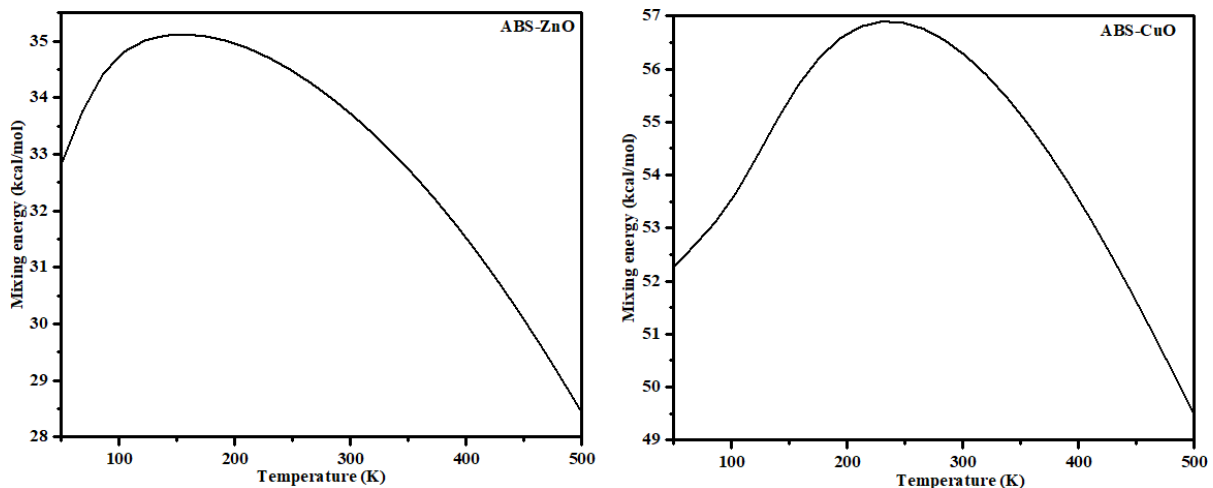


**Figure 27b:** Mixing energies for ABS-ZnO and ABS-CuO blends against temperature

### 4.5.3: Free energies

Each binary mixture's free energies at varying volume fractions and temperatures were computed via equation 24. The blend is expected to be miscible if  $\Delta G_{mix} < 0$  and only a single minimum point exists on the curve while immiscible if  $\Delta G_{mix} > 0$  (Abdalla *et al.*, 2018). The binary systems were computed at different temperatures and the polymerization degree of polylactic acid was set to 10000. As observed in figure 28a, the free energies for PLA/CuO NPs were positive at all temperatures hence revealing miscibility for the binary system. At a temperature of 500K, the free energies are negative therefore PLA-ZnO blend is slightly miscible and regarded immiscible at temperatures 50,162.5,275 and 387.5K since all the free energies were positive.

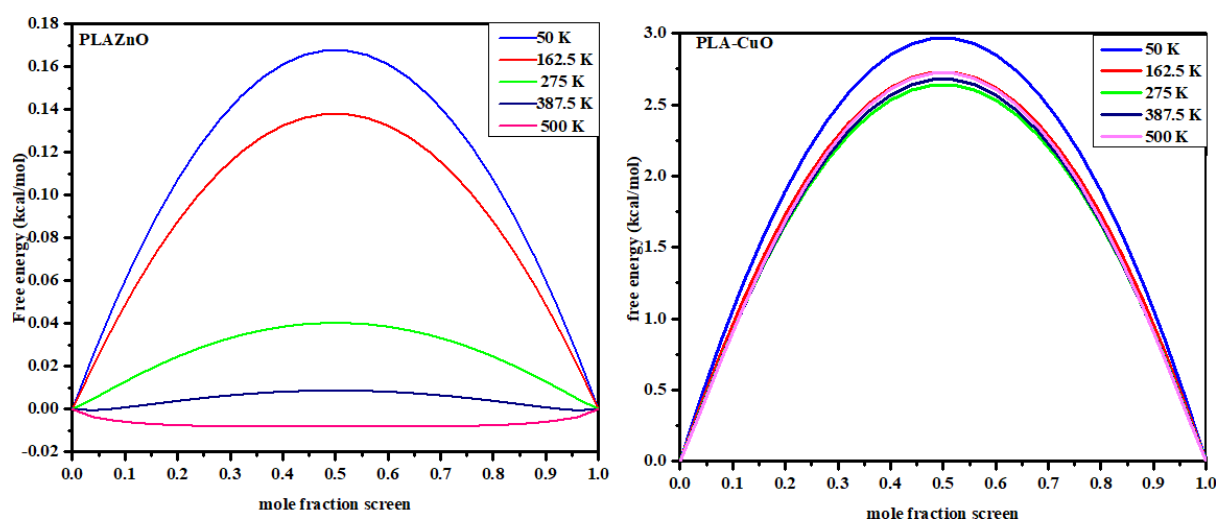


**Figure 28a:** Free energies of PLA-ZnO and PLA-CuO blend against mole fractions

The free energies for ABS-ZnO and ABS-CuO were positive at all temperatures hence revealing miscibility for the binary system at temperatures 50,162.5, 275 and 387.5 K. It is worth mentioning that the immiscibility of the blends increased with an increase in mole fraction.



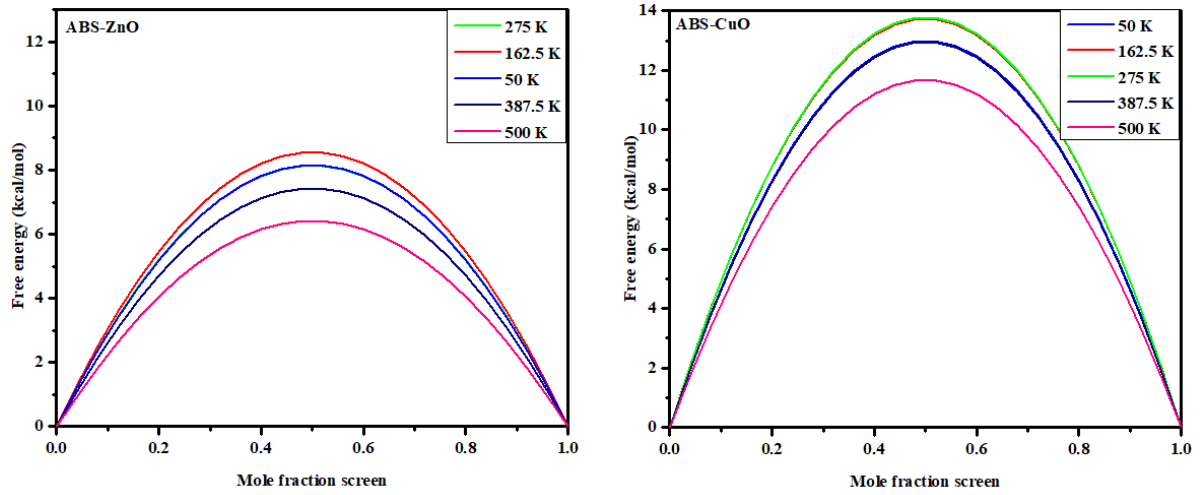


**Figure 28b:** Free energies of ABS-ZnO and ABS-CuO blend against mole fractions

#### 4.6: Fabricating bottle caps and dispenser pump

##### 4.6.1: Bottle caps.

The bottle cap designs were then converted to the appropriate file extension formats including STL (stereolithography). Using the Cura software, the three-dimensional virtual model was then digitally divided into numerous horizontal layers. After calculating the extrusion path, molten PLA and ABS filaments with an infill density of 80% were deposited on the print bed through the 3-D printer (Ultimaker<sup>2</sup>, USA) nozzle.

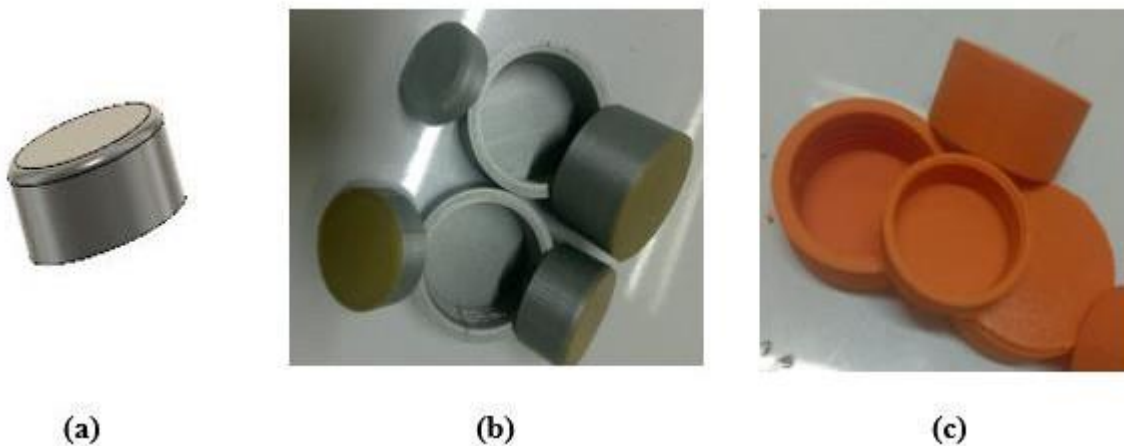


**Figure 29a:** Virtual (a) and printed models (b and c) of bottle caps

#### 4.6.2: Dispenser Pumps

The 3-D printed bottle caps and dispenser pumps were designed using Autodesk fusion 360 software as shown in figure 29b. The virtual models designed to scale had no extraneous configurations hence the virtual models were sliced into layers using the Ultimaker Cura software and transferred to a 3-D printer (Ultimaker <sup>2</sup>) using an SD card where they were printed using the fused deposition modelling method. This technique involved the extrusion of the molten PLA and ABS polymers through the extruder head. The heated nozzle moved along the extrusion path in vertical and horizontal directions as governed by the computer-aided manufacturing software package. The polymers were cooled from glass transition temperatures of 65<sup>0</sup>C and 105<sup>0</sup>C hence minimizing part fabrication failure or cracking due to internal stress.

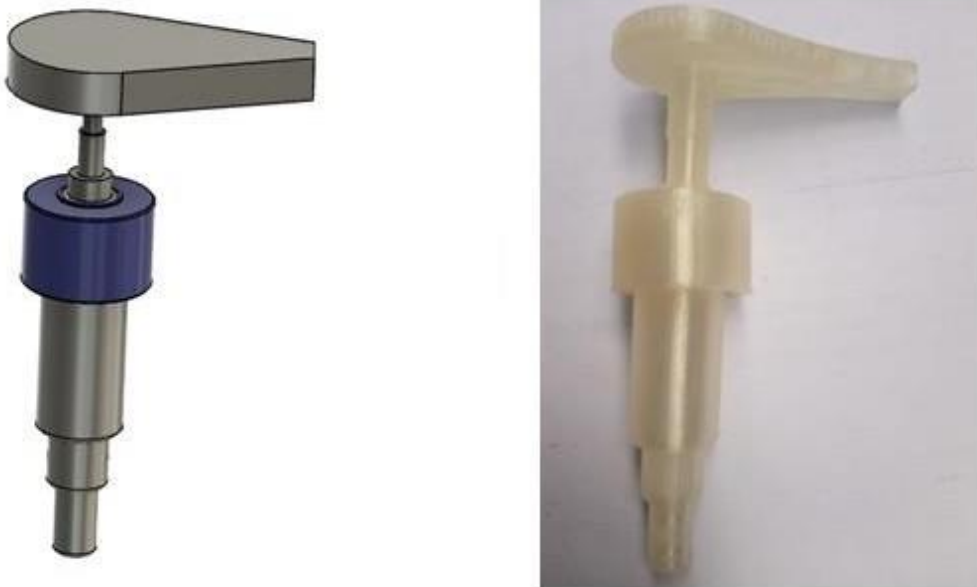


**Figure 29b:** Virtual and printed model dispenser pump

#### 4.7: Characterization of the 3-D printed dispenser

##### 4.7.1: Scanning electron microscopy.

The surface morphology of the PLA and ABS was shown in the SEM images (Figures 30a and 30b). Figure 30a revealed that at a magnification of 2.19kx, the PLA filament exhibited high interfacial adhesion, implying improved mechanical capabilities, but surface roughness was observed for the ABS at a magnification of 969 x, implying poor adhesive properties throughout the printing process. Furthermore, the appearance of gaps between the pores suggested that the ABS molecules' motion was inhibited by poor interfacial compatibility. The rigidity of both polymers, as indicated by the high-resolution magnification, is expected to have

resulted from the steady movement of the print head in the course of the extrusion and cooling stages.

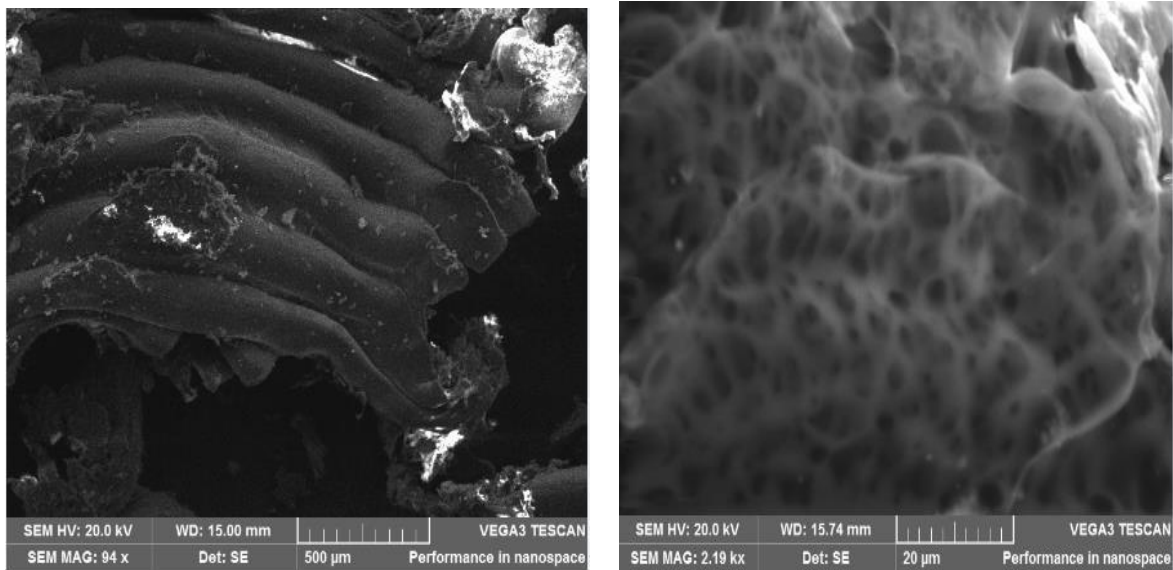


**Figure 30a:** SEM images for PLA

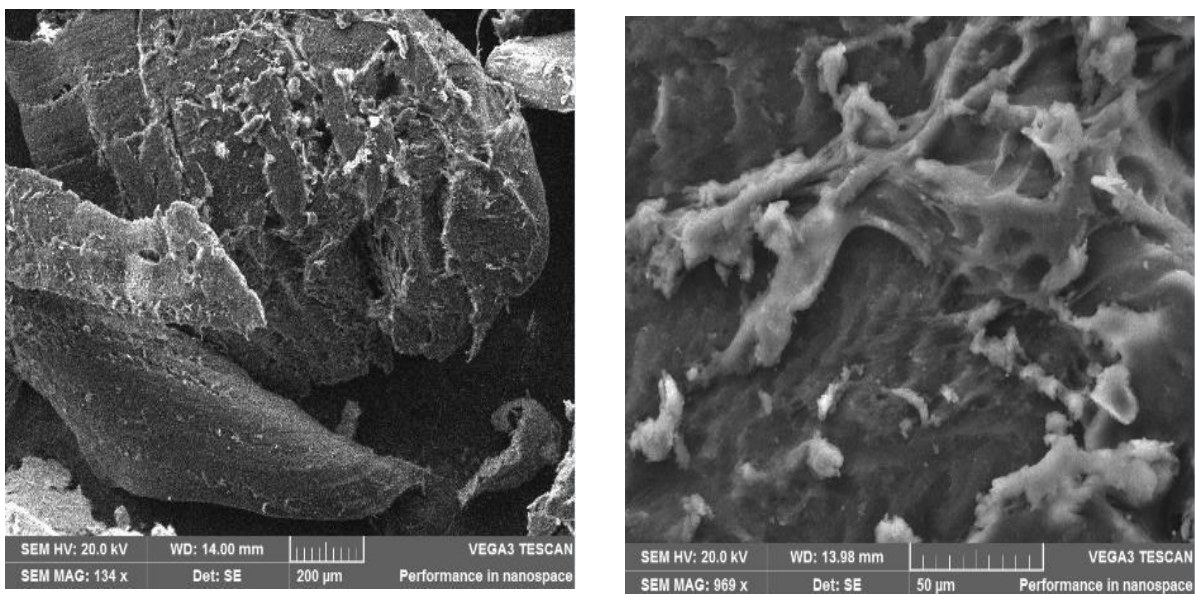
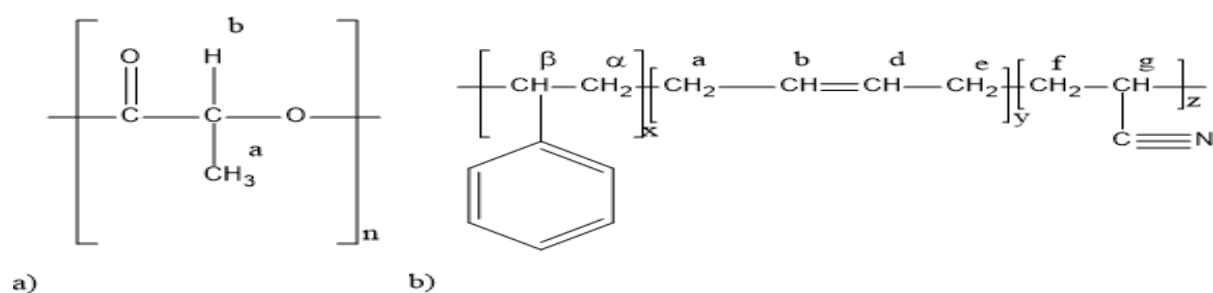


**Figure 30b:** SEM images for ABS

#### 4.7.2: Nuclear Magnetic Resonance (NMR)

The spectrum obtained in figure 31a showed a characteristic methyl (-CH<sub>3</sub>) and methine (-CH) chemical shift of the PLA peak centered at 1.47 ppm and a doublet centered at about 5.1 ppm, respectively. The integration of the peaks was consistent with the structure of the PLA polymer

(scheme 6) and showed a ratio of 3:1 (Onyari *et al.*, 2008). As shown in figure 31b, the hydrogen protons ( $\beta$   $\alpha$  a, e, f, g) chemical shifts were observed at 0.86 - 2.04ppm while the vinyl (-CH=CH) protons of the butadiene structure was observed at 5.37ppm. The chemical shifts observed from 6.75-7.23 ppm demonstrate the presence of an aromatic structure (Otieno *et al.*, 2022). The methylene (-CH<sub>2</sub>) and methine (-CH) signals observed are consistent with the findings of previous studies (Du *et al.*, 2011). The chemical structures of the polymers are consistent with the <sup>1</sup>H NMR spectra obtained in this study.



**Scheme 6:** Structures of a) PLA b) ABS

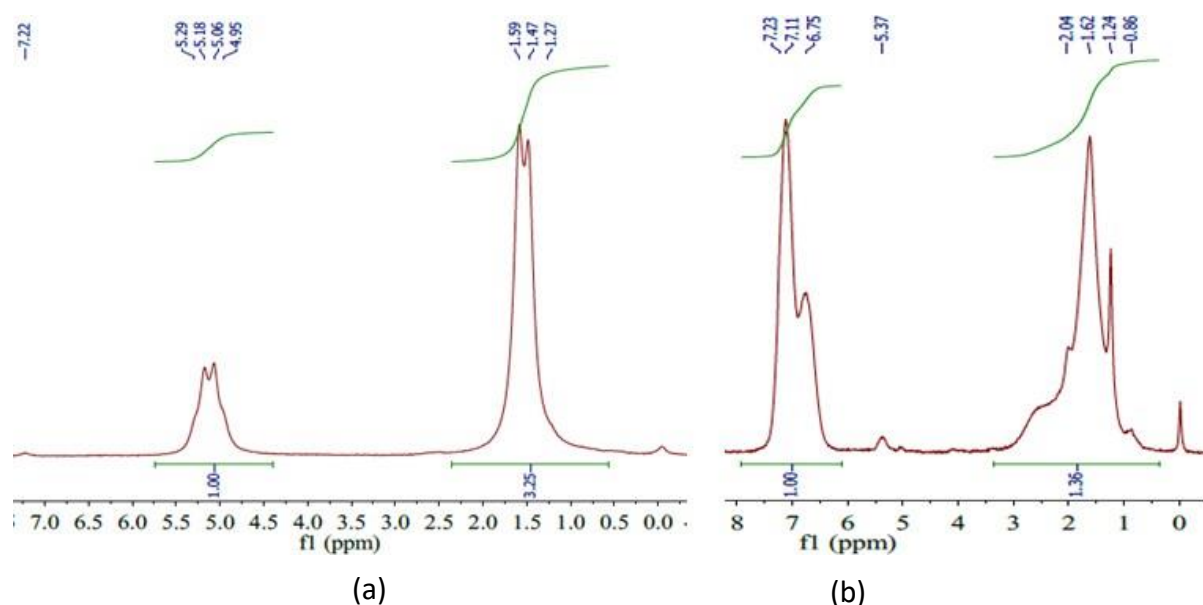


**Figure 31:** PLA (a) and ABS (b) <sup>1</sup>H-NMR spectra

### 4.7.3: Fourier Transform Infrared (FTIR)

FTIR spectroscopy was used to study the functional groups and their interactions in PLA and ABS polymers as shown in figure 32a. Different functional groups were observed in the PLA FTIR spectrum. Regions of interest were at 869.90 and 756.10  $\text{cm}^{-1}$  which were associated with C-C stretching, 1074.31 and 1180.44  $\text{cm}^{-1}$  were attributed to C-O-C stretching, 1041.56  $\text{cm}^{-1}$  was for C-CH<sub>3</sub>, 1361.74 and 1454.33  $\text{cm}^{-1}$  were referenced to CH-CH<sub>3</sub>. The peak at 2995.45  $\text{cm}^{-1}$  was linked to C-H stretching which appeared more pronounced at the beginning but later shifted to lower wavelengths. The O-H stretch was referenced to the band at 3454.78  $\text{cm}^{-1}$ . In addition, C-H stretch was ascribed to the peak at 2945.30  $\text{cm}^{-1}$ . The sharper 1747.51  $\text{cm}^{-1}$  absorbance peak is attributable to the C=O ester stretching. The ABS spectrum showed several absorbance peaks at 698.23 and 759.95  $\text{cm}^{-1}$  which were associated with CH<sub>2</sub> aromatic ring in styrene, the peak at 910.40  $\text{cm}^{-1}$  was attributed to CH<sub>2</sub> in vinyl butadiene, the peak at 964.41  $\text{cm}^{-1}$  was attributed to CH in trans butadiene, at 1452.40 and 1494.83  $\text{cm}^{-1}$  the peaks were associated with symmetric CH<sub>2</sub> and aromatic ring in styrene. The peak at 3026.31  $\text{cm}^{-1}$  was associated with C-H aromatic stretch. Asymmetric CH<sub>2</sub> was associated with the absorption peak at 2918.30  $\text{cm}^{-1}$ . The weaker bands located between 1696 - 1765  $\text{cm}^{-1}$  may have originated from a C=O stretching in an ester compound. The ester could have resulted from additives such as heat stabilizers added during formulation. It might also be the result of oxidation during the extrusion of the ABS polymer. That is supported by the fact that at 2237.43  $\text{cm}^{-1}$ , a nitrile group was identified thus implying that the ester group may have resulted from the acrylonitrile monomer. Besides the functional group analysis by FTIR, vibrational analysis was conducted on the 3-D printed PLA and ABS to analyze the conformational distribution of its chains. The PLA polymer yielded a Raman spectrum shown in Figure 32b. The peak at 2944.14  $\text{cm}^{-1}$  was referenced to the C-H stretching mode. In addition, the characteristic Raman band associated with C=O stretch appeared at 1765.04  $\text{cm}^{-1}$ . The vibrational peak at 1452.248  $\text{cm}^{-1}$  was ascribed to CH<sub>3</sub> asymmetric mode while at 872.77  $\text{cm}^{-1}$ , the C-COO stretching was identified. On the contrary, the ABS polymer was found to be Raman inactive.

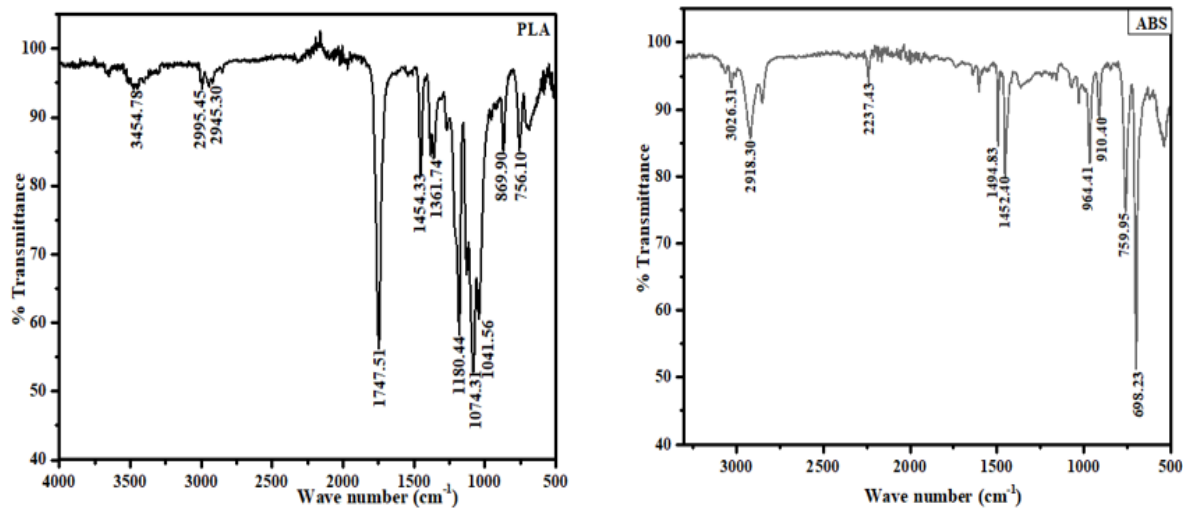


**Figure 32a:** FTIR spectra of PLA and ABS

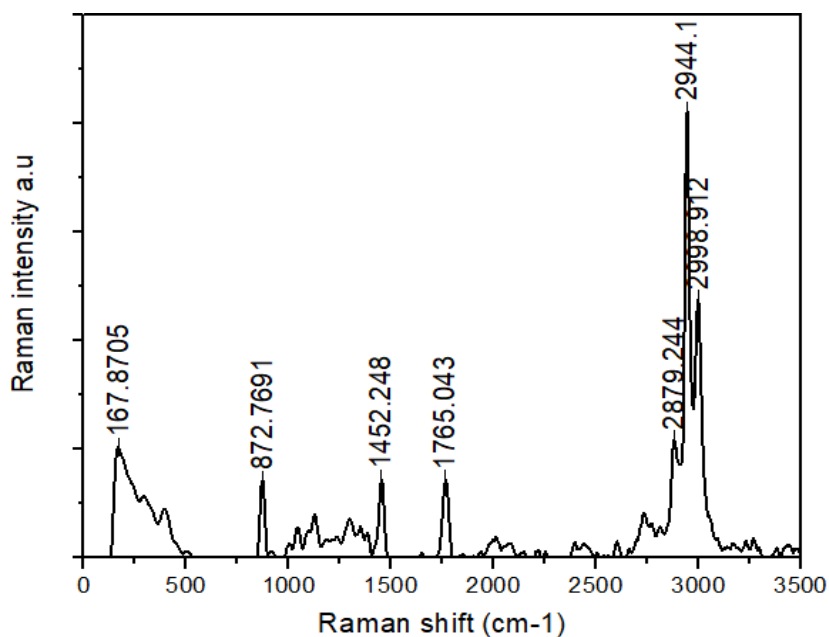


**Figure 32b:** Raman spectrum of PLA

#### 4.7.4: X-ray Fluorescence

A high amount of tin was present in the PLA sample unlike in ABS where small traces were determined as observed in table 7. This could be attributed to tin octanoate used as a catalyst during the industrial production of the PLA polymer. Calcium carbonate a common additive used in the manufacture of most polymers including ABS and PLA accounts for the traces of calcium concentration. The high iron concentration in PLA can be associated with the wear and tear of the metal components used during the processing of the filaments such as the shredder and extruder as in agreement with (Cress *et al.*, 2020). A significant amount of flame-

retardant additive was identified by the presence of a notable phosphorus content in both polymers. The application of titanium dioxide pigment to whiten the ABS polymer during production owing to its higher concentration. The presence of greater amounts of silica could be traced from silica oxide which acts as a filler during production to aid in the chemical and thermal stability of both polymers. It is noteworthy to mention that a high amount of sulphur was detected in ABS compared to PLA polymer. This is because sulphur forms cross-linking bonds during the vulcanization of polybutadiene rubber. An insignificant amount of chromium was detected for both polymers. These results are equally supported by studies done by (Cress *et al.*, 2020).

**Table 7:** Elemental composition of PLA and ABS obtained in ppm (parts per million)

<b>Elements</b>	<b>Polylactic acid</b>	<b>Acrylonitrile Butadiene Styrene</b>
Silica	550.0	416.0
Tin	862.7	87.60
Phosphorus	12.30	75.00
Sulphur	60.70	712.0
Potassium	98.70	92.20
Calcium	104.0	596.0
Titanium	9.490	1020
Chromium	7.760	0.992
Iron	299.0	29.50

#### **4.8: Determination of mechanical properties of the designed bottle caps and dispenser pumps.**

Table 8 showed the mechanical properties of the 3-D printed samples. All three PLA (grey, blue and black) and ABS (orange) grades exhibited a tensile strength of 44.21,40.39, 36.63, and 16.12 MPa respectively. The grey samples in particular, with an infill percentage of 80% had higher tensile strength (42.78,44.21,35.91 MPa) compared to the other infill percentages of 40 and 60 (35.42,36.02,35.54 MPa and 39.22,34.46,28.63 MPa) respectively. The orange ABS sample printed at an infill percentage of 60 showed tensile strength and elongation at breaks of 16.09,16.12, 16.12 MPa and 18.06, 18.09, 18.09% compared to those printed at 80 % (16.12, 16.39, 16.18 MPa and 18.12, 18.18, 18.10 %). This could be attributed to the effect of different infill percentages of 40,60 and 80% used to print the samples and modification of

the pristine filaments into 3-D materials to suit the performance and customer requirements. Lower experimental values of some mechanical properties such as elongation at break for the rigid PLA and ABS samples were attributed to filament orientation of 0o/90o in the course of printing. Because of the raster orientation, the porosities increased, resulting in higher stress concentrations and poor bonding properties of the 3-D printed polymers. It is noteworthy to mention that as the infill percentage used for 3-D printing increases, there is a proportional increase in the strength and stiffness of the specimen due to a reduction in the strain of failure. This would also imply less deformation under a static load. This is evident from the low values of elongation at break for the grey, blue, and black samples observed in table 8. All the printed PLA and ABS specimens exhibited a hardness of 100 using the shore D durometer. To minimize the raw material and energy used, the grey and orange samples printed with an infill percentage of 40% would be highly recommended.

**Table 8:** Mechanical properties of the 3-D printed PLA and ABS samples

Grade	Color	Infill percent age (%)	Tensile Strength (Mpa)			Elongation at Break (%)			Hardness		
			(for three printed samples)			(for three printed samples)			For the three printed samples		
1	PLA	40	35.42	36.02	35.54	16.80	18.60	18.00	100	100	100
	Grey	60	39.22	34.46	28.63	16.00	19.30	19.70	100	100	100
		80	42.78	44.21	35.91	16.70	18.00	23.30	100	100	100
2	PLA	40	38.30	30.95	34.09	19.30	19.30	19.30	100	100	100
	Blue	60	35.59	36.82	38.12	16.70	19.30	19.30	100	100	100
		80	38.18	37.42	40.39	19.70	19.70	19.70	100	100	100
3	PLA	40	21.09	31.33	31.70	18.30	18.30	18.30	100	100	100
	Black	60	21.72	35.96	33.06	16.70	19.30	19.30	100	100	100
		80	35.05	36.63	32.13	19.30	19.30	23.30	100	100	100
4	ABS	60	16.09	16.12	16.12	18.06	18.09	18.09	100	100	100
	Orange	80	16.12	16.39	16.18	18.12	18.18	18.10	100	100	100

#### 4.9: Characterization of Zinc Oxide and Copper Oxide

The synthesized zinc oxide nanocrystals had absorption bands at 705.95cm<sup>-1</sup>, 829.39



$\text{cm}^{-1}$ ,  $1047.35\text{cm}^{-1}$ ,  $1392.61\text{cm}^{-1}$ ,  $1500.62\text{cm}^{-1}$ , and  $3309.85\text{ cm}^{-1}$ . The presence of the Zn-O bond exhibited the formation of zinc oxide compound after the annealing process which was later supported by stretching vibrations at  $705.95\text{ cm}^{-1}$ . The peaks at  $1047.35\text{ cm}^{-1}$  and  $1392.61\text{ cm}^{-1}$  revealed the presence of C-O-C and C-O stretching modes respectively. Further, the absorption peaks at  $1500.62\text{ cm}^{-1}$  and  $3309.85\text{ cm}^{-1}$  were ascribed to the O-H group. The FTIR spectrum for CuO nanoparticles shown in figure 33 indicated the presence of a Cu-O bond. It shows the formation of copper oxide after the annealing process which is equally attributed to Cu-O stretching modes observed at  $570.0\text{ cm}^{-1}$ . The bands within the range of  $1380\text{-}1640\text{ cm}^{-1}$  were designated to O-H vibrations combined with copper atoms. The broad absorption peak at  $3363.86\text{ cm}^{-1}$  is due to the presence of adsorbed OH since the copper nanoparticles had increased surface area to volume ratio to absorb moisture.

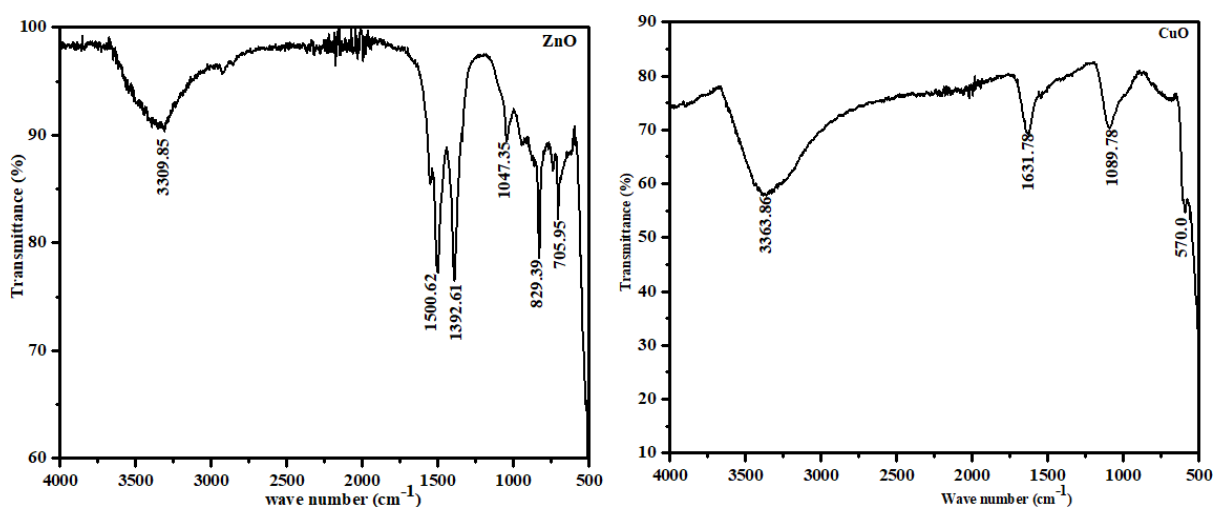


**Figure 33:** FTIR spectra of ZnO and CuO nanoparticles.

#### 4.10: Antimicrobial activity of ZnO and CuO nanocrystals

ZnO and CuO nanoparticles generated zones of inhibition as observed in figure 34. The measurements of the inhibition zones of bacterial growth were been tabulated in table 9. It is worth mentioning that in this particular study, ZnO and CuO nanoparticles had an antimicrobial effect against *Escherichia coli*. Zinc oxide nanoparticles were observed to be slightly ineffective on *Bacillus thuringiensis*. Narayan and team also determined the efficacy of zinc oxide nanoparticles against *Escherichia coli* to be higher (Narayanan *et al.*, 2012). However, in a study done by Ahmed and coworkers (2014), copper oxide nanoparticles were found to exhibit an inhibitory effect against most gram-negative and positive bacterial strains including *Pseudomonas aeruginosa* and *Escherichia coli* respectively. Various mechanisms including

deposition of the nanoparticles on the bacteria surface, disruption of the cellular operations of the bacteria by the accumulation of the nanoparticles in the periplasmic region of the cell, and formation of active hydroxyls explain the interaction between nanoparticles and different bacteria strains. Zinc oxide and copper oxide in particular destroyed the cytoplasmic membrane by neutralizing the respiratory enzymes and immersing the cytoplasm contents in an outward direction. This process interfered with the cellular membrane hence killing the bacteria and resulting in a zone of inhibition of bacterial growth (Chopra *et al.*, 2020; Sirelkhatim *et al.*, 2015).

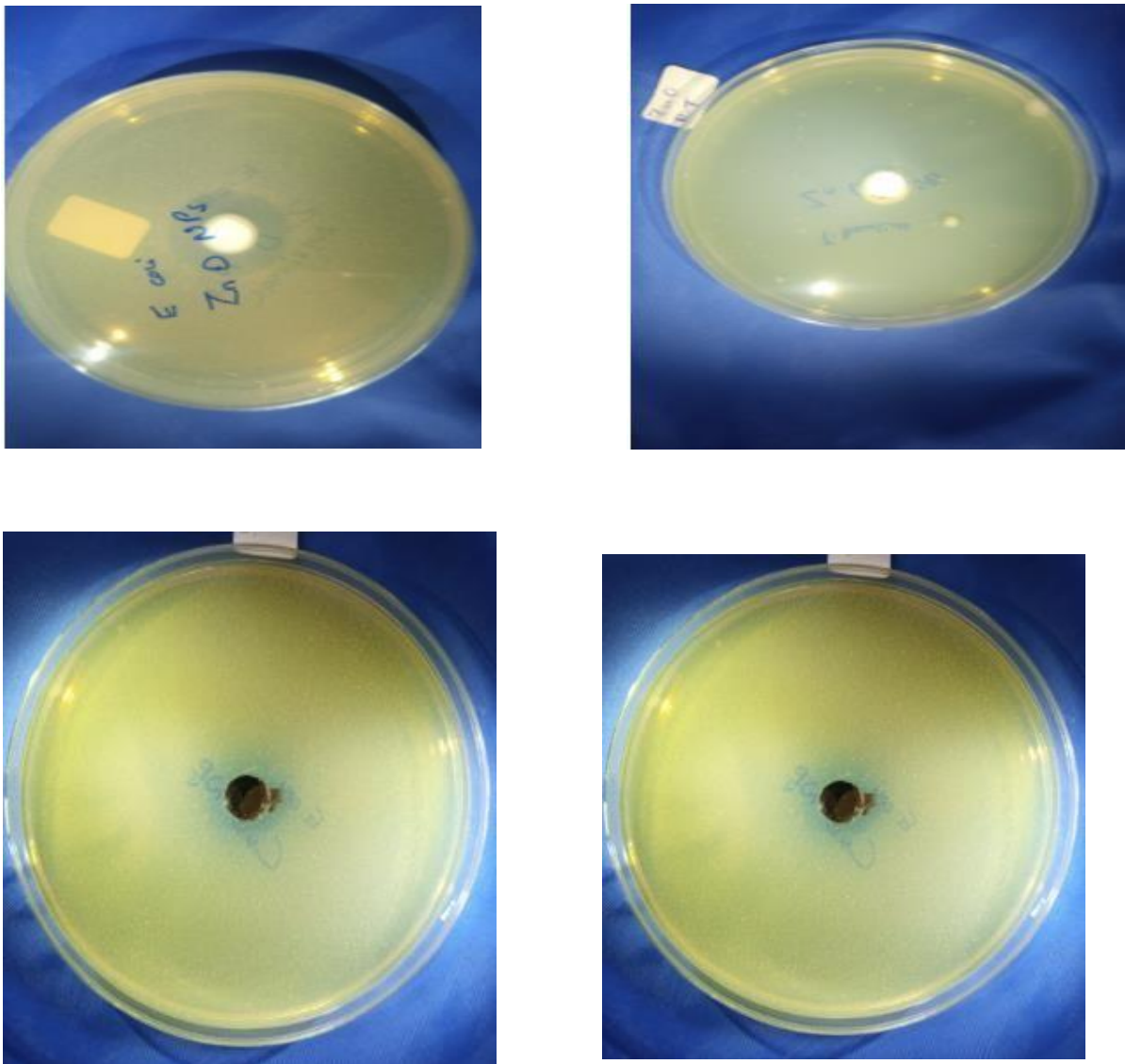


**Figure 34:** Antimicrobial activity of ZnO and CuO Nanocrystals

**Table 9:**Inhibition measurements of zinc oxide nanoparticles

<b>Sample</b>	<b>Bacteria scientific name</b>	<b>Bacteria type</b>	<b>Inhibition</b>
ZnO NPs	<i>Escherichia coli</i>	Gram negative	(mm)
CuO NPs	<i>Escherichia coli</i>	Gram negative	371.96
ZnO NPs	<i>Bacillus</i>	Gram positive	170.47
CuO NPs	<i>thuringiensis</i>	Gram positive	N/A

## CHAPTER 5: CONCLUSIONS AND RECOMMENDATIONS

### 5.1: Conclusions

The theoretical computation simulations of both polymers provided satisfactory scientific data which complemented experimental data reported in this study and elsewhere. In this research, the fabrication of PLA and ABS bottle caps and dispenser pumps was accomplished through 3-D printing. FTIR functional group analysis of the two polymers revealed the presence of ester and hydroxyl groups (-OH) in the PLA sample suggesting quicker degradation in comparison to the aromatic groups in ABS which is non-biodegradable because of significant steric hindrance. The grey PLA grades printed with an infill percentage of 80% exhibited better mechanical properties than the blue and black grades. The orange ABS with a similar infill percentage equally showed good properties. The synthesized ZnO and CuO nanoparticles exhibited antibacterial effects on gram-negative *Escherichia coli* and little effect on gram-positive *Bacillus thuringiensis*. Given that PLA is biodegradable and hence greener, the findings of this work will serve as a springboard for further research studies on PLA modifications that would generate PLA-based polymer blends and composites that are comparable to conventional polymers used in packaging.

### 5.2: Recommendations

Exploration for further work should look into;

1. Development of PLA and ABS polymer blends

An investigation on formulation of modified polylactic acid blends is suggested. The addition of more additives to the pristine polymer is foreseen to improve the mechanical and antimicrobial properties of the frequently touched PLA surfaces.

2. Optimization of the nanoparticles' synthesis process

Optimization of the zinc oxide and copper oxide nanoparticles synthesis process will help determine the conditions and concentration of maximum yield. Further tests are to be done on the antibacterial properties of zinc oxide nanoparticles on other gram-positive and gram-negative bacteria besides *Bacillus thuringiensis* and *Escherichia coli* respectively to test its effectiveness.

3. Computation of PLA, ABS, ZnO and CuO NPS.

More computational studies are to be done using other modules and simulation techniques on the interaction of various polymers and other additives including PLA, ABS, copper oxide, and zinc oxide nanocrystals. This is to enhance the comparison of computational simulations and experimental data in the context of PLA and ABS properties.

## REFERENCES

- Aalto-Korte, K., & Suuronen, K. (2019). Plastic materials and glues. In: Johansen, J., Mahler, V., Lepoittevin, JP., Frosch, P. (eds) Contact Dermatitis. Springer, Cham, 1-28. [https://doi.org/10.1007/978-3-319-72451-5\\_79-1](https://doi.org/10.1007/978-3-319-72451-5_79-1)
- Abd Alsaheb, R. A., Aladdin, A., Othman, N. Z., Abd Malek, R., Leng, O. M., Aziz, R., & El Enshasy, H. A. (2015). Recent applications of polylactic acid in pharmaceutical and medical industries. *J. Chem. Pharm. Res*, **7**(12), 51–63.
- Abdalla, M. A. M., Peng, H., Wu, D., Abusin, L., & Mbah, T. J. (2018). Prediction of Hydrophobic Reagent for Flotation Process Using Molecular Modeling. *ACS Omega*, **3**(6), 6483–6496. <https://doi.org/10.1021/acsomega.8b00413>
- Abukasim, S. M., Zuhria, F., & Saing, Z. (2020). Alternative management of plastic waste. *J Phys Conf Ser*, **1517**, 12041. <https://doi.org/10.1088/1742-6596/1517/1/012041>
- Adeniran, A. A., & Shakantu, W. (2022). The Health and Environmental Impact of Plastic Waste Disposal in South African Townships: A Review. *Int J Environ Res Public Health*, **19**(2), Article 2. <https://doi.org/10.3390/ijerph19020779>
- Agarwal, H., Kumar, S. V., & Rajeshkumar, S. (2017). A review on green synthesis of zinc oxide nanoparticles—An eco-friendly approach. *Resource-Efficient Technologies*, **3**(4), 406–413.
- Ahamed, M., Alhadlaq, H. A., Khan, M. A., Karuppiah, P., & Al-Dhabi, N. A. (2014). Synthesis, characterization, and antimicrobial activity of copper oxide nanoparticles. *J Nanomater*, 2014.
- Alabi, O., Ologbonjaye, K., Awosolu, O., & Alalade, O. (2019). Public and Environmental Health Effects of Plastic Wastes Disposal: A Review. *Journal of Toxicology and Risk Assessment*, **5**. <https://doi.org/10.23937/2572-4061.1510021>
- Al-Bayati, A. J., & Al-Zubaidi, H. A. (2018). Inventory of Nanomaterials in Construction Products for Safety and Health. *J Constr Eng Manag*, **144**(9), 06018004. [https://doi.org/10.1061/\(ASCE\)CO.1943-7862.0001547](https://doi.org/10.1061/(ASCE)CO.1943-7862.0001547)

Alda-Vidal, C., Browne, A. L., & Hoolohan, C. (2020). “Unflushables”: Establishing a global agenda for action on everyday practices associated with sewer blockages, water quality, and plastic pollution. *Wiley Interdisciplinary Reviews: Water*, **7**(4), e1452.

Alkorta, I., & Elguero, J. (2003). Review on DFT ab initio calculations of scalar coupling constants. *Int J Mol Sci*, **4**(3), 64–92.

Almaguer-Flores, A., Ximénez-Fyvie, L. A., & Rodil, S. E. (2010). Oral bacterial adhesion on amorphous carbon and titanium films: Effect of surface roughness and culture media. *J Biomed Mater Res Part B: Applied Biomaterials: An Official Journal of The Society for Biomaterials, The Japanese Society for Biomaterials, and The Australian Society for Biomaterials and the Korean Society for Biomaterials*, **92**(1), 196–204.

Amza, C. G., Zapciu, A., Constantin, G., Baciu, F., & Vasile, M. I. (2021). Enhancing mechanical properties of polymer 3-D printed parts. *Polym*, **13**(4), 562.

Andreeßen, C., & Steinbüchel, A. (2019). Recent developments in non-biodegradable biopolymers: Precursors, production processes, and future perspectives. *Appl Microbiol Biotechnol*, **103**, 143–157. <https://doi.org/10.1007/s00253-018-9483-6>

Aouadi, S. M. (2006). Structural and mechanical properties of TaZrN films: Experimental and *ab initio* studies. *J Appl Phys*, **99**(5), 053507. <https://doi.org/10.1063/1.2178394>

Armijo, P. R., Markin, N. W., Nguyen, S., Ho, D. H., Horseman, T. S., Lisco, S. J., & Schiller, A. M. (2021). 3D printing of face shields to meet the immediate need for PPE in anesthesiology department during the COVID-19 pandemic. *Am J Infect Control*, **49**(3), 302–308.

AshaRani, P. V., Low Kah Mun, G., Hande, M. P., & Valiyaveetil, S. (2009). Cytotoxicity and genotoxicity of silver nanoparticles in human cells. *ACS Nano*, **3**(2), 279–290.

Auras, R. (2002). Poly (lactic acid). *Encyclopedia of Polymer Science and Technology*. <https://doi.org/10.1002/0471440264.pst275>

Ayawei, N., Ebelegi, A. N., & Wankasi, D. (2017). Modelling and Interpretation of Adsorption Isotherms. *J Chem*, **2017**, 1–11. <https://doi.org/10.1155/2017/3039817>

Ayawei, N., Ekubo, A. T., Wankasi, D., & Dikio, E. D. (2015). Adsorption of congo red by Ni/Al-CO<sub>3</sub>: Equilibrium, thermodynamic and kinetic studies. *Orient J Chem*, **31**(3), 1307.

- Ayers, P. W., Morell, C., De Proft, F., & Geerlings, P. (2007). Understanding the Woodward–Hoffmann Rules by Using Changes in Electron Density. *Chem – A European Journal*, **13**(29), 8240–8247. <https://doi.org/10.1002/chem.200700365>
- Bali, C., Brandlmaier, A., Ganster, A., Raab, O., Zapf, J., & Hübler, A. (2016). Fully inkjet-printed flexible temperature sensors based on carbon and PEDOT: PSS. *Mater Today: Proceedings*, **3**(3), 739–745.
- Bellini, A., Güçeri, S., & Bertoldi, M. (2004). Liquefier Dynamics in Fused Deposition. *J Manuf Sci Eng*, **126**(2), 237–246. <https://doi.org/10.1115/1.1688377>
- Berekaa, M. M. (2015). *Nanotechnology in Food Industry; Advances in Food processing, Packaging and Food Safety*. *Int J Curr Microbiol App Sci*, **4**(5), 345–357.
- Biçen Ünlüer, Ö., Emir Diltemiz, S., Say, M. G., Hür, D., Say, R., & Ersöz, A. (2022). A powerful combination in designing polymeric scaffolds: 3-D bioprinting and cryogelation. *Int J Polym Mater*, **71**(4), 278–290.
- Bickelhaupt, F. M., & Baerends, E. J. (2000). Kohn-Sham density functional theory: Predicting and understanding chemistry. *Rev Comput Chem*, **15**, 1–86. <https://doi.org/10.1002/9780470125922.ch1>
- Borrelle, S. B., Ringma, J., Law, K. L., Monnahan, C. C., Lebreton, L., McGivern, A., Murphy, E., Jambeck, J., Leonard, G. H., & Hilleary, M. A. (2020). Predicted growth in plastic waste exceeds efforts to mitigate plastic pollution. *Science*, **369**(6510), 1515–1518.
- Bouapao, L., & Tsuji, H. (2009). Stereocomplex Crystallization and Spherulite Growth of Low Molecular Weight Poly(L-lactide) and Poly(D-lactide) from the Melt. *Macromol Chem Phys*, **210**(12), 993–1002. <https://doi.org/10.1002/macp.200900017>
- Busscher, H. J., Uyen, M. H., Van Pelt, A. W., Weerkamp, A. H., & Arends, J. (1986). Kinetics of adhesion of the oral bacterium *Streptococcus sanguis* CH<sub>3</sub> to polymers with different surface free energies. *Appl Environ Microbiol*, **51**(5), 910–914.
- Caglar, B., Kizilkaya, A. C., Niemantsverdriet, J. W. (Hans), & Weststrate, C. J. (Kees-J. (2018). Application of work function measurements in the study of surface catalyzed reactions on Rh(1 0 0). *Catal Struct React*, **4**(1), 1–11. <https://doi.org/10.1080/2055074X.2018.1434986>



- Campos, A., Gómez, C. M., García, R., Figueruelo, J. E., & Soria, V. (1996). Extension of the Flory-Huggins theory to study incompatible polymer blends in solution from phase separation data. *Polym*, **37**(15), 3361–3372.
- Carrasco, F., Pagès, P., Gamez-Perez, J., Santana Perez, O., & MasPOCH, M. (2010). Processing of poly(lactic acid): Characterization of chemical structure, thermal stability and mechanical properties. *Polym Degrad Stab*, **95**, 116–125. <https://doi.org/10.1016/j.polymdegradstab.2009.11.045>
- Carvalho, C., Landers, R., Hübner, U., Schmelzeisen, R., & Mülhaupt, R. (2005). Fabrication of soft and hard biocompatible scaffolds using 3-D-Bioplotting™. *Virtual Modeling and Rapid Manufacturing—Advanced Research in Virtual and Rapid Prototyping*, 97–102.
- Chami Khazraji, A., & Robert, S. (2013). Self-assembly and intermolecular forces when cellulose and water interact using molecular modeling. *J Nanomater*, 2013.
- Chang, Y.-H., Wang, K., Wu, C., Chen, Y., Zhang, C., & Wang, B. (2015). A facile method for integrating direct-write devices into three-dimensional printed parts. *Smart Mater Struct*, **24**(6), 065008.
- Chaudhry, Q., Watkins, R., & Castle, L. (2010). *Nanotechnologies in the Food Arena: New Opportunities, New Questions, New Concerns*. (pp. 1–17). <https://doi.org/10.1039/9781847559883-00001>
- Chen, Z., Song, X., Lei, L., Chen, X., Fei, C., Chiu, C. T., Qian, X., Ma, T., Yang, Y., & Shung, K. (2016). 3-D printing of piezoelectric element for energy focusing and ultrasonic sensing. *Nano Energy*, **27**, 78–86.
- Choi, J., Kwon, O.-C., Jo, W., Lee, H. J., & Moon, M.-W. (2015). 4D printing technology: A review. *3-D Print Addit Manuf*, **2**(4), 159–167. <https://doi.org/10.1089/3dp.2015.0039>
- Chopra, R., Kashyap, N., Kumar, A., & Banerjee, D. (2020). Chemical Synthesis of Copper Oxide Nanoparticles Study of its Optical and Electrical Properties. *Int J Eng Res Technol*, **9**. <https://doi.org/10.17577/IJERTV9IS010160>
- Chow, C.-F., So, W.-M. W., Cheung, T.-Y., & Yeung, S.-K. D. (2017). Plastic Waste Problem and Education for Plastic Waste Management. In S. C. Kong, T. L. Wong, M. Yang, C. F. Chow, & K. H. Tse (Eds.), *Emerging Practices in Scholarship of Learning and Teaching in a*

*Digital Era*. Springer. Singapore: (pp. 125–140). [https://doi.org/10.1007/978-981-10-3344-5\\_8](https://doi.org/10.1007/978-981-10-3344-5_8)

Cifuentes, S. C., Frutos, E., Benavente, R., Lorenzo, V., & González-Carrasco, J. L. (2017). Assessment of mechanical behavior of PLA composites reinforced with Mg micro-particles through depth-sensing indentations analysis. *J Mech Behav Biomed Mater*, **65**, 781–790.

Cress, A., Huynh, J., Anderson, E., O’neill, R., Schneider, Y., & Keleş, Ö. (2020). Effect of recycling on the mechanical behavior and structure of additively manufactured acrylonitrile butadiene styrene (ABS). *J Cleaner Prod*, **279**, 123689. <https://doi.org/10.1016/j.jclepro.2020.123689>

De Weerd, L., Sasao, T., Compernelle, T., Van Passel, S., & De Jaeger, S. (2020). The effect of waste incineration taxation on industrial plastic waste generation: A panel analysis. *Res Con Rec*, **157**, 104717. <https://doi.org/10.1016/j.resconrec.2020.104717>

De-la-Torre, G. E. (2020). Microplastics: An emerging threat to food security and human health. *J Food Sci Technol*, **57**(5), 1601–1608.

Derby, B. (2011). Inkjet printing ceramics: From drops to solid. *J Eur Ceram Soc*, **31**(14), 2543–2550.

Dikovsky, D., & Napadensky, E. (2013). *Three-dimensional printing process for producing a self-destructible temporary structure*; US Patent 8470231B1.

Domb, A. J., & Kumar, N. (2011). *Biodegradable polymers in clinical use and clinical development*. John Wiley & Sons, New jersey: pp 200.

Du, A.-K., Zhou, Q., Wen, Z.-B., Yang, J.-W., van Kasteren, J. M., & Wang, Y.-Z. (2011). Denitrogenation of acrylonitrile–butadiene–styrene copolymers using polyethylene glycol/hydroxides. *Polym Degrad Stab*, **96**(5), 870–874.

Duffy, L. L., Osmond-McLeod, M. J., Judy, J., & King, T. (2018). Investigation into the antibacterial activity of silver, zinc oxide and copper oxide nanoparticles against poultry-relevant isolates of Salmonella and Campylobacter. *Food Control*, **92**, 293–300.

Dugan, J. (2001). Novel properties of PLA fibers. *Int Nonwovens J*, **10**, 29–33. <https://doi.org/10.1177/1558925001OS-01000308>

Ebewele, R. O. (2000). *Polymer science and technology*. CRC press, Florida: 440-449.

- Ebnesajjad, S. (2012). *Handbook of biopolymers and biodegradable plastics: Properties, processing and applications*. William Andrew, New York; 11-70.
- Endres, H.-J., & Siebert-Raths, A. (2011). Engineering biopolymers. *Eng. Biopolym*, **71148**, 3–15.
- Fan, C. F., Olafson, B. D., Blanco, M., & Hsu, S. L. (1992). Application of molecular simulation to derive phase diagrams of binary mixtures. *Macromolecules*, **25**(14), 3667–3676.
- Fattahi, F., Khoddami, A., & Avinc, O. (2019). Poly (Lactic Acid) nanofibres as drug delivery systems: Opportunities and challenges. *J Nanomed Res*, **4**(3), 130–140.
- Ficko, M., Drstvenšek, I., Brezočnik, M., Balič, J., & Vaupotic, B. (2005). Prediction of total manufacturing costs for stamping tool on the basis of CAD-model of finished product. *J Mater Process Technol*, **164**, 1327–1335.
- Frascella, F., González, G., Bosch, P., Angelini, A., Chiappone, A., Sangermano, M., Pirri, C. F., & Roppolo, I. (2018). Three-dimensional printed photoluminescent polymeric waveguides. *ACS Appl Mater Interfaces*, **10**(45), 39319–39326.
- Fucic, A., Galea, K. S., Duca, R. C., El Yamani, M., Frery, N., Godderis, L., Halldorsson, T. I., Iavicoli, I., Ndaw, S., & Ribeiro, E. (2018). Potential health risk of endocrine disruptors in construction sector and plastics industry: A new paradigm in occupational health. *Int J Environ Res Public Health*, **15**(6), 1229.
- Gamez-Perez, J. (2010). Fracture behaviour of quenched poly (lactic acid). *EXPRESS Polym. Lett*, **5**, 82–91. <https://doi.org/10.3144/expresspolymlett.2011.9>
- Gámez-Pérez, J., Velazquez-Infante, J. C., Franco-Urquiza, E., Carrasco, F., Santana, O. O., & Maspoch, M. L. (2011). Fracture behavior of quenched poly (lactic acid). *Express Polym Lett*, **5**(1).
- Ganesan, V., & Jayaraman, A. (2014). Theory and simulation studies of effective interactions, phase behavior and morphology in polymer nanocomposites. *Soft Matter*, **10**(1), 13–38.
- Gherasim, C., Pascariu Dorneanu, P., Asandulesa, M., Dobromir, M., Doroftei, F., Fifere, N., Dascalu, A., & Airinei, A. (2022). Copper oxide nanostructures: Preparation, structural, dielectric and catalytic properties. *Ceram Int*, **48** (7). <https://doi.org/10.1016/j.ceramint.2022.05.235>

- Ghosh, A., & Chakrabarty, S. (2011). The work function associated with ultra-relativistic electron emission from strongly magnetized neutron star surface. *J Astrophys Astron*, **32**(3), 377–390. <https://doi.org/10.1007/s12036-011-9090-8>
- Gillono, M., Chiappone, A., Mendola, L., Gomez Gomez, M., Scaltrito, L., Pirri, C. F., & Roppolo, I. (2019). Study on the printability through digital light processing technique of ionic liquids for CO<sub>2</sub> capture. *Polym*, **11**(12), 1932.
- Glehr, M., Leithner, A., Friesenbichler, J., Goessler, W., Avian, A., Andreou, D., Maurer-Ertl, W., Windhager, R., & Tunn, P. U. (2013). Argyria following the use of silver-coated megaprotheses: No association between the development of local argyria and elevated silver levels. *The Bone & Joint J*, **95**(7), 988–992.
- Gloria, A., Russo, T., De Santis, R., & Ambrosio, L. (2009). 3d Fiber Deposition Technique to Make Multifunctional and Tailor-Made Scaffolds for Tissue Engineering Applications. *Journal of Applied Biomater Biomech*, **7**(3), 141–152. <https://doi.org/10.1177/228080000900700301>
- Gooneie, A., Schuschnigg, S., & Holzer, C. (2017). A Review of Multiscale Computational Methods in Polymeric Materials. *Polym*, **9**(1), Article 1. <https://doi.org/10.3390/polym9010016>
- Gopi, K. S., & Srinivas, T. (2020). Feasibility study of recycled plastic waste as fine aggregate in concrete. *E3S Web of Conferences*, **184**, 01084. <https://doi.org/10.1051/e3sconf/202018401084>
- Guo, Y., Patanwala, H. S., Bognet, B., & Ma, A. W. (2017). Inkjet and inkjet-based 3-D printing: Connecting fluid properties and printing performance. *Rapid Prototyp J*, **23**(3), 562–576. <https://doi.org/10.1108/RPJ-05-2016-0076>
- Han, W., Jafari, M. A., & Seyed, K. (2003). Process speeding up via deposition planning in fused deposition-based layered manufacturing processes. *Rapid Prototyp J*, **9**(4), 212–218. <https://doi.org/10.1108/13552540310489596>
- Hardin, J. O., Ober, T. J., Valentine, A. D., & Lewis, J. A. (2015). Microfluidic printheads for multimaterial 3-D printing of viscoelastic inks. *Adv Mater*, **27**(21), 3279–3284. <https://doi.org/10.1002/adma.201500222>

- Harrysson, O., & Cormier, D. (2006). Direct fabrication of custom orthopedic implants using electron beam melting technology. *Advanced Manufacturing Technology for Medical Applications*, 193–208.
- Harrysson, O. L., Cansizoglu, O., Marcellin-Little, D. J., Cormier, D. R., & West II, H. A. (2008). Direct metal fabrication of titanium implants with tailored materials and mechanical properties using electron beam melting technology. *Mater Sci Eng: C*, **28**(3), 366–373.
- Haynes, W. M. (2014). *CRC handbook of chemistry and physics*. CRC press, Florida: 10-73.
- Heinlaan, M., Ivask, A., Blinova, I., Dubourguier, H.-C., & Kahru, A. (2008). Toxicity of nanosized and bulk ZnO, CuO and TiO<sub>2</sub> to bacteria *Vibrio fischeri* and crustaceans *Daphnia magna* and *Thamnocephalus platyurus*. *Chemosphere*, **71**(7), 1308–1316. <https://doi.org/10.1016/j.chemosphere.2007.11.047>
- Henton, D. E., Gruber, P., Lunt, J., & Randall, J. (2005). Polylactic acid technology. *Natural fibers, biopolymers, and biocomposites*, **16**, 527–577.
- Hortos Llobera, M., Espino, S., & Bou Serra, J. (2019). Influence of temperature on high molecular weight poly (lactic acid) stereocomplex formation. *Express Polym Lett*, **13**(2), 123–134.
- Horvath, D., Noorani, R., & Mendelson, M. (2007). Improvement of surface roughness on ABS 400 polymer using design of experiments (DOE). *Materials Science Forum*, **561**, 2389–2392.
- Hottle, T. A., Agüero, M. L., Bilec, M. M., & Landis, A. E. (2016). Alkaline amendment for the enhancement of compost degradation for polylactic acid biopolymer products. *Compost Sci Util*, **24**(3), 159–173.
- Hoyle, C. E., & Bowman, C. N. (2010). Thiol–Ene Click Chemistry. *Angew Chem Int Ed*, **49**(9), 1540–1573. <https://doi.org/10.1002/anie.200903924>
- Hu, Y., Daoud, W. A., Cheuk, K. K. L., & Lin, C. S. K. (2016). Newly Developed Techniques on Polycondensation, Ring-Opening Polymerization and Polymer Modification: Focus on Poly(Lactic Acid). *Materials*, **9**(3), Article 3. <https://doi.org/10.3390/ma9030133>
- Huang, S. J., & Onyari, J. M. (1996). Multicomponent polymers of poly (lactic acid) macromonomers with methacrylate terminal and copolymers of poly (2-hydroxyethyl methacrylate). *J Macromol Sci, Part A: Pure and Applied Chemistry*, **33**(5), 571–584.

- Huang, S., Wang, H., Ahmad, W., Ahmad, A., Ivanovich Vatin, N., Mohamed, A. M., Deifalla, A. F., & Mehmood, I. (2022). Plastic Waste Management Strategies and Their Environmental Aspects: A Scientometric Analysis and Comprehensive Review. *Int J Environ Res Public Health*, **19**(8), Article 8. <https://doi.org/10.3390/ijerph19084556>
- Hussein, A., Hao, L., Yan, C., & Everson, R. (2013). Finite element simulation of the temperature and stress fields in single layers built without-support in selective laser melting. *Materials & Design (1980-2015)*, **52**, 638–647. <https://doi.org/10.1016/j.matdes.2013.05.070>
- IETC. (2021, January 26). *Enhancing Circular Economy Perspectives—Plastic Waste Management Strategy and Action Plan for Greater Hyderabad Municipal Corporation*. International Environmental Technology Centre. <http://www.unep.org/ietc/resources/policy-and-strategy/enhancing-circular-economy-perspectives-plastic-waste-management>
- Imad, E. M. N., Asim, A. E., & Tasneem, J. M. S. (2017). Management of Post-Consumer Pharmaceutical Waste: An Overview. *SOJ Pharm Pharm Sci*, **4**(5), 1–5.
- Jadoun, S. (2019). Polylactide (PLA) based nanocomposites for applications in antibacterial/microbial and biomedical engineering. *Biocompos Biomed*, **6**, 69-80.
- Jamshidian, M., Tehrany, E. A., Imran, M., Jacquot, M., & Desobry, S. (2010). Poly-Lactic Acid: Production, Applications, Nanocomposites, and Release Studies. *Compr Rev Food Sci Food Saf*, **9**(5), 552–571. <https://doi.org/10.1111/j.1541-4337.2010.00126.x>
- Jem, K. J., & Tan, B. (2020). The development and challenges of poly (lactic acid) and poly (glycolic acid). *Adv Ind Eng Polym Res*, **3**(2), 60–70. <https://doi.org/10.1016/j.aiepr.2020.01.002>
- Jiang, J., Pi, J., & Cai, J. (2018). The advancing of zinc oxide nanoparticles for biomedical applications. *Bioinorg Chem Appl*, **2018**. <https://doi.org/10.1155/2018/1062562>
- Jiang, S., Chen, P., Zhan, Y., & Zhao, C. (2020). Theoretical and computational analysis on the melt flow behavior of polylactic acid in material extrusion additive manufacturing under vibration field. *Appl Sci*, **10**(11), 3801. Article 11. <https://doi.org/10.3390/app10113801>
- Jones, N., Ray, B., Ranjit, K. T., & Manna, A. C. (2008). Antibacterial activity of ZnO nanoparticle suspensions on a broad spectrum of microorganisms. *Microbiol Lett*, **279**(1), 71–76. <https://doi.org/10.1111/j.1574-6968.2007.01012.x>

- Joshi, M. P., Pudavar, H. E., Swiatkiewicz, J., Prasad, P. N., & Reianhardt, B. A. (1999). Three-dimensional optical circuitry using two-photon-assisted polymerization. *Appl Phys Lett*, **74**(2), 170–172.
- Kale, G., Auras, R., Singh, S. P., & Narayan, R. (2007). Biodegradability of polylactide bottles in real and simulated composting conditions. *Polym Test*, **26**(8), 1049–1061. <https://doi.org/10.1016/j.polymertesting.2007.07.006>
- Kamel, S. (2007). Nanotechnology and its applications in lignocellulosic composites, a mini review. *Express Polym Lett*, **1**(9), 546–575.
- Katsikogianni, M., Spiliopoulou, I., Dowling, D. P., & Missirlis, Y. F. (2006). Adhesion of slime producing *Staphylococcus epidermidis* strains to PVC and diamond-like carbon/silver/fluorinated coatings. *J Mater Sci: Mater Med*, **17**(8), 679–689.
- Kedzierski, M., Frère, D., Le Maguer, G., & Bruzard, S. (2020). Why is there plastic packaging in the natural environment? Understanding the roots of our individual plastic waste management behaviours. *Sci Total Environ*, **740**, 139985. <https://doi.org/10.1016/j.scitotenv.2020.139985>
- Khanesar, M. (2019). Medical Applications of 3-D Printing. *Archives in Biomedical Engineering & Biotechnology*, **2**. <https://doi.org/10.33552/ABEB.2019.02.000531>
- Klink, M. J., Laloo, N., Leudjo Taka, A., Pakade, V. E., Monapathi, M. E., & Modise, J. S. (2022). Synthesis, Characterization and Antimicrobial Activity of Zinc Oxide Nanoparticles against Selected Waterborne Bacterial and Yeast Pathogens. *Molecules*, **27**(11), 3532.
- Knetsch, M. L., & Koole, L. H. (2011). New strategies in the development of antimicrobial coatings: The example of increasing usage of silver and silver nanoparticles. *Polym*, **3**(1), 340–366.
- Körner, C. (2016). Additive manufacturing of metallic components by selective electron beam melting—A review. *Int Mater Rev*, **61**(5), 361–377.
- Kwok, S. W., Goh, K. H. H., Tan, Z. D., Tan, S. T. M., Tjiu, W. W., Soh, J. Y., Ng, Z. J. G., Chan, Y. Z., Hui, H. K., & Goh, K. E. J. (2017). Electrically conductive filament for 3-D-printed circuits and sensors. *Appl Mater Today*, **9**, 167–175.

- Lai, B., Zhou, Y., Qin, H., Wu, C., Pang, C., Lian, Y., & Xu, J. (2012). Pretreatment of wastewater from acrylonitrile–butadiene–styrene (ABS) resin manufacturing by microelectrolysis. *Chem Eng J*, **179**, 1–7. <https://doi.org/10.1016/j.cej.2010.12.089>
- Larson, R. G. (2004). Principles for coarse-graining polymer molecules in simulations of polymer fluid mechanics. *Mol Phys*, **102**(4), 341–351.
- Lebreton, L., & Andrady, A. (2019). Future scenarios of global plastic waste generation and disposal. *Palgrave Commun*, **5**(1), 1–11.
- Lee, J., Mahendra, S., & Alvarez, P. J. (2010). Nanomaterials in the construction industry: A review of their applications and environmental health and safety considerations. *ACS Nano*, **4**(7), 3580–3590.
- Liacouras, P., Garnes, J., Roman, N., Petrich, A., & Grant, G. T. (2011). Designing and manufacturing an auricular prosthesis using computed tomography, 3-dimensional photographic imaging, and additive manufacturing: A clinical report. *J Prosthet Dent*, **105**(2), 78–82.
- Ligon, S. C., Liska, R., Stampfl, J., Gurr, M., & Mülhaupt, R. (2017). Polymers for 3-D printing and customized additive manufacturing. *Chem Rev*, **117**(15), 10212–10290.
- Liu, H., & Webster, T. (2023). *From Nano to Micro: Nanostructured Titania/PLGA Orthopedic Tissue Engineering Scaffolds Assembled by Three-dimensional Printing*. AIChE Annual Meeting, San Francisco, CA, 56002.
- Liu, Y., He, L., Mustapha, A., Li, H., Hu, Z. Q., & Lin, M. (2009). Antibacterial activities of zinc oxide nanoparticles against Escherichia coli O157: H7. *J Appl Microbiol*, **107**(4), 1193–1201.
- Liu, Y. J., Qu, J. P., & Cao, X. W. (2005). Mathematical model of shear rate of polymer melt dynamic extruding through capillary. *J Appl Polym Sci*, **95**(5), 1056–1061. <https://doi.org/10.1002/app.21281>
- Lorenzo, A. T., Arnal, M. L., Albuérne, J., & Müller, A. J. (2007). DSC isothermal polymer crystallization kinetics measurements and the use of the Avrami equation to fit the data: Guidelines to avoid common problems. *Polym Test*, **26**(2), 222–231.
- Lu, B. H., & Li, D. C. (2013). Development of the additive manufacturing (3-D printing) technology. *Machine Building & Automation*, **42**(4), 1–4.



- Luckachan, G. E., & Pillai, C. K. S. (2011). Biodegradable polymers-a review on recent trends and emerging perspectives. *J Polym Environ*, **19**(3), 637–676.
- Mangaraj, S., Yadav, A., Bal, L. M., Dash, S. K., & Mahanti, N. K. (2019). Application of biodegradable polymers in food packaging industry: A comprehensive review. *J Package Technol Res*, **3**, 77–96.
- Matos, B., Rocha, V., Jannone da Silva, E., Moro, F., Bottene, A., Ribeiro, C., Dias, D., Antonio, S., Amaral, A., Cruz, S., Barud, H., & Barud, H. (2018). Evaluation of commercially available polylactic acid (PLA) filaments for 3-D printing applications. *J Therm Anal Calorim*, **137**. <https://doi.org/10.1007/s10973-018-7967-3>
- Mehta, R., Kumar, V., Bhunia, H., & Upadhyay, S. N. (2005). Synthesis of poly (lactic acid): A review. *J Macromol Sci, Part C: Polymer Reviews*, **45**(4), 325–349.
- Melchels, F. P., Feijen, J., & Grijpma, D. W. (2010). A review on stereolithography and its applications in biomedical engineering. *Biomaterials*, **31**(24), 6121–6130.
- Mihindukulasuriya, S. D. F., & Lim, L.-T. (2014). Nanotechnology development in food packaging: A review. *Trends Food Sci Technol*, **40**(2), 149–167.
- Milman, V., Winkler, B., White, J. A., Pickard, C. J., Payne, M. C., Akhmatskaya, E. V., & Nobes, R. H. (2000). Electronic structure, properties, and phase stability of inorganic crystals: A pseudopotential plane-wave study. *Int J Quantum Chem*, **77**(5), 895–910.
- Mondal, D., Griffith, M., & Venkatraman, S. S. (2016). Polycaprolactone-based biomaterials for tissue engineering and drug delivery: Current scenario and challenges. *Int J Polym Mater Polym Biomater*, **65**(5), 255–265.
- Müller-Plathe, F. (2002). Coarse-graining in polymer simulation: From the atomistic to the mesoscopic scale and back. *ChemPhysChem*, **3**(9), 754–769.
- Murcia Valderrama, M. A., van Putten, R.-J., & Gruter, G.-J. M. (2020). PLGA barrier materials from CO<sub>2</sub>. The influence of lactide co-monomer on glycolic acid polyesters. *ACS Appl Polym Mater*, **2**(7), 2706–2718.
- Napadensky, E. (2003). *Compositions and methods for use in three dimensional model printing* (United States Patent No. US6569373B2). <https://patents.google.com/patent/US6569373B2/en>

- Napadensky, E., Kritchman, E. M., & Cohen, A. (2007). *Compositions and methods for use in three dimensional model printing* (United States Patent No. US7300619B2). <https://patents.google.com/patent/US7300619B2/en>
- Narayanan, P. M., Wilson, W. S., Abraham, A. T., & Sevanan, M. (2012). Synthesis, characterization, and antimicrobial activity of zinc oxide nanoparticles against human pathogens. *Bio Nano Science*, **2**(4), 329–335.
- Nath, S. D., & Nilufar, S. (2020). An overview of additive manufacturing of polymers and associated composites. *Polym*, **12**(11), 2719.
- Niaounakis, M. (2013). *Biopolymers: Reuse, recycling, and disposal*. William Andrew, NewYork: 50-89.
- Oksiuta, Z., Jalbrzykowski, M., Mystkowska, J., Romanczuk, E., & Osiecki, T. (2020). Mechanical and Thermal Properties of Polylactide (PLA) Composites Modified with Mg, Fe, and Polyethylene (PE) Additives. *Polym*, **12**(12), 2939.
- Olivera, S., Muralidhara, H. B., Venkatesh, K., Gopalakrishna, K., & Vivek, C. S. (2016). Plating on acrylonitrile–butadiene–styrene (ABS) plastic: A review. *J Mater Sci*, **51**(8), 3657–3674.
- Onyari, J. M., Mulaa, F., Muia, J., & Shiundu, P. (2008). Biodegradability of Poly (lactic acid), Preparation and Characterization of PLA/Gum Arabic Blends. *J Polym Environ*, **16**(3), 205–212. <https://doi.org/10.1007/s10924-008-0096-5>
- Otieno, D., Geoffrey, B., Onyari, J., & Mwabora, J. (2022). Comparative analysis of 3-D-printed polylactic acid and acrylonitrile butadiene styrene: Experimental and Materials-Studio-based theoretical studies. *J Polym Res*, **29**, 291. <https://doi.org/10.1007/s10965-022-03075-6>
- Padiyara, P., Inoue, H., & Sprenger, M. (2018). Global governance mechanisms to address antimicrobial resistance. *Infectious Diseases: Res Treat*, **11**, 1178633718767887.
- Padmavathy, N., & Vijayaraghavan, R. (2008). Enhanced bioactivity of ZnO nanoparticles—An antimicrobial study. *Sci Technol Adv Mater*, **9**(3). <https://doi.org/10.1088/1468-6996/9/3/035004>
- Pal, S., Tak, Y. K., & Song, J. M. (2007). Does the antibacterial activity of silver nanoparticles depend on the shape of the nanoparticle? A study of the gram-negative bacterium *Escherichia coli*. *Appl Environ Microbiol*, **73**(6), 1712–1720.

- Palai, B., Biswal, M., Mohanty, S., & Nayak, S. K. (2019). In situ reactive compatibilization of polylactic acid (PLA) and thermoplastic starch (TPS) blends; synthesis and evaluation of extrusion blown films thereof. *Ind Crops Prod*, **141**, 111748.
- Palmara, G., Frascella, F., Roppolo, I., Chiappone, A., & Chiadò, A. (2021). Functional 3-D printing: Approaches and bioapplications. *Biosens. Bioelectron*, **175**, 112849.
- Panáček, A., Kvítek, L., Pucek, R., Kolář, M., Večeřová, R., Pizúrová, N., Sharma, V. K., Nevěčná, T. ějana, & Zbořil, R. (2006). Silver colloid nanoparticles: Synthesis, characterization, and their antibacterial activity. *J Phys Chem B*, **110**(33), 16248–16253.
- Papadakis, L., Loizou, A., Risse, J., Bremen, S., & Schrage, J. (2014). A computational reduction model for appraising structural effects in selective laser melting manufacturing. *Virtual Phys Prototyp*, **9**(1), 17–25. <https://doi.org/10.1080/17452759.2013.868005>
- Papaoiannou, T. G., Manolesou, D., Dimakakos, E., Tsoucalas, G., Vavuranakis, M., & Tousoulis, D. (2019). 3-D bioprinting methods and techniques: Applications on artificial blood vessel fabrication. *Acta Cardiologica Sinica*, **35**(3), 284.
- Park, J.-U., Hardy, M., Kang, S. J., Barton, K., Adair, K., Lee, C. Y., Strano, M. S., Alleyne, A. G., Georgiadis, J. G., & Ferreira, P. M. (2007). High-resolution electrohydrodynamic jet printing. *Nat Mater*, **6**(10), 782–789.
- Paul, G. M., Rezaenia, A., Wen, P., Condoor, S., Parkar, N., King, W., & Korakianitis, T. (2018). Medical applications for 3-D printing: Recent developments. *Mo Med*, **115**(1), 75.
- Pavithra, D., & Doble, M. (2008). Biofilm formation, bacterial adhesion and host response on polymeric implants—Issues and prevention. *Biomed Mater*, **3**(3), 034003.
- Piccin, J. S., Dotto, G. L., & Pinto, L. A. A. (2011). Adsorption isotherms and thermochemical data of FD&C Red n 40 binding by chitosan. *Braz J Chem Eng*, **28**, 295–304.
- Powell, S. K., Cruz, R. L., Ross, M. T., & Woodruff, M. A. (2020). Past, present, and future of soft-tissue prosthetics: Advanced polymers and advanced manufacturing. *Adv Mater*, **32**(42), 2001122.
- Prabhakar, M. M., Saravanan, A. K., Lenin, A. H., Mayandi, K., & Ramalingam, P. S. (2021). A short review on 3-D printing methods, process parameters and materials. *Mater Today: Proceed*, **45**, 6108–6114.

- Prata, J. C., Silva, A. L. P., da Costa, J. P., Mouneyrac, C., Walker, T. R., Duarte, A. C., & Rocha-Santos, T. (2019). Solutions and Integrated Strategies for the Control and Mitigation of Plastic and Microplastic Pollution. *Int J Environ Res Public Health*, **16**(13), Article 13. <https://doi.org/10.3390/ijerph16132411>
- Rangel, W. M., Santa, R. A. A. B., & Riella, H. G. (2020). A facile method for synthesis of nanostructured copper (II) oxide by coprecipitation. *J Mater Res Technol*, **9**(1), 994–1004.
- Rodríguez, J. F., Thomas, J. P., & Renaud, J. E. (2003). Mechanical behavior of acrylonitrile butadiene styrene fused deposition materials modeling. *Rapid Prototyp J*, **9**(4), 219-230. <https://doi.org/10.1108/13552540310489604>
- RUJNIC-SOKELE, M. (2005). Catia Bastioli: Handbook of Biodegradable Polymers. *Polimeri: Časopis Za Plastiku i Gumu*, **26**(1), 47–47.
- Rydz, J., Musion, I. M., Zawidlak-Węgrzyńska, B., & Sikorska, W. (2018). Chapter Present and future of biodegradable polymers for food packaging applications, In: Grumezescu, A. M., Holban, A. M., handbook of food Bioengineering, *Biopolym Food Des*, Academic Press, 431–467. <https://doi.org/10.1016/B978-0-12-811449-0.00014-1>.
- Ryjkina, E., Kuhn, H., Rehage, H., Müller, F., & Peggau, J. (2002). Molecular Dynamic Computer Simulations of Phase Behavior of Non-Ionic Surfactants. *Angew Chem Int Ed*, **41**(6), 983–986.
- Saba, N., Tahir, P. M., & Jawaid, M. (2014). A Review on Potentiality of Nano Filler/Natural Fiber Filled Polymer Hybrid Composites. *Polym*, **6**(8), Article 8. <https://doi.org/10.3390/polym6082247>
- Sajid, M., Gul, J. Z., Kim, S. W., Kim, H. B., Na, K. H., & Choi, K. H. (2018). Development of 3-D printed embedded temperature sensor for both terrestrial and aquatic environmental monitoring robots. *3-D Print Addit Manuf*, **5**(2), 160–169.
- Saravanan, M., Gopinath, V., Chaurasia, M. K., Syed, A., Ameen, F., & Purushothaman, N. (2018). Green synthesis of anisotropic zinc oxide nanoparticles with antibacterial and cytofriendly properties. *Microb Pathog*, **115**, 57–63. <https://doi.org/10.1016/j.micpath.2017.12.039>

- Sathishkumar, T. P., Navaneethakrishnan, P., Shankar, S., & Rajasekar, R. (2013). Characterization of new cellulose sansevieria ehrenbergii fibers for polymer composites. *Compos Interfaces*, **20**(8), 575–593.
- Schmidt, K. A., Doan, V. A., Xu, P., Stockwell, J. S., & Holden, S. K. (2008). *Ultra-violet light curable hot melt composition* (United States Patent No. US7378460B2).
- Shahrubudin, N., Lee, T. C., & Ramlan, R. (2019). An overview on 3-D printing technology: Technological, materials, and applications. *Procedia Manuf*, **35**, 1286–1296.
- Sherrill, C. D. (2000). An introduction to Hartree-Fock molecular orbital theory. *School of Chemistry and Biochemistry Georgia Institute of Technology*. 1-8.
- Silva, A. L. P., Prata, J. C., Walker, T. R., Duarte, A. C., Ouyang, W., Barcelò, D., & Rocha-Santos, T. (2021). Increased plastic pollution due to COVID-19 pandemic: Challenges and recommendations. *Chem Eng J*, **405**, 126683.
- Simmons, D. S. (2022). Macromolecular Modeling. *Macromol Eng: From Precise Synthesis to Macroscopic Materials and Applications*, 1–40. <https://doi.org/10.1002/9783527815562.mme0049>
- Sin, L. T. (2012). *Polylactic acid: PLA biopolymer technology and applications*. William Andrew, Florida, 50-55.
- Sin, L. T., Rahmat, A. R., & Rahman, W. A. W. A. (2012). *Polylactic acid: PLA biopolymer technology and applications*. William Andrew, Florida, 70-84.
- Singare, S., Liu, Y., Li, D., Lu, B., & He, S. (2008). Individually prefabricated prosthesis for maxilla reconstruction. *J Prosthodont*, **17**(2), 135–140.
- Singhvi, M. s., Zinjarde, S. s., & Gokhale, D. v. (2019). Polylactic acid: Synthesis and biomedical applications. *J Appl Microbiol*, **127**(6), 1612–1626. <https://doi.org/10.1111/jam.14290>
- Sintim, H. Y., Bary, A. I., Hayes, D. G., Wadsworth, L. C., Anunciado, M. B., English, M. E., Bandopadhyay, S., Schaeffer, S. M., DeBruyn, J. M., & Miles, C. A. (2020). In situ degradation of biodegradable plastic mulch films in compost and agricultural soils. *Sci Total Environ*, **727**, 138668.

- Sirelkhatim, A., Mahmud, S., Seeni, A., Kaus, N. H. M., Ann, L. C., Bakhori, S. K. M., Hasan, H., & Mohamad, D. (2015). Review on Zinc Oxide Nanoparticles: Antibacterial Activity and Toxicity Mechanism. *Nano-Micro Lett*, **7**(3), 219–242. <https://doi.org/10.1007/s40820-015-0040-x>
- Smith, M., Love, D. C., Rochman, C. M., & Neff, R. A. (2018). Microplastics in seafood and the implications for human health. *Curr Environ Health Rep*, **5**, 375–386.
- Sotiriou, G. A., & Pratsinis, S. E. (2010). Antibacterial activity of nanosilver ions and particles. *Environ Sci Technol*, **44**(14), 5649–5654.
- Stewart, S. R., Wentz, J. E., & Allison, J. T. (2015). Experimental and computational fluid dynamic analysis of melt flow behavior in fused deposition modelling of poly (lactic) acid. *ASME International Mechanical Engineering Congress and Exposition*, 57359, V02AT02A010; 8. <https://doi.org/10.1115/IMECE2015-52261>
- Stotko, C. M. (2009). Layer by layer. *Nature Photonics*, **3**(5), 265–266. <https://doi.org/10.1038/nphoton.2009.60>
- Sun, D., & Valtasa, A. (2019). 3-D printing in modern fashion industry. *J Text Sci Fashion Technol*, **2**(2), 1–4. <https://doi.org/10.33552/JTSFT.2019.02.000535>
- Sun, Q., Rizvi, G. M., Bellehumeur, C. T., & Gu, P. (2008). Effect of processing conditions on the bonding quality of FDM polymer filaments. *Rapid Prototyp J*, **14**(2), 72-80. <https://doi.org/10.1108/13552540810862028>
- Suri, S. S., Fenniri, H., & Singh, B. (2007). Nanotechnology-based drug delivery systems. *J Occup Med Toxicol*, **2**(1), 16. <https://doi.org/10.1186/1745-6673-2-16>
- Tábi, T. (2019). The application of the synergistic effect between the crystal structure of poly (lactic acid)(PLA) and the presence of ethylene vinyl acetate copolymer (EVA) to produce highly ductile PLA/EVA blends. *J Therm Anal Calorim*, **138**(2), 1287–1297.
- Takahashi, E., Shirai, A., Takahashi, H., & Kimizuka, S. (2003). *Photocurable composition containing iodonium salt compound* (United States Patent No. US6558871B1).
- Takahashi, E., Shirai, A., Takahashi, H., & Kimizuka, S. (2004). *Photocurable composition containing iodonium salt compound* (United States Patent No. US6677390B1).

- Takhulee, A., Takahashi, Y., & Vao-soongnern, V. (2017). Molecular simulation and experimental studies of the miscibility of polylactic acid/polyethylene glycol blends. *J Polym Res*, **24**(1), 1–10.
- Tan, L. J., Zhu, W., & Zhou, K. (2020). Recent progress on polymer materials for additive manufacturing. *Adv Funct Mater*, **30**(43), 2003062.
- Tang, M., Pistorius, P. C., & Beuth, J. (2015). Geometric model to predict porosity of part produced in powder bed system. *Materials Science & Technology Proceedings (MS&T)*, 129–136.
- Tang, Y., Henderson, C., Muzzy, J., & Rosen, D. W. (2004). Stereolithography cure modelling and simulation. *Int J Mater Prod Technol*, **21**(4), 255–272. <https://doi.org/10.1504/IJMPT.2004.004941>
- Tappa, K., & Jammalamadaka, U. (2018). Novel biomaterials used in medical 3-D printing techniques. *J Funct Biomater*, **9**(1), 17.
- Thrimurthulu, K., Pandey, P. M., & Reddy, N. V. (2004). Optimum part deposition orientation in fused deposition modeling. *Int J Mach Tools Manuf*, **44**(6), 585–594.
- van Velzen, E. T., Jansen, M., Brouwer, M. T., Feil, A., Molenveld, K., & Pretz, T. (2017). Efficiency of recycling post-consumer plastic packages. *AIP Conference Proceedings*, **1914**(1), 170002.
- Vassallo, A., Silletti, M. F., Faraone, I., & Milella, L. (2020). Nanoparticulate antibiotic systems as antibacterial agents and antibiotic delivery platforms to fight infections. *J Nanomater*, **2020**, 1–31.
- Vlachopoulos, A., Karlioti, G., Balla, E., Daniilidis, V., Kalamas, T., Stefanidou, M., Bikiaris, N. D., Christodoulou, E., Koumentakou, I., & Karavas, E. (2022). Poly (lactic acid)-based microparticles for drug delivery applications: An overview of recent advances. *Pharmaceutics*, **14**(2), 359.
- Wan, X., Luo, L., Liu, Y., & Leng, J. (2020). Direct ink writing based 4D printing of materials and their applications. *Adv Sci*, **7**(16), 2001000.
- Wang, T.-M., Xi, J.-T., & Jin, Y. (2007). A model research for prototype warp deformation in the FDM process. *Int J Adv Manuf Technol*, **33**(11), 1087–1096.

- Wei, Q., Cai, X., Guo, Y., Wang, G., Guo, Y., Lei, M., Song, Y., Yingfeng, Z., & Wang, Y. (2019). Atomic-scale and experimental investigation on the micro-structures and mechanical properties of PLA blending with CMC for additive manufacturing. *Mater Des*, **183**, 108158. <https://doi.org/10.1016/j.matdes.2019.108158>
- Woodfield, T. B. F., Malda, J., de Wijn, J., Péters, F., Riesle, J., & van Blitterswijk, C. A. (2004). Design of porous scaffolds for cartilage tissue engineering using a three-dimensional fiber-deposition technique. *Biomaterials*, **25**(18), 4149–4161. <https://doi.org/10.1016/j.biomaterials.2003.10.056>
- Wright, S. L., & Kelly, F. J. (2017). Plastic and human health: A micro issue? *Environ Sci Technol*, **51**(12), 6634–6647.
- Yan, Q., Dong, H., Su, J., Han, J., Song, B., Wei, Q., & Shi, Y. (2018). A review of 3-D printing technology for medical applications. *Engineering*, **4**(5), 729–742.
- Yang, H., Ze-Sheng, L., Qian, H., Yang, Y., Zhang, X., & Sun, C. (2004). Molecular dynamics simulation studies of binary blend miscibility of poly (3-hydroxybutyrate) and poly (ethylene oxide). *Polym*, **45**(2), 453–457.
- Ying-Chen, Z., Hong-Yan, W., & Yi-Ping, Q. (2010). Morphology and properties of hybrid composites based on polypropylene/poly(lactic acid) blend and bamboo fiber. *Bioresour Technol*, **101**(20), 7944–7950. <https://doi.org/10.1016/j.biortech.2010.05.007>
- Zäh, M. F., & Lutzmann, S. (2010). Modelling and simulation of electron beam melting. *Prod Eng*, **4**(1), 15–23.
- Zeng, F., Sun, Y., Zhou, Y., & Li, Q. (2009). Molecular simulations of the miscibility in binary mixtures of PVDF and POSS compounds. *Model Simul Mater Sci Eng*, **17**(7), 075002.
- Zhang, B., Gao, L., Ma, L., Luo, Y., Yang, H., & Cui, Z. (2019). 3-D bioprinting: A novel avenue for manufacturing tissues and organs. *Engineering*, **5**(4), 777–794.
- Zhang, B., Luo, Y., Ma, L., Gao, L., Li, Y., Xue, Q., Yang, H., & Cui, Z. (2018). 3-D bioprinting: An emerging technology full of opportunities and challenges. *Bio-Des. Manuf*, **1**(1), 2–13.
- Zhang, F., Tuck, C., Hague, R., He, Y., Saleh, E., Li, Y., Sturgess, C., & Wildman, R. (2016). Inkjet printing of polyimide insulators for the 3 D printing of dielectric materials for microelectronic applications. *J Appl Polym Sci*, **133**(18).



- Zhang, Y., & Chou, K. (2008). A parametric study of part distortions in fused deposition modelling using three-dimensional finite element analysis. *Proceedings of the Institution of Mechanical Engineers, Part B: J Eng Manuf*, **222**(8), 959–968. <https://doi.org/10.1243/09544054JEM990>
- Zhang, Y., & Dubé, M. A. (2017). Green emulsion polymerization technology. *Polymer Reaction Engineering of Dispersed Systems*, 65–100. Volume I (pp. 65–80).
- Zhang, Y., & Dubé, M. A. (2018). Green Emulsion Polymerization Technology. In W. Pauer (Ed.), *Polymer Reaction Engineering of Dispersed Systems: Volume I* (pp. 65–100). Springer International Publishing. [https://doi.org/10.1007/12\\_2017\\_8](https://doi.org/10.1007/12_2017_8)
- Zheng, Y., Yanful, E. K., & Bassi, A. S. (2005). A Review of Plastic Waste Biodegradation. *Crit Rev Biotechnol*, **25**(4), 243–250. <https://doi.org/10.1080/07388550500346359>
- Zhou, L.-Y., Fu, J., & He, Y. (2020). A Review of 3-D Printing Technologies for Soft Polymer Materials. *Adv Funct Mater*, **30**(28), 2000187. <https://doi.org/10.1002/adfm.202000187>
- Zhou, X., Hsieh, S.-J., & Sun, Y. (2017). Experimental and numerical investigation of the thermal behaviour of polylactic acid during the fused deposition process. *Virtual Phys Prototyp*, **12**(3), 221–233.
- Zhu, C., Liu, T., Qian, F., Han, T. Y.-J., Duoss, E. B., Kuntz, J. D., Spadaccini, C. M., Worsley, M. A., & Li, Y. (2016). Supercapacitors based on three-dimensional hierarchical graphene aerogels with periodic macropores. *Nano Lett*, **16**(6), 3448–3456.
- Ziemian, S., Okwara, M., & Ziemian, C. W. (2015). Tensile and fatigue behavior of layered acrylonitrile butadiene styrene. *Rapid Prototyp J*.

## APPENDICES

### I. Zinc Oxide crystal structure

The zinc oxide crystal model was developed using the material studio software 2021 user interface (Figure 35) (Otieno *et al.*, 2022). Supercell units of 4 x 3 x 3 were created using symmetry calculations. The structure was optimized using the BFGS algorithm. Zinc oxide belongs to a P63MC space group with a hexagonal crystal structure.

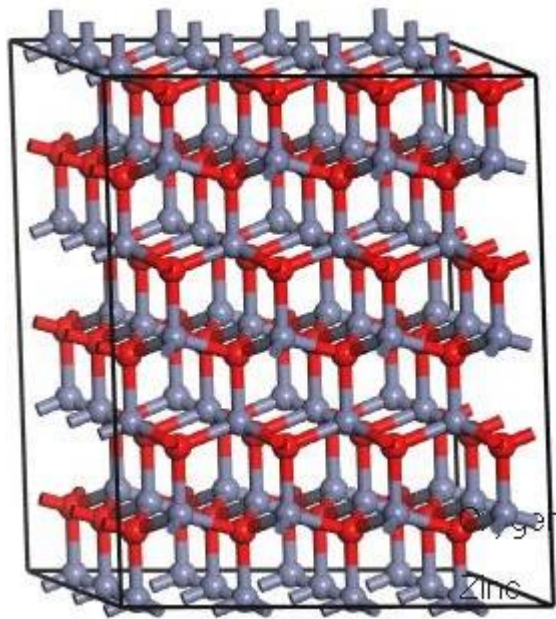


**Figure 35:** Zinc oxide 3-D structure

### II. Copper oxide crystal structure

The copper oxide crystal model has been built using the material studio software 2021 user interface (Figure 36). Supercell units of 3 x 3 x 3 were created using symmetry calculations. Copper oxide has a monoclinic structure with a space group of C2/C (Gherasim *et al.*, 2022).

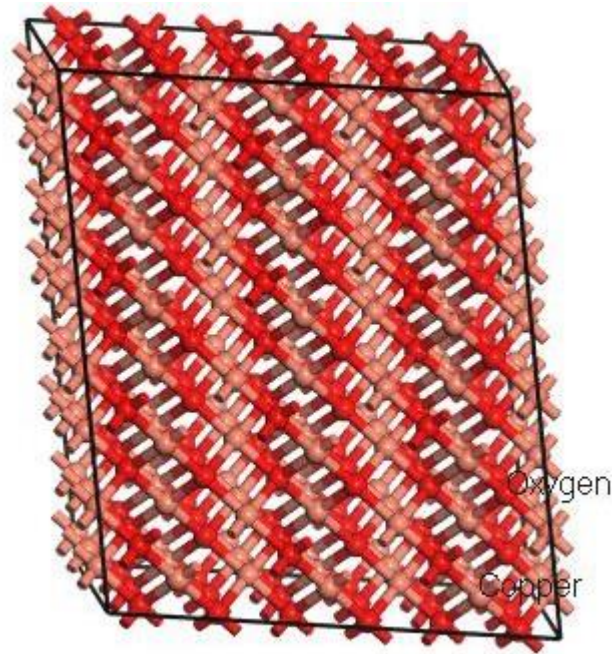


**Figure 36:** Copper oxide 3-D structure

### **III. Blending of PLA, ABS, Zinc Oxide and Copper Oxide nanoparticles**

PLA, ABS, and the nanocrystals were screened for compatibility. The lactic acid monomer was geometrically optimized before carrying out blend calculations. Copper oxide and zinc oxide NPs were screened against lactic acid and acrylonitrile butadiene styrene (base role). This aided in the calculations of the binding and mixing energies of the polymer and the nanoparticles. Setting up the head and tail atoms on the repeat units was signified by the presence of magenta and cyan cages around the respective atoms (figure 37a). This minimized close contact with any other atom in the system hence allowing the monomer to mimic the rest of the polymer which was represented by the non-contact atoms (Zeng *et al.*, 2009).

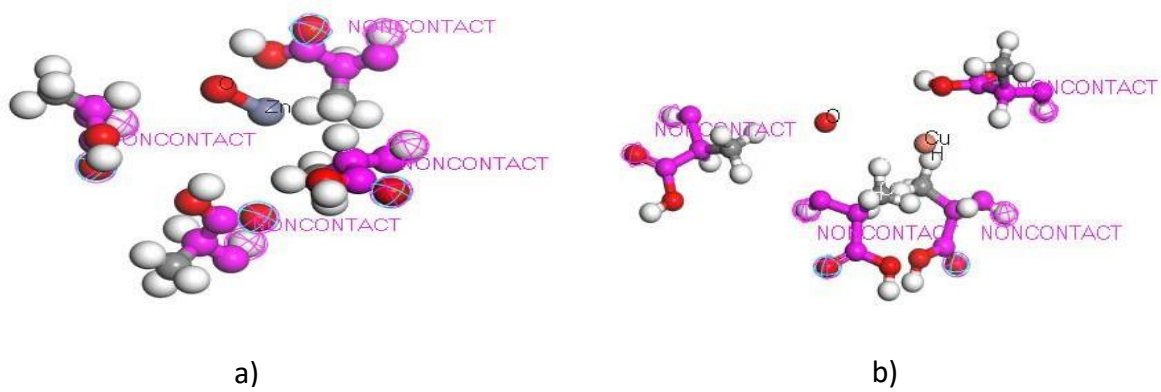


**Figure 37a:** PLAZnO and PLACuO blends respectively

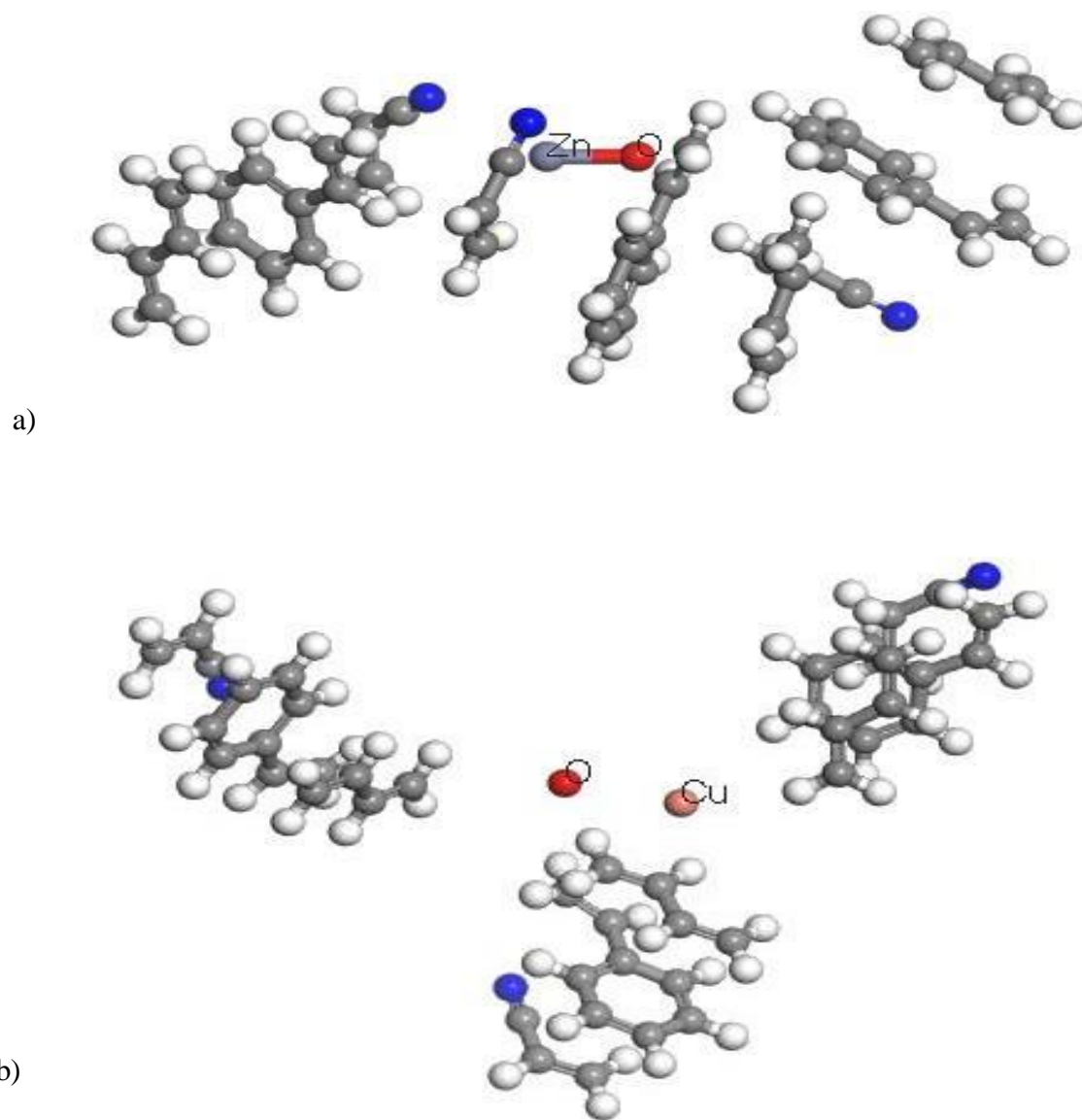


**Figure 37b:** ABSZnO and ABSCuO blends respectively